Stability of Thick and Thin Flexible Pipes Subjected to Axial Flow

by

Stéphane Jamin

Under the supervision of

Professor M.P. Païdoussis and Professor M. Amabili

Department of Mechanical Engineering

McGill University

Montréal, Québec, Canada

A thesis submitted to McGill University in partial fulfilment of the
requirements of the Master's of Engineering Thesis Program

Abstract

Have you ever experienced oscillatory motions of the free end your hose while watering your garden? This ordinary phenomenon of a pipe conveying fluid has asserted itself as a paradigm since it is described by quite simple equations and its study has various applications in engineering systems such as heat exchangers, blood circulatory systems as well as mining operations.

The scope of the present work is the study of the dynamics of two different kinds of cylindrical pipes: (i) a cantilevered thin-walled pipe, i.e. a cylindrical shell, aspirating air and (ii) a thick-walled pipe subjected to internal, external, or simultaneous internal and external axial flows. This was accomplished for the cantilevered shell by deriving a linear analytical model through a variational principle while taking into account modified boundary conditions, and then by comparing theoretical and experimental results. For the thick wall pipe, the study was mainly experimental. A great part of the work was to design and build an entirely new apparatus allowing the investigation of the dynamics of the pipe in a lot of different configurations. The critical flow velocity and the corresponding frequency of oscillation as well as the pipe behaviour at higher flow velocities are described.

Sommaire

N'avez-vous jamais ressenti un mouvement d'oscillations de l'extrémité libre de votre tuyau pendant que vous arrosiez votre jardin? Ce phénomène, banal pour un tuyau véhiculant un fluide, s'est imposé comme un problème fondamental puisqu'il est gouverné pas des équations relativement simples et que son étude a des applications dans des systèmes aussi variés que les échangeurs de chaleur, les systèmes de circulation sanguine et les opérations minières.

L'objectif de ce travail de recherche est l'étude de la dynamique de deux différents types de tuyaux cylindriques: (i) un tuyau encastré-libre à paroi mince, i.e. une coque cylindrique, aspirant de l’air et (ii) un tuyau à paroi large soumis à un écoulement axial qui peut être interne, externe, ou les deux simultanément. Pour la coque encastrée-libre, ce fut accompli en dérivant un modèle analytique linéaire par l'intermédiaire d'un principe variationnel tout en prenant en compte des conditions aux limites modifiées, puis, en comparant les résultats théoriques et expérimentaux. Pour le tuyau à paroi large, l'étude fut principalement expérimentale. La majeure partie de ce travail fut la conception et le montage d'un appareil entièrement nouveau qui permet d'étudier le comportement du tuyau dans de multiples configurations. La vitesse d'écoulement critique, la fréquence d'oscillation correspondante ainsi que l'évolution du comportement du tuyau lorsque la vitesse d'écoulement augmente sont présentées.

Acknowledgements

First, it is a real pleasure to profoundly thank my research supervisor, Professor Michael P. Païdoussis for his support, his guidance throughout the course of this project as well as his patience to my many questions. I would also like to thank Professor Marco Amabili for the co-supervision of a part of this work.

I would like to extend my appreciation to all the members of the McGill Fluid-Structure Interaction lab for their company, assistance and friendly talk: Ahmad, Dana, James, Kostas, Medhi, Mergen, Mojtaba, Stephanie and Wensheng. I would also like to thank my office coworkers for their pleasant discussion.

I am also grateful to Thierry Lafrance of Ecole Polytechnique and Gary Savard for their valuable help to design and build a new experimental apparatus. I am further indebted to François Di Quinzio, Georges Tewfik, Tony Micozzi and William Alcock for their advice, aid and technical assistance, and to Professor Roderick Guthrie and Dr Mihaela Isac for the heat treatment in their laboratory of the helical spring inserted in the pipe in the experiments, in order to straighten it.

I would also like to acknowledge the financial support of the Natural Sciences and Engineering Research Council of Canada and the Solution Mining Research Institute.

Special thanks go out to all my friends for the two wonderful and rewarding years I spent in Montreal. Finally, I would like to express my gratitude to my family for their unconditional support and encouragement. While completing this thesis, I would like to spare a kind thought for my sister, Valérie, and my mother, Marie.

Table of Contents

Chapter 1: Introduction

1.1 Outline of the Thesis

The work done in this thesis can be divided into two main themes. The first deals with the stability of a cantilevered thin-walled pipe, i.e. a cylindrical shell, aspirating air. In the second one, the dynamics of a thick-walled pipe subjected to internal, external or simultaneous internal and external flows is experimentally investigated and some of the results are compared with an existing linear theory.

This thesis encompassed four chapters. Chapter 1 provides the general context of the research through a literature review that, first, introduces the field of Fluid-Structure Interactions and then briefly discusses earlier work carried out on different systems involving cylindrical cantilevered structures: (i) cantilevered cylindrical structures discharging fluid, (ii) cantilevered cylindrical structures in axial flow, (iii) cantilevered coaxial cylindrical structures and (iv) cantilevered cylindrical structures aspirating fluid. In Chapter 2, the dynamics of a flexible cantilevered shell aspirating fluid is studied both experimentally and theoretically. A new analytical model is first derived by taking into account a new boundary condition due to the fluid flowing from the free end to the clamped end. The linear equations of motion are then derived through a variational principle and solved using the extended form of the Galerkin method. Finally, the theoretical results are compared to experimental observations for two different pipes that are made of the same material but whose lengths and wall thicknesses differ. Chapter 3 treats the problem of the stability of the hanging tubular pipes used in salt caverns. The study was mainly experimental. A great part of the work was to design and build an entirely new apparatus allowing the investigation of the dynamics of the pipe in a lot of different configurations with water as flowing fluid. In each configuration, the critical flow velocity and the corresponding frequency of oscillations as well as the pipe behaviour at higher flow velocity are described. Finally, Chapter 4 contains a summary and a discussion about this thesis as well as some insights for future work.

1.2 Literature Review

Flow-induced vibration is a common phenomenon that arises in nature. Considering for example a woodwind instrument, it is well known that it produces music thanks to the reed that vibrates because of the blowing air. But, usually, flow induced vibration is an undesirable feature in engineering systems where large amplitude vibrations could not only cause serious and costly damages but also put human life at risk. A really unfortunate example is the collapse of the Tacoma Narrows Bridge in 1940. That is why the study of flow induced vibrations of slender bodies has established itself as a challenging problem which the engineer has to face. Stability and reliability are always required in the development of new equipment.

One of the early industrial studies was thus carried out by Ashley and Haviland (1950) to elucidate the vibrations of the Trans-Arabian pipeline. Since then, the necessity of investigating the dynamics of slender structures subjected to and/or immersed in flow arises in a lot of different engineering systems, such as heat exchangers, nuclear reactors, jet pumps, heat shields in aircraft engines, Coriolis mass-flow meters, as well as pulmonary and blood circulatory systems.

But, in general, much of the work in this area has been curiosity-driven because, just like the column subjected to compressive loading and the rotating shaft are model problems for the study of stability of structures, as pointed out by Païdoussis & Li (1993), the pipe conveying fluid is asserting itself as another paradigm. The dynamics of this system is indeed described by quite simple equations, and experiments can easily be performed, so that theoretical and experimental investigations can both be pursued and compared. However, most importantly, as it is a simple system, it can be used to investigate the effects of different parameters, such as dissipation, fluid compressibility or viscosity but can also be the lead to study more complex systems. Finally it is worth highlighting that these studies sometimes find practical applications years after they have been carried out.

The work that has been undertaken for this Thesis deals with a lot of different configurations involving cantilevered pipes, thick-walled or thin-walled (shells), subjected to internal and/or external axial flow. That is why the following literature review presenting various subjects is selective rather than exhaustive; it mainly focuses on the research dealing with aspirating cylindrical cantilevered structures.

1.2.1 Cantilevered Cylindrical Structures Discharging Fluid

The early work on the dynamics of a pipe conveying fluid was conducted by Brillouin in 1885, his work remaining unpublished. One of his students, Bourrières, undertook a very serious study on this subject right before the Second World War. In his work (1939), rediscovered by Païdoussis more than thirty years later, he derived the correct equation of motion using string theory and was able to study the oscillatory instability of a cantilevered system both theoretically and experimentally. He got very accurate results regarding stability but was unable to predict the critical flow velocity at the onset of oscillation due to lack of tools for numerical solutions.

As recalled before, the interest for this subject was then driven by the problem of the Trans-Arabian pipeline that is considered as a series of simply-supported pipes at both ends. But the equation of motion derived by Ashley and Haviland was incorrect. In the following years, using different modelling but all considering pinned-pinned system, the correct equations of motion were rederived by Feodos'ev (1951), Housner (1952) and Niordson (1953).

Long (1955) was the first to consider a cantilevered pipe. Unfortunately, his method of solution could only determine the dynamics of the system for small flow velocities and he was unable to predict the oscillatory instabilities found by Bourrières.

Considering the dynamics of articulated cantilevered pipes conveying fluid, Benjamin (1961) was the first to report on the phenomenon of unstable oscillations (he was unaware of Bourrières' work). It was later confirmed both theoretically and experimentally by Gregory and Païdoussis (1966) that a continuous cantilevered pipe conveying fluid can flutter at sufficiently high flow velocity. Deriving the linear equation of motion using a Newtonian approach, they were able to predict the critical flow velocity at the onset of oscillatory instability. Païdoussis (1970) then extended the theory to vertical pipes where gravity is operative. Contrary to what Benjamin (1961) observed for articulated pipes, he concluded that buckling does not occur for continuously flexible pipes; this was later explained by Païdoussis and Deksnis (1970) in their study of articulated vertical pipes. They specifically emphasized the inadequacy of the modelling used by Benjamin in the transition from a discrete to a continuous system.

Païdoussis and Issid (1974) re-examined later the stability of the cantilevered pipe by deriving a more general equation of motion that takes into account gravity, dissipation in the material of the pipe due to the surrounding fluid, tensioning and pressurization effects. In an attempt to improve the theory, Laithier and Païdoussis (1981) included shear deformation in deriving the equations; that means they considered the tube as a Timoshenko beam. They found that in the case of short tubes, this theory was more suitable but, surprisingly, not for longer tubes. It was later discovered by Chen (1971) and Sugiyama et al. (1985) that the addition of a motion-constraining spring could stabilize the system or not, depending on its position along the pipe. Other linear studies with additional springs and/or masses were then conducted by Hill and

Swanson (1970), Chen and Jendrzejczyk (1985), Jendrzejczyk and Chen (1985), and Sugiyama et al. (1988).

In all previous studies mentioned so far, the unstable oscillations are supposed to be planar. It was not before the nonlinear equations of motion were derived in the 80's that 3-D motion was considered. The early nonlinear studies were conducted by Rousselet and Herrmann (1981) and Bajaj and Sethna (1982). More recently, Semler et al. (1994) derived very accurate (to third order) and complete nonlinear equations of motion for pipes conveying fluid. They also considered the nonlinear equations with an added mass or springs but only for the case of planar motion. In the past few years, Wadham-Gagnon et al. (2007), Païdoussis et al. (2007) and Modarres-Sadeghi et al. (2007) conducted the same study but also considering 3-D motions in a three-part analysis. Very recently, Ghayesh and Païdoussis (2010) studied further the three-dimensional dynamics of a cantilevered pipe conveying fluid, additionally supported by an intermediate spring array. Rinaldi (2010) studied the effect of a stabilizing end-piece.

In 1934, Donnell was one of the first to tackle the problem of the dynamics of very thin pipes conveying fluid by deriving the equations of motion under simplifying hypotheses. Because of the relative simplicity of the Donnell shallow shell theory, it has been widely used but gives accurate results only for large enough circumferential wavenumber *n*. In 1960, Flügge established a more refined theory presented in his own book (1973). In Yamaki's book (1984), a so-called modified Flügge theory taking into account the effect of bending deformation is presented. Renewed interest in the dynamics of thin-walled pipes (shells) conveying fluid was aroused by the fortuitous discovery in 1969 that both clamped-clamped and clamped-free shells conveying low-speed flow do flutter by losing stability in the so-called second circumferential 'shell-type' mode. That is why Païdoussis and Denise (1970, 1971, 1972) studied both experimentally and theoretically such a system and predicted instabilities in the shell modes involving deformation of the cross-section. Reasonably good agreement was obtained between analytical results and experiments. Similar results were obtained independently by Weaver and Unny (1973) and extended by Weaver and Myklatun (1973).

The problem was then revisited by Shayo and Ellen. They first derived expressions for the generalized aerodynamic forces acting on the tube using Fourier Transform Theory. Thanks to this method, first outlined by Dowell and Widnall (1966), it is possible to avoid considerable effort in the numerical solution required in previous methods. Using this theory, Shayo and Ellen (1974) were able to express the time-dependent fluid pressure due to flowing fluid and could obtain the critical flow velocity at divergence in terms of different parameters such as the radius-to-thickness ratio or the mode numbers. This method was then successfully used by Chan (1984) and Nguyen (1992) in their respective work concerning the dynamics of coaxial cylindrical shells conveying fluid that were clamped-clamped in Chan's work and clamped-free in Nguyen's. In the current study also, it is the method that is used to solve the equations of motion. As the flow is incompressible, it has the great advantage of giving explicit expressions in terms of frequency.

Shayo and Ellen (1978) revealed the importance of the effect of flow perturbations beyond the downstream end of the shell. To take that into account, they introduce so-called downstream flow models. Païdoussis, Luu and Laithier (1986) developed this concept by suggesting three different downstream flow models characterized by different conditions of continuity of the pressure and its derivative at the inlet of the shell and where the perturbation pressure is close to zero at a finite distance *l* downstream of the inlet. Pursuing his work, Nguyen pointed out some inaccuracies and numerical difficulties encountered with those models as *l* was increased. Nguyen, Païdoussis and Misra (1993) developed a new outflow model that is problem free with *l* tending to infinity.

1.2.2 Cantilevered Cylindrical Structures in Axial Flow

The study of vibration of cylindrical structures due to axial flow was undertaken quite recently. It was first related in the 60’s to the power generating industry. It has indeed some engineering applications: e.g., in nuclear reactors with fissile fuel rods subjected to axial flow, heat exchangers, the Dracone barge, towed acoustic arrays for oil exploration and high speed trains in tunnels.

The Dracone is a long flexible towed container with tapered ends used for water transportation. The stability of this kind of flexible tubular container was first investigated by Hawthorne (1961). Through a simplified analysis, he showed the possible buckling of the system at sufficiently high towing velocity.

A more general theoretical and experimental study of cylindrical structures in axial flow was conducted by Païdoussis (1966 a, b). The linear equations of motion were derived including the viscous forces and a shape parameter f related to the tapering of the free end of the cylinder; f is equal to unity if the end is perfectly streamlined, and zero if it is blunt. The theoretical investigation showed that, if the cylinder is sufficiently well streamlined, it first becomes unstable through a static divergence in its first mode. It then regains stability and loses it again by flutter in its second mode and then in its third mode. In the case of a sufficiently blunt end, the first-mode buckling and second-mode flutter can be missed out; as f approaches zero all instabilities disappear. The experimental results are in good agreement with the theory. However, a component due to viscous effects was forgotten when deriving the equations. This mistake was corrected and the correct linear equations of motion taking into account internal dissipation, gravity, pressurization and confinement are given in Païdoussis (1973). However, it turns out that this correction did not change the general theoretical behaviour of the system. Some nonlinear studies were then undertaken, first by Lopes et al. (1999) who derived a first set of equations of motion. A more general analysis was then undertaken by Païdoussis et al. (2002), Lopes et al. (2002) and Semler et al. (2002). The linear and nonlinear theories were investigated and compared to experiments, showing good agreement. The long ‘acoustic streamers’ used in oil exploration revived research interest in the subject. Unlike Dowling (1988) who showed that they were stable at all towed speed, de Langre et al. (2007) demonstrated that very long slender cylinders subjected to axial flow could indeed flutter if the free end is well streamlined.

1.2.3 Cantilevered Coaxial Cylindrical Structures

There exist many engineering applications involving cylindrical structures in a confined channel or two concentric pipes or shells. Annular-flow-induced instabilities occur in certain types of pistons and valves, in control rods in guide tubes in nuclear reactors and in heat exchangers. Different related configurations will be discussed in this section because the flow can be in the inner cylinder only, in the annulus, or in both regions at the same time.

The early studies on the stability of flexible cylinders in axisymmetrically confined flow were undertaken by Païdoussis (1973), Païdoussis and Pettigrew (1979) and Païdoussis and Ostoja-Starzewski (1981). Although the mathematical models do not seem so reliable in the case of not very confined flow, they all point out the destabilizing effect of confinement. The case of a rigid cylindrical body hinged at one point and coaxially positioned in a duct while subjected to annular flow was considered by Hobson (1982). He formulated an analytical model that showed the possible loss of stability via a negative-damping mechanism at sufficiently high velocity. Considering the same type of problem but constraining the free motions of the centre-body with a rotational spring and a rotational dashpot at the hinge point, Mateescu and Païdoussis (1985) developed a more rigorous inviscid analytical model. They demonstrate the existence of a critical location of the hinge, the destabilization of the system as the gap becomes narrower and the dynamical effect of a convergent or divergent passage. They later improved their model (Mateescu and Païdoussis, 1987) to deal with unsteady viscous effects, discovering that they have a stabilizing effect on the system. They also conducted an experimental study of this problem (Mateescu, Païdoussis and Bélanger, 1988), with results in good agreement with the theoretical predictions. Some work was later undertaken to take into account turbulence in the flow and to use other integration methods. The foregoing works give a good overview of the general dynamics of a cylinder subjected to annular flow and we shall now focus on the studies that deal with coaxial systems in which both the inner cylinder and the annulus are filled with fluid.

One of the first studies of a coaxial system containing quiescent fluid is due to Chen and Rosenberg (1975). The main interest was to study the effect of the added mass of the fluid due to the narrowness of the annulus, as well as the hydrodynamical coupling in the motions of the coaxial cylinders giving rise to sets of in-phase and out-of-phase modes. It was found that the lowest frequency of the coupled system is lower than those of the individual shells and is associated to an out-of-phase mode. Au-Yang (1976) calculated the added mass and the coupling coefficients of two coaxial cylinders of different lengths. The main result was the relation of proportionality between their coupled axial mode numbers and their length. Yeh and Chen (1977) studied the effect of viscosity and found that it was negligibly small in most practical systems. The effects of gap width, cylinder wall thickness and boundary conditions were examined by Brown and Lieb (1980).

Those previous studies do not consider a flowing fluid. In the same period, some works dealing with the case of axysymmetric structures subjected to both inner and outer flow consider the external flow as unconfined. Cesari and Curioni (1971) studied a lot of different end-support configurations but only considered the buckling of horizontal pipes. A more general combined experimental and theoretical study was done by Hannoyer and Païdoussis (1978). They derived the equations of motion for both the cases of cantilevered and simply supported beams, including the effects of gravity, internal dissipation and an external boundary layer. It was found that, for a pinned-pinned system, increasing the internal and/or external flow caused the system to lose stability first by buckling, followed by a succession of buckling and flutter instabilities. For the cantilevered beam, the stability characteristics are not straightforward and depend on the velocities of the internal and external flow in a more complex fashion as well as on the shape of the free end. If it is well streamlined, the system will lose stability by a complex sequence of buckling and flutter instabilities, depending on the parameters of the system. If the free end is blunt, the dynamics of the system is dominated by internal flow and flutter will occur. Hannoyer and Païdoussis (1979) later extended their model to deal with the case of conical cantilevers. They found that a conical beam inside and/or outside is usually less stable. In all cases, experiments were also conducted and the results were found to be in good agreement with theory.

It appears that Krajcinovic (1974) was the first to consider flowing fluid in a confined annular region; but he was able to determine the lowest natural frequencies of the system only. Weppelink (1979) undertook a more general study of the dynamics of a flexible cylindrical shell in a coaxial rigid cylinder within the inner shell and/or in the annular region; but only limited calculations and results were given. In the 80’s, Païdoussis et al. (1984) conducted a really serious study of the stability of a system of two clamped-clamped coaxial shells subjected to incompressible or compressible inviscid fluid in the annulus and/or the inner shell. The shell motions are governed by Flügge’s thin-shell equations, potential flow theory is considered to describe the fluid motions, and the aerodynamic forces are evaluated through the Fourier transform method; Galerkin’s method is used to get solutions of the set of equations. It was found that, by increasing the flow velocity in the inner and/or the outer region, the system first loses stability by divergence followed by coupled-mode flutter, but also that the coupled system is less stable than a single shell.

The model was then extended, and the steady viscous terms were accounted for (Païdoussis et al., 1985). The pressurization in the inner flow was found to be stabilizing. If the outer shell is rigid, pressurization of the annular flow has a destabilizing effect; but, if the outer shell is flexible, the effect could be either stabilizing or destabilizing depending on the system parameters. El Chebair et al. (1990) attempted to improve the model by taking into account the unsteady viscous forces. In that study, some difficulties were encountered with the application of the no-slip boundary condition on the wall. The unsteady viscous forces appeared to have a really small effect on the dynamics of the system; their stabilizing influence was overwhelmed by the opposing effect of the steady viscous forces.

Following the same kind of method, Païdoussis et al. (1991) studied the stability of cantilevered coaxial cylindrical shells conveying incompressible fluid. The steady viscous effects were taken into account and the fluid flow beyond the free end was determined by an ‘‘outflow model’’. They found that, in the case of inner flow, the system first loses stability by flutter in both inviscid and viscous theory. For annular flow, flutter was predicted by inviscid theory, whereas viscous theory assumed that the system would first lose stability by divergence and then by flutter. The viscous terms were found to destabilize the system *vis-à-vis* the annular flow but to stabilize it for internal flow. The presence of internal flow in addition to annular flow tends to stabilize the system at low flow velocities but to destabilize it at higher flow velocities. The same effects arise if the main flow is the internal one. Later, Païdoussis et al. (1992) studied the effect of the system parameters. It was found that increasing the length of the shells, decreasing the annular gap width or decreasing the shell thickness destabilizes the system.

El Chebair et al. (1989) conducted some experiments to observe the dynamics of annular-flow-induced instabilities of cylindrical clamped-clamped or clamped-free shells. For the clamped-clamped shells, the experimental observations show that the system first loses stability by buckling as predicted by the theory. But the coupled-mode flutter predicted by theory was never observed. The cantilevered system loses stability by a single degree of freedom flutter. In both cases, it was also pointed out that increasing the length-to-radius ratio or the gap-to-radius ratio destabilizes the system. Nguyen et al. (1993) conducted some experiments too, but in the case of a cantilevered shell concentrically located within a rigid cylinder only. It was observed that for annular flow, the system first loses stability, generally by flutter but sometimes by divergence, followed by flutter at higher flow velocity. For internal flow the first instability is flutter. The same observations were made regarding the effects of the parameters of the system. The experiments are in generally good agreement with the theory.

Some works were also undertaken considering a coaxial system in which the internal and annular flows are not independent. The study of such systems was motivated by the problem of the patented drill-string described by Den Hartog (1969). In this system, the water is conveyed downwards in the cantilevered pipe and then flows upward around the cantilever as a confined annular flow. The work of Luu (1983) was revisited by Païdoussis et al. (2008). The main results of this work show that for a wide annulus, the dynamics of the system is dominated by the internal flow so that the system is damped at low flow velocities but loses stability by flutter at higher flow velocities. For narrower annuli, the dynamics of the system is overwhelmed by the annular flow. The main effect is to destabilize the system, and flutter occurs at really low flow velocities. Rinaldi (2009) undertook experimental work to compare with these theoretical results. Qualitatively, the system loses stability at very low flow velocity regardless of the amount of confinement. She also found that it behaves as a free-clamped cylinder, i.e. a cantilevered cylinder subjected to axial flow directed from the free end to the clamped on, which Rinaldi also studied in her work. Increasing the flow velocity induces higher vibration frequencies and amplitudes. Increasing the velocity further, the system becomes chaotic and impacts the sides of the rigid annular channel surrounding the pipe. Even if the flutter was well predicted by theory, it appeared that the experimental results were not in good agreement with the theoretical ones, paving the way to some suggestions for future work.

1.2.4 Cantilevered Cylindrical Structures Aspirating Fluids

The early interest in the dynamics of aspirating cantilevered pipes, i.e. with the fluid entering the free end and then flowing upward towards the clamped one, was aroused by its use in “ocean mining”. The system consists in a large vacuum cleaner with a “miner” at the end of the pipe in contact with the sea floor. If, for any reason, this contact is broken, the system becomes an aspirating cantilever pipe. Some recent developments have given added impetus to the necessity of knowing if the system will become unstable at low flow velocity. Specifically, to gain time and money, companies would prefer to liquefy the natural gas directly where it is extracted. In this process, cold water is aspirated by long pipes really deep in the ocean. For the well-being of people and equipment, flutter in that kind of system has to be avoided.

The first attempt to study such a system was conducted by Païdoussis in the mid-1960s. The dynamics was explored experimentally at the Chalk River Nuclear Laboratories in Ontario. Although flutter was expected, it never occurred at any experimental flow velocity. The work was abandoned because of the shell-type collapse of the pipe near the support due to the induced large negative transmural pressure. The effect of reinforcing the pipe was just to postpone the collapse to a higher flow.

In the past twenty years, a lot of theories have been developed in an attempt to predict if flutter will occur and the critical velocity if necessary. The first general theoretical study has been undertaken by Païdoussis and Luu (1985). The equations of motion including the effect of gravity, buoyancy, added mass, an end-mass and viscous damping were derived considering the conventional boundary conditions (i.e. the bending moment and shear forces were assumed to be zero at the free end). The result was essentially obtained by replacing +U by -U in the equations of motion of a cantilevered pipe discharging fluid. Naturally, the mirror-image behaviour of this system was theoretically predicted: the system was shown to lose stability by flutter at infinitesimal flow velocities in the absence of dissipation and then to regain stability at a higher flow rate. Here the direction of the inlet flow was considered to remain tangential to the deflected pipe. A little later, an experimental investigation was conducted at McGill University. In the new apparatus, the pipe was hung vertically and was totally immersed in water in a steel tank. The water was supplied into the tank and forced into the pipe and out of the tank. Several experiments were conducted with different pipe thicknesses and different-shaped inlet forms. As flutter was never observed, the pressure was continuously increased to get a higher flow rate. But the experiment was finally abandonned when water was spread all over the laboratory because the hose leading the water to the tank burst free of its clamp.

Subsequently, it was not before 1995 and a discussion between Prof. M.P. Païdoussis and Dr D.J. Maull of Cambridge University linking this problem with Feynman’s aspirating rotary-sprinkler quandary that the investigation resumed. Païdoussis (1998, 1999) revisited the problem both theoretically and experimentally and came to the conclusion that ‘’aspirating pipes do not flutter at infinitesimally small flow’’. They conducted an experiment in which two flexible elastomer pipes fitted with elbows at their free end, hanging vertically in water, were connected via a pump. Thus one was aspirating flow and the other discharging it. Once again, no flutter was observed. The main theoretical device to explain the contradiction between theory and experiment was to find a correct description of the flow field in the vicinity of the inlet, as it was made clear that it is not a reverse jet but rather a sink flow. Here the main new idea was to consider a pressure drop at the intake of the pipe. This depressurization was shown to cancel out the centrifugal force. This effect would explain the stability of the system. But it was not long before Kuiper and Metrikine (2005) raised some doubts concerning the previous analysis. They pointed out that the depressurization influences the general dynamics of the system only slightly and that the system could lose stability, even in the absence of centrifugal force, by the action of Coriolis force alone. Furthermore, the depressurization might have been overestimated and should finally lie between $-\rho U^2$ and $-\frac{1}{2}\rho U^2$; the centrifugal force may in fact not cancel out. To explain the paradox, they suggested that the external hydrodynamic drag on the pipe is a major stabilizing factor and the viscosity of the surrounding fluid has to be taken into account. Thus having a correct description of both the flow field around the free end and the viscous damping due to the surrounding fluid seems of great importance.

For these reasons, Païdoussis (2005) reevaluated the problem by developing a new set of boundary conditions, considering the pressure drop at the inlet as well as a tensioning effect induced by the flow near the free end. A new description of the boundary conditions was developed assuming that forces are exerted at the inlet of the pipe because of a change of momentum of the entering fluid. The basic theory assumes that the mean flow remains unchanged in the vertical direction and no tensioning effects are considered. The system, stable at low flow velocity, buckled at higher flow rate. Variants of the model (Païdoussis et al., 2005) were developed allowing the intake flow to remain tangential to the deflected pipe and also considering tensioning effects and dissipation. It was found that the occurrence of flutter of the system depended on some parameters related to the tensioning effect ($\overline{\gamma}$), the change of flow velocity ($\alpha = V/U$ with V being the velocity near the inlet), the flow direction (δ_s=0 or 1 for vertical or tangential entry) at the free end, and the dissipation in the pipe and from the surrounding fluid. It was concluded that it would be of particular interest to have CFD simulations to better understand what happens near the intake. Some work started on this at McGill in 2005 and is discussed later.

On their side, Kuiper et al. (2007) tried to improve the description of the hydrodynamic drag, but their results did not meet their expectations and they decided to undertake experiments with a long pipe (Kuiper and Metrikine, 2008). In this new set-up, a cantilevered plastic pipe, about 5 m long with a diameter of 0.1 m, was partially submerged in water. For the first time, it was observed that for a sufficiently high flow velocity, an aspirating cantilevered pipe can lose stability. But, above this critical velocity, the behaviour of the pipe is a complex motion combining two phases: a nearly periodic orbital motion alternating with a noise-like vibration of small amplitude. The experimental results were compared to existing theory. Although the main frequency is well predicted, it was not possible to predict the unsteady unstable motion, the amplitude of the steady state orbital motion, and the critical flow velocity at the onset of flutter. These results elicit the necessity to further study the problem.

Independently of the above, in the recent past, Giacobbi (2007), Giacobbi et al. (2008), Païdoussis (2008) and Rinaldi (2009) carried out a general experimental, theoretical and numerical investigation of this problem. Using a computational fluid dynamics and finite element analysis model in ANSYS, Giacobbi undertook a numerical simulation of the problem. Some problems concerning length of the computing periods and mesh deformation were encountered, but this method gave some significant results. First, the aim of the initial numerical experiment was to study the flow field in the vicinity of the intake to get a good estimation of the parameters $\overline{\gamma}$, α and δ_s. Then, the stability of the system was investigated and it was shown that it is definitely subject to flutter at flow velocities in the range of those observed experimentally. This numerical investigation is still being pursued. A review of the analytical model was performed by Rinaldi (2009). She rederived the equations of motion including the effect of gravity and modified it. Considering that the force exerted at the intake does not materialize instantaneously, two distinct time-delays are included in the equations, one for each component of this force. New experiments in air were also conducted and it was shown that for an appropriate set of axial and lateral time delay values, the theoretical and experimental results are in good agreement. The system loses stability by flutter in its first mode. However, it is worth pointing out that Rinaldi also observed an unexplainable and intermittent shuddering motion characterized by a decrease of the amplitude of the system, and a shell-type collapse of the free end of the cantilevered pipe in the absence of a stiffening end-piece.

Chapter 2: Dynamics of a Cantilevered Shell Aspirating Fluid

2.1 Introduction

As presented in Chapter 1, a lot of work has been carried out on the subject of cantilevered shell aspirating fluid over the past years. If it was first motivated by fundamental interest, it recently appears necessary to investigate this problem, as industrial installations now utlizise this kind of system; e.g. in boats liquefying the gas on board. Experiments were conducted a few years ago by Rinaldi (2009) at McGill University, Montreal, Canada. Her experiments involved a thick-walled cantilevered pipe that was aspirating air. It, unexpectedly, experienced a shell-type instability at rather low flow velocity. Although she by-passed the problem by adding a stabilising end-piece, the question of the stability of cantilevered shell arose.

In this Chapter, an analytical model of this problem will be developed. The equations of motion will first be derived; a method to find solution to these equations will then be presented. It will be followed by a discussion about the theoretical results and the experimental observations.

2.2 Equations of Motion

For the shell under consideration, the configuration is presented in Figure 2.1.a. It consists of a flexible cantilevered cylindrical shell aspirating fluid. The shell is characterized by a length L, a radius a, a wall thickness h, a cross-sectional flow area A, a density ρ_s, a Young's modulus E and a Poisson's ratio v. The fluid has density ρ_f and a velocity U inside the shell. The cylindrical coordinate system (r, ϑ, x) shown in Figure 2.1.b is used due to cylindrical nature of the system. Its origin is located on the tube axis at the clamped end of the shell. The displacement components of the middle surface are *u*, *v* and *w* with w being positive outward.

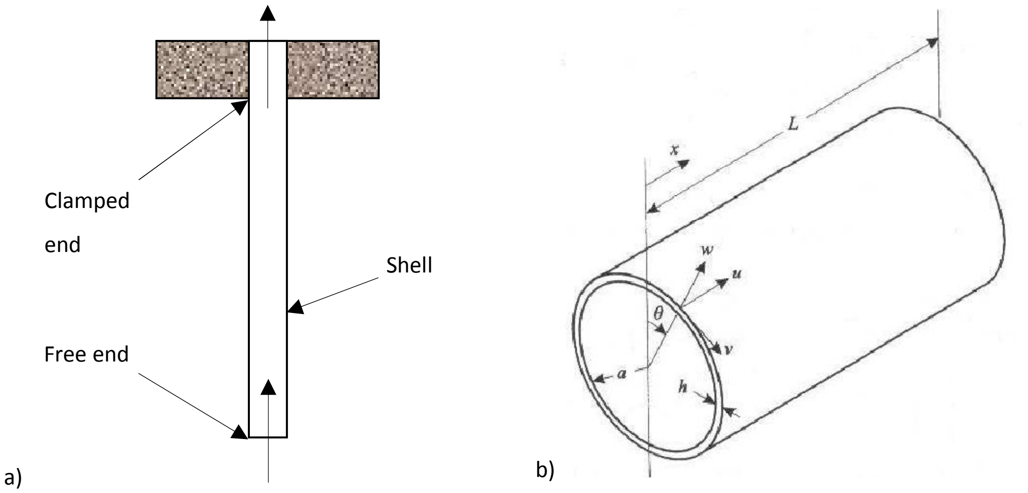

Figure 2.1: a) A cantilevered shell aspirating fluid and b) the coordinate system and some key dimensions [Païdoussis et al. (2005)]

2.2.1 Model Assumptions

In order to develop a first mathematical model for this configuration, some assumptions need to be made. First of all, we shall consider only small deformations of the middle surface of the shell. The important consequence of this hypothesis is that it allows to describe this problem using a linear theory. For this purpose, we employ the modified Flügge theory based on the following assumptions:

(1) the shell is sufficiently thin compared with the least radius of curvature of the reference surface, i.e. $h/a \ll 1$;
(2) the strains are small enough for Hooke's law to hold;
(3) the stress acting in the direction normal to the reference surface is negligible compared with the stresses acting in a direction parallel to the middle surface;
(4) any straight line normal to the undeformed reference surface remains straight and normal to the deformed reference surface and their length is not affected;

(5) in deriving the expressions for strain and stress resultants, second order terms are retained; this means that terms of orders up to $(h/a)^2$ are taken into account.

The first four hypotheses constitute the classical theory of shells proposed by Love in 1888 and presented in his book (1927). All these assumptions are relative to the shell. Regarding the fluid flow, we consider it as a potential flow and the fluid to be incompressible. This means that the flow is irrotational, inviscid, non-heat-conducting, homogeneous and incompressible. However, we will take into account steady viscous effects and pressurization effects in this theory. And, when it comes to calculating friction-related stress resultants, we consider the flow to be a fully-developed turbulent flow. In this theory, the shell is subjected to two kinds of load: a static part and a time dependent one. The magnitude of the steady components, called basic loads, is much larger than the other ones, viewed as additional loads. Finally, the shell is pre-stressed by a constant axial force per unit surface area, p_{x0}, and an axially symmetric pressure, p_0. These forces generate a basic axial stress, N_{x0}, and a basic hoop stress, $N_{\theta 0}$. So that the stress resultants N_x and N_θ and the loads p_x^* and p_z^* represented in the Figure 2.2 are the combination of the former components and an additional time-varying part:

$$\begin{cases} p_z^* = p_0 + p_1, \\ p_x^* = p_{x0} + p_{x1}, \\ N_x = N_{x0} + N_{x1}, \\ N_\theta = N_{\theta 0} + N_{\theta 1}. \end{cases} \tag{2.1}$$

All the other components consist only of an additional part and will not be denoted by any subscript.

As we are using air in the experiments, the incompressibility assumption may seem inappropriate but the velocity is sufficiently small for this assumption to hold.

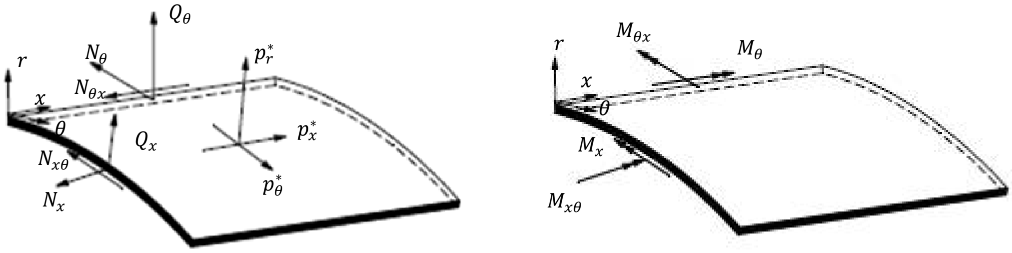

Figure 2.2: Stress and moment resultants acting on a shell element

2.2.2 Derivation of the Fundamental Equations

The derivation is carried out in two major parts following the lead of Yamaki's book (1984):

(i) obtaining the expressions of the time-dependent stress resultants and stress couples;
(ii) deriving the equations through a variational principle.

Here, we will just describe the most important steps in the employed method; more elaborate explanations are presented in Appendices A and B. The definitions of the stress resultants and moments are defined in the first chapter of Flügge's book (1973). To obtain the relevant expressions in our particular case, we first need to express the displacement of an arbitrary point of the shell according to the displacement of the point located on the reference surface. Then, we can define the strain expression considering only ε_x, ε_θ and $\gamma_{x\theta}$. Using assumptions 2 and 3, we determine the corresponding stresses. Introducing them in the definitions of the stress resultants and couples, we get their final expressions (Appendix A).

Before applying the variational principle, we have to determine the expressions of the variation of the elastic strain energy and of the potential of the external force. The first one is given by

$$U_e = \frac{1}{2}\int_0^L \int_0^{2\pi a} \int_{-h/2}^{h/2} (\sigma_{xx}\varepsilon_x + \sigma_{\theta\theta}\varepsilon_\theta + \sigma_{x\theta}\gamma_{x\theta})\left(1 + \frac{z}{a}\right) a dx d\theta dz, \tag{2.2}$$

and the variation of this elastic strain energy is expressed as

$$\delta U_e = \int_0^L \int_0^{2\pi a} \int_{-h/2}^{h/2} (\sigma_{xx}\delta\varepsilon_x + \sigma_{\theta\theta}\delta\varepsilon_\theta + \sigma_{x\theta}\delta\gamma_{x\theta})\left(1+\frac{z}{a}\right) a dx d\theta dz. \qquad (2.3)$$

To express the variation of the potential of the external force, we have to consider the deformation of the shell. Indeed, to consider all the terms of first order in the equations of motion, we have to remember that one component of the loads is of zero order. As a result, the product of the latter with a displacement or its derivative is of order one and has to be taken into account. Finally, the expression of this variation is given by

$$\begin{aligned} \delta V_f = -\int_0^L \int_0^{2\pi a} \Bigg\{ & p_x^* \left[\left(1 + u_{,x} + \frac{v_{,\theta} + w}{a}\right)\delta u + v_{,x}\,\delta v\right] + p_\theta^* \delta v \\ & - p_z^* \Bigg[w_{,x}\,\delta u + \frac{w_{,\theta} - v}{a}\delta v \\ & - \left(1 + u_{,x} + \frac{v_{,\theta} + w}{a}\right)\delta w \Bigg]\Bigg\} a dx d\theta \\ & - \int_0^{2\pi a} [P_x^*\delta u + P_\vartheta^*\delta v - P_z^*\delta w + M_x^*\delta w_{,x}\,]_{x=0}^{x=L} a d\theta, \end{aligned} \qquad (2.4)$$

where P_x^*, P_ϑ^*, P_z^* and M_x^* are respectively the three components of the external load and the bending moment applied to the edge of the shell. If the additional load acting on the pre-stressed shell has only a radial component, $p_x^*, p_\vartheta^*\ and\ p_z^*$ consist in the association of the basic loads presented in equation (2.1), the acceleration terms and the radial additional load for the last one:

$$\begin{cases} p_x^* = p_{x0} - \rho_s h \dfrac{\partial^2 u}{\partial t^2}, \\ p_\theta^* = -\rho_s h \dfrac{\partial^2 v}{\partial t^2}, \\ p_z^* = p_0 + q - \rho_s h \dfrac{\partial^2 w}{\partial t^2}, \end{cases} \qquad (2.5)$$

where *q*, as it is a radial load, is given by the difference between the fluid pressure inside the shell, p_i, and the fluid pressure outside the shell, p_e:

$$q = p_i - p_e|_{r=a} \tag{2.6}$$

The variational principle states that

$$\delta U_e + \delta V_f = 0. \tag{2.7}$$

Developing this expression and keeping only the terms of zero order, we get

$$\begin{cases} \dfrac{\partial N_{x0}}{\partial x} = -p_{x0}, \\ \dfrac{\partial N_{\theta 0}}{\partial \theta} = 0, \\ p_0 = \dfrac{N_{\theta 0}}{a}. \end{cases} \tag{2.8}$$

At the zero order, the shell can be considered as an axially symmetric pipe; so, neither N_{x0} or $N_{\theta 0}$ will depend of the ϑ component. p_{x0} represents the wall shear stress of a fully-developed pipe flow. Whether it is laminar or turbulent, it has been shown by Fox et al. (2009) that

$$p_{x0} = -\frac{1}{8}\lambda_f \rho_f U^2, \tag{2.9}$$

where λ_f is the friction factor given in Fox et al. (2009). To get the pressure distribution along the shell, we simply have to consider the equilibrium of a small section of the fluid inside a pipe. It is only subjected to steady pressure and steady viscous effect. The length of this region being *dx* and the radius *a*, we obtain

$$\left(p_0 + \frac{\partial p_0}{\partial x} dx\right)\pi a^2 - p_0 \pi a^2 + p_{x0} 2\pi a dx = 0, \tag{2.10}$$

so that

$$\frac{\partial p_0}{\partial x} + 2\frac{p_{x0}}{a} = 0. \tag{2.11}$$

Integrating equation (2.11) along the shell, we get

$$p_0(x) = 2\frac{p_{x0}}{a}(L - x) + \frac{C_2}{a}, \tag{2.12}$$

and from equations (2.8), we obtain

$$\begin{cases} N_{x0} = p_{x0}(L - x) + C_1, \\ N_{\theta 0} = 2p_{x0}(L - x) + C_2, \end{cases} \tag{2.13}$$

where C_1 and C_2 are constant, depending only on the boundary conditions. This will be discussed later.

Hence, we finally obtain the equations of motion:

$$\begin{aligned} L_1(u, v, w) = {} & u'' + \frac{1-\nu}{2}u^{\cdot\cdot} + \frac{1+\nu}{2}v'^{\cdot} + \nu w' \\ & + k_a\left[\frac{1-\nu}{2}u^{\cdot\cdot} - w''' + \frac{1-\nu}{2}w'^{\cdot\cdot}\right] + \tau_x u'' \\ & + \tau(v^{\cdot} + w) + \tau_\theta(u^{\cdot\cdot} - w') - \gamma\frac{\partial^2 u}{\partial t^2} = 0, \end{aligned} \tag{2.14}$$

$$\begin{aligned} L_2(u, v, w) = {} & \frac{1+\nu}{2}u'^{\cdot} + v^{\cdot\cdot} + \frac{1-\nu}{2}v'' + w^{\cdot} \\ & + k_a\left[3\frac{1-\nu}{2}v'' - \frac{3-\nu}{2}w''^{\cdot}\right] + \tau_x v'' + \tau_\theta(v^{\cdot\cdot} + w^{\cdot}) \\ & - \gamma\frac{\partial^2 v}{\partial t^2} = 0, \end{aligned} \tag{2.15}$$

$$\begin{aligned} L_3(u, v, w) = {} & \nu u' + v^{\cdot} + w \\ & + k_a\left[\frac{1-\nu}{2}u'^{\cdot\cdot} - u''' - \frac{3-\nu}{2}v''^{\cdot} + \nabla^4 \mathrm{w} + 2\mathrm{w}^{\cdot\cdot} \right. \\ & \left. + \mathrm{w}\right] - \tau_x w'' - \tau_\theta(u' - v^{\cdot} + w^{\cdot\cdot}) + \gamma\left[\frac{\partial^2 w}{\partial t^2} - \frac{q}{\rho_s h}\right] \\ & = 0, \end{aligned} \tag{2.16}$$

where

$$(\ )^{\cdot} = \frac{\partial}{\partial\theta}, \qquad (\ )' = a\frac{\partial}{\partial x}, \qquad k_a = \frac{1}{12}\left(\frac{h}{a}\right)^2, \qquad \gamma = \frac{\rho_s a^2(1-\nu^2)}{E}$$

$$\nabla^2 = \mathrm{a}^2\frac{\partial^2}{\partial \mathrm{x}^2} + \frac{\partial^2}{\partial \theta^2}, \qquad \{\tau_x, \tau, \tau_\theta\} = \frac{1-\nu^2}{Eh}\{N_{x0}, ap_{x0}, N_{\theta 0}\}.$$

2.2.3 Boundary Conditions

From the variational principle (see Appendix B) used in the Section 2.2.2, we can get the usual boundary conditions for a cantilevered shell:

$$\begin{array}{ll} at\ x = 0: & u = v = w = \dfrac{\partial w}{\partial x} = 0; \\ at\ x = L: & \begin{cases} aN_{x0} = P_x^*, \\ aN_{\theta 0} = P_\vartheta^*, \\ N_{x1} = 0, \\ N_{x\theta} - \dfrac{M_{x\theta}}{a} = 0, \\ M_x = 0, \\ aM_{x,x} + M_{x\theta,\theta} + M_{\theta x,\theta} = 0. \end{cases} \end{array} \quad (2.17)$$

But here we are considering a shell that is aspirating fluid, so that the intake of the shell is not stress-free. We have to consider that forces are exerted at this end due to the fluid entering the shell. The configuration of the vibrating end of a shell is presented in Figure 2.3.a. Because of the circular shape of the shell, the direction of the flow velocity depends of the position along the circumference of the intake. That is why we will determine the fluid forces acting on a small part of the free end inclined at an angle $\chi \equiv \tan^{-1}(w_{,x})_L \approx (w_{,x})_L$. Before entering the shell, the flow velocity is V, and upon entering the shell it becomes U. As we consider shell vibrations, V will remain vertical. So that the norm and the direction of the fluid velocity change at the intake inducing a change in momentum, $mU\Delta U$. To determine the expression of the mass m, we consider that the force exerted on the considered part of the intake is only due to the change of momentum of the fluid going through the region whose area is A_1 represented in Figure 2.3.b and that the fluid flow is equally distributed among the cross section:

$$m = \frac{M}{2\pi} d\theta, \quad (2.18)$$

where $M = \rho_f \pi a^2$ is the mass of fluid per unit length of the shell.

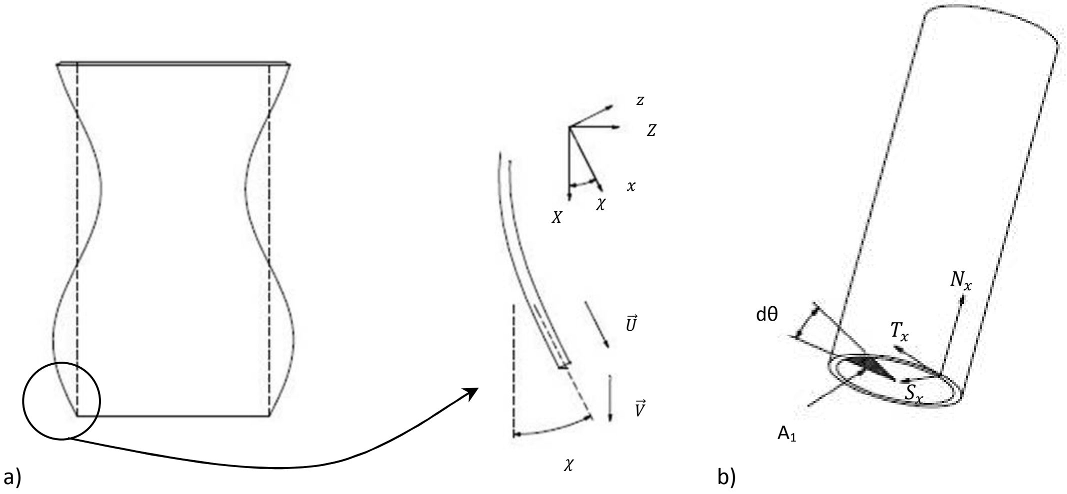

Figure 2.3: a) A cylindrical shell showing the configuration of a shell element at the free end and b) the forces acting on it.

Because of this phenomenon, a force that we separate in two components arises:

$$F_X = \frac{Md\theta}{2\pi} U(V - U\cos\chi), \tag{2.19}$$

$$F_Z = \frac{Md\theta}{2\pi} U\left(0 - \left(U\sin\chi + \frac{\partial w}{\partial t}\right)\right), \tag{2.20}$$

where $\alpha = V/U$. As χ is supposed to be small, $\cos\chi \approx 1$ and $\sin\chi \approx w,_x|_L$, and thus

$$F_X = -\frac{Md\theta}{2\pi} U^2(1-\alpha), \tag{2.21}$$

$$F_Z = -\frac{Md\theta}{2\pi} U(w,_t|_L + Uw,_x|_L). \tag{2.22}$$

These are the forces exerted by the shell on the fluid. But we are interested in the reaction: the forces exerted on the shell,

$$F_X^* = \frac{Md\theta}{2\pi} U^2(1-\alpha), \tag{2.23}$$

$$F_Z^* = \frac{Md\theta}{2\pi} U(w,_t|_L + Uw,_x|_L). \tag{2.24}$$

Therefore the fluid forces acting at the shell intake in the *x*- and *z*-direction (see Figure 2.3.b) are:

$$F_x^* = \frac{Md\theta}{2\pi} U^2 (1-\alpha), \tag{2.25}$$

$$F_z^* = \frac{Md\theta}{2\pi} U (w,_t|_L + U\alpha w,_x|_L). \tag{2.26}$$

It is now supposed that the force F_x^* is due to the pressure drop at the shell intake. We also have to consider that a compression force, *T*, is acting on the lips of the shell. Then,

$$-\bar{p}A_1 = F_x^* = \frac{Md\theta}{2\pi} U^2 (1-\alpha), \tag{2.27}$$

$$\begin{aligned} T = -\gamma\bar{p}(A_0 - A_1) &= \gamma \frac{A_0 - A_1}{A_1} \frac{Md\theta}{2\pi} U^2 (1-\alpha) \\ &= \bar{\gamma} \frac{Md\theta}{2\pi} U^2 (1-\alpha), \end{aligned} \tag{2.28}$$

where $\bar{p} = p_0(L)$, A_0 is the outer sectional area of the region considered and $\bar{\gamma} = \gamma \frac{A_0 - A_1}{A_1}$. Finally, the force acting at the shell intake in the x-direction is

$$T - \bar{p}A_1 = \frac{Md\theta}{2\pi} U^2 (1-\alpha)(1+\bar{\gamma}). \tag{2.29}$$

It is of order zero and it allows us to determine the constant C_1 of (2.13):

$$ad\theta N_{x0}(L) = T - \bar{p}A_1 = \frac{Md\theta}{2\pi} U^2 (1-\alpha)(1+\bar{\gamma}), \tag{2.30}$$

yielding

$$N_{x0}(L) = C_1 = \frac{\rho_f a}{2} U^2 (1-\alpha)(1+\bar{\gamma}). \tag{2.31}$$

Furthermore, we know that $N_{\theta 0}(L) = a\bar{p}$, and from (2.27) we get

$$N_{\theta 0}(L) = C_2 = -\frac{\rho_f a}{2} U^2 (1-\alpha). \tag{2.32}$$

Equation (2.26) is of the first order. That is why it has to be inserted in the expression of the boundary conditions. As the force is in the direction of the *z*-axis, only the fourth expression of (2.17) changes and it becomes

$$\frac{M}{2\pi}U(w_{,t}|_L + U\alpha w_{,x}|_L) - (aM_{x,x} + M_{x\theta,\theta} + M_{\theta x,\theta}) = 0 \; at \; x = L. \qquad (2.33)$$

Finally, we get the expressions of all the boundary conditions in terms of displacement

$$R_1(u,v,w) = u' + \nu v^{\cdot} + \nu w - kw'' = 0, \qquad (2.34)$$

$$R_2(u,v,w) = u^{\cdot} + v' + 3k(v' - w'^{\cdot}) = 0, \qquad (2.35)$$

$$R_3(u,v,w) = w'' + \nu w^{\cdot\cdot} - \nu v^{\cdot} - u' = 0, \qquad (2.36)$$

$$\begin{aligned} R_4(u,v,w) = -w''' - (2-\nu)w'^{\cdot\cdot} + \frac{3-\nu}{2}v'^{\cdot} - \frac{1-\nu}{2}u^{\cdot\cdot} \\ +u'' + \frac{\rho_f a^2}{2}U(w_{,t}|_L + U\alpha w_{,x}|_L) = 0. \end{aligned} \qquad (2.37)$$

2.2.4 Dynamics of the Fluid Flow

In the equations of motion, we still need to develop the expression of the perturbation pressure inside and outside of the shell. Recalling that the fluid flow we consider is irrotational, inviscid, homogeneous and incompressible, we will use potential flow theory. It specifies that the velocity $\vec{V}$ can be expressed by a velocity potential $\Psi(x,\theta,r,t)$:

$$\vec{V} = \vec{\nabla}\Psi. \qquad (2.38)$$

From the former analysis, the potential Ψ can be separated into two components: a steady one giving the mean flow velocity *U* in the *x*-direction and a disturbed component defined by the scalar $\Psi(x,\theta,r,t)$. The same is also true for the pressure:

$$\Psi = Ux + \psi, \qquad (2.39)$$

$$P = p_0 + p. \qquad (2.40)$$

Hence, the general expressions of the flow and pressure fields are given by

$$V_x = U + \frac{\partial \psi}{\partial x}, \qquad V_\theta = \frac{1}{r}\frac{\partial \psi}{\partial \theta}, \qquad V_r = \frac{\partial \psi}{\partial r}. \tag{2.41}$$

The fluid flow being incompressible and irrotational, the velocity potential is governed by the Laplace equation:

$$\nabla^2 \Psi = \frac{\partial^2 \psi}{\partial \mathrm{r}^2} + \frac{1}{\mathrm{r}}\frac{\partial \psi}{\partial \mathrm{r}} + \frac{1}{\mathrm{r}^2}\frac{\partial^2 \psi}{\partial \theta^2} + \frac{\partial^2 \psi}{\partial \mathrm{x}^2} = 0. \tag{2.42}$$

It also has to respect the impermeability condition at the wall:

$$\left.\frac{\partial \psi}{\partial \mathrm{r}}\right|_{\mathrm{r}=\mathrm{a}^-} = \begin{cases} \dfrac{\partial \mathrm{w}}{\partial \mathrm{t}} + U\dfrac{\partial \mathrm{w}}{\partial \mathrm{x}} & \text{for } 0 \le \mathrm{x} \le \mathrm{L} \\ 0 & \text{for } \mathrm{x} < 0 \; and \; x > L \end{cases} \tag{2.43}$$

$$\left.\frac{\partial \psi}{\partial \mathrm{r}}\right|_{\mathrm{r}=\mathrm{a}^+} = \begin{cases} \dfrac{\partial \mathrm{w}}{\partial \mathrm{t}} & \text{for } 0 \le \mathrm{x} \le \mathrm{L} \\ 0 & \text{for } \mathrm{x} < 0 \; and \; x > L \end{cases} \tag{2.44}$$

Here, we should say some words about the boundary conditions of the potential ψ at the intake and outlet of the shell. At the clamped end, it is natural to assume that ψ vanishes for all *x*<0. On the contrary, we cannot assume the same where the shell is free to move. We have to consider that the fluid is already perturbed when entering the shell. That is why we need to elaborate a model to specify the evolution of the velocity potential and of the fluid pressure for $L < x \le L'$, where L' is the position where both quantities are equal to zero. The elaboration of this model will be discussed in Section 2.3.2, once we have determined the general form of the solution.

Finally, the unsteady pressure and potential are related to each other through the Bernouilli's equation:

$$\frac{\partial \psi}{\partial t} + \frac{V^2}{2} + \frac{P}{\rho_f} = \frac{P_s}{\rho_f}, \tag{2.45}$$

where P_s is the stagnation point pressure.

We finally have:

$$\left[p_0 - P_s + \rho_f \frac{U^2}{2}\right] + \left[\rho_f \frac{\partial \Psi}{\partial t} + \rho_f U \frac{\partial \Psi}{\partial x} + p\right] + \frac{1}{2}\rho_f \left[\left(\frac{\partial \Psi}{\partial x}\right)^2 + \left(\frac{1}{r}\frac{\partial \Psi}{\partial \theta}\right)^2 + \left(\frac{\partial \Psi}{\partial r}\right)^2\right] = 0. \tag{2.46}$$

The first term of (2.46) is time-independent but the second one is not. The third is non-linear and will be neglected. As a consequence, each of these terms is equal to zero:

$$p_0 = P_s - \rho_f \frac{U^2}{2}, \tag{2.47}$$

$$p = -\rho_f \left(\frac{\partial \Psi}{\partial t} + U \frac{\partial \Psi}{\partial x}\right). \tag{2.48}$$

2.3 Method of Solution

2.3.1 General Form of the Solution

To find solutions of the problem presented in the previous section, we have to consider two different sets of equations referring to the dynamics of the fluid and to the motion of the shell.

The expression of the pressure drop between the inner fluid and the outer fluid is governed by the equations (2.42) to (2.44) and (2.48). To solve this set of equations, we shall use the Fourier-Transform Generalized-Force method that was used by Chan (1984). Then, we substitute this solution into the equations of motion. We finally use the extended form of the Galerkin method to solve them.

To satisfy these equations, the general form of the solution we consider is close to the one governing the motion of cantilevered pipe:

$$\begin{Bmatrix} u \\ v \\ w \end{Bmatrix} = \sum_{n=1}^{\infty}\sum_{m=1}^{\infty} \begin{Bmatrix} A_m \cos n\theta \left(a \dfrac{\partial}{\partial x}\right) \\ B_m \sin n\theta \\ C_m \cos n\theta \end{Bmatrix} \varphi_m(x) e^{i\Omega t}, \tag{2.49}$$

where m and n are respectively the axial and circumferential mode, A_m, B_m and C_m are constants, Ω the frequency of oscillations and φ_m are the eigenfunctions of clamped-free pipe. The expressions of these functions and of the eigenvalues, λ_m, are given in Paidoussis (1998). They do not satisfy the boundary conditions of a cantilevered shell. That is why we have to use the extended Galerkin method and look for a series-form solution.

Considering the general form of the displacement, the expression of the unsteady pressure and velocity potential is given by

$$\begin{Bmatrix} \psi_i \\ p_i \end{Bmatrix} = \sum_{n=1}^{\infty} \begin{Bmatrix} \bar{\psi}_i(x,r) \\ \bar{p}_i(x,r) \end{Bmatrix} \cos n\theta \, e^{i\Omega t}, \tag{2.50}$$

$$\begin{Bmatrix} \psi_o \\ p_o \end{Bmatrix} = \sum_{n=1}^{\infty} \begin{Bmatrix} \bar{\psi}_o(x,r) \\ \bar{p}_o(x,r) \end{Bmatrix} \cos n\theta \, e^{i\Omega t}, \tag{2.51}$$

where the subscript *i* denotes the inner fluid properties and *o* the outer fluid ones.

2.3.2 Expression of the Unsteady Pressure

As explained before, we use a Fourier-Transform method to obtain the expression required. The Fourier transform of a function *f(x,r)* is given by

$$f^*(\alpha,r) = \int_{-\infty}^{+\infty} f(x,r) e^{i\alpha x} dx, \tag{2.52}$$

and its inverse is

$$f(x,r) = \frac{1}{2\pi} \int_{-\infty}^{+\infty} f^*(\alpha,r) e^{-i\alpha x} d\alpha, \tag{2.53}$$

where α should not be confused with that in Section 2.2.3.

First, we introduce the expression of the velocity potential into (2.42). The result is the same for both internal and external problems and we suppress the subscript here:

$$\sum_{n=1}^{\infty}\left(\frac{\partial^2\overline{\psi}}{\partial \mathrm{r}^2}+\frac{1}{\mathrm{r}}\frac{\partial\overline{\psi}}{\partial \mathrm{r}}-\frac{\mathrm{n}^2}{\mathrm{r}^2}\overline{\psi}+\frac{\partial^2\overline{\psi}}{\partial \mathrm{x}^2}\right)\cos n\theta = 0. \tag{2.54}$$

We then take the Fourier transform:

$$\sum_{n=1}^{\infty}\left(\frac{\partial^2\overline{\psi}^*}{\partial \mathrm{r}^2}+\frac{1}{\mathrm{r}}\frac{\partial\overline{\psi}^*}{\partial \mathrm{r}}-\left(\alpha^2+\frac{\mathrm{n}^2}{\mathrm{r}^2}\right)\overline{\psi}^*\right)\cos n\theta = 0. \tag{2.55}$$

As this infinite series in $\cos n\theta$ is identically equal to zero, each term has to vanish:

$$\forall n, \qquad \frac{\partial^2\overline{\psi}^*}{\partial \mathrm{r}^2}+\frac{1}{\mathrm{r}}\frac{\partial\overline{\psi}^*}{\partial \mathrm{r}}-\left(\alpha^2+\frac{\mathrm{n}^2}{\mathrm{r}^2}\right)\overline{\psi}^* = 0. \tag{2.56}$$

We recognize the modified Bessel differential equation, whose general solution takes the form

$$\overline{\psi}^* = C_1 I_n(\alpha r) + C_2 K_n(\alpha r), \tag{2.57}$$

where I_n and K_n are the modified Bessel functions of the first and second kinds, and C_1 and C_2 are constants to be determined from the boundary conditions. Now we need to separate the study for the internal and external flow.

For the internal flow, we substitute (2.57) into (2.43), obtaining

$$\begin{aligned}\sum_{n=1}^{\infty}\frac{\partial\overline{\psi}_i}{\partial \mathrm{r}}(x,r)\Big|_{\mathrm{r=a}} &\cos n\theta e^{i\Omega t}\\ &= \sum_{n=1}^{\infty}\sum_{m=1}^{\infty} C_m\left(i\Omega\varphi_m(x)+U\frac{\partial\varphi_m}{\partial \mathrm{x}}\right)\cos n\theta\, e^{i\Omega t}\,;\end{aligned} \tag{2.58}$$

we then take the Fourier transform and we get

$$\sum_{n=1}^{\infty}\frac{\partial\overline{\psi}_{\mathrm{i}}^*}{\partial \mathrm{r}}(\alpha,r)\Big|_{\mathrm{r=a}} \cos n\theta = \sum_{n=1}^{\infty}\sum_{m=1}^{\infty} C_m i(\Omega-\alpha U)\varphi_m^*(\alpha)\cos n\theta. \tag{2.59}$$

For the same reason as before, the coefficients of $\cos n\theta$ have to be equal. Taking the derivative of (2.57), we obtain

$$\left.\frac{\partial \overline{\Psi}_{\mathrm{i}}^{*}}{\partial r}(\alpha, r)\right|_{\mathrm{r=a}} = C_{1i}\alpha I_n'(\alpha a) + C_{2i}\alpha K_n'(\alpha a)$$
$$= i(\Omega - \alpha U)\sum_{m=1}^{\infty} C_m \varphi_m^*(\alpha). \tag{2.60}$$

Since the velocity cannot be infinite for *r*=0, $C_{2i} = 0$ and, therefore,

$$C_{1i} = i\frac{\Omega - \alpha U}{\alpha I_n'(\alpha a)}\sum_{m=1}^{\infty} C_m \varphi_m^*(\alpha). \tag{2.61}$$

Next, from (2.48), we obtain the expression of the Fourier transform of the perturbed internal pressure:

$$p_i^* = -\rho_f i(\Omega - \alpha U)\sum_{n=1}^{\infty} \overline{\Psi}_{\mathrm{i}}^* \cos n\theta = \sum_{n=1}^{\infty} \bar{p}_i^* \cos n\theta. \tag{2.62}$$

Equating the terms in $\cos n\theta$ again, we obtain

$$\bar{p}_i^* = \rho_f \frac{(\Omega - \alpha U)^2}{\alpha}\frac{I_n(\alpha a)}{I_n'(\alpha a)}\sum_{m=1}^{\infty} C_m \varphi_m^*(\alpha). \tag{2.63}$$

Starting again from equation (2.57) but for the external flow and using (2.44), we get:

$$\left.\frac{\partial \overline{\Psi}_{\mathrm{o}}^{*}}{\partial r}(\alpha, r)\right|_{\mathrm{r=a}} = C_{1o}\alpha I_n'(\alpha a) + C_{2o}\alpha K_n'(\alpha a) = i\Omega\sum_{m=1}^{\infty} C_m \varphi_m^*(\alpha). \tag{2.64}$$

As we are dealing with the outer velocity potential, it cannot become infinite as $r \to +\infty$ and thus $C_{1o} = 0$; hence,

$$C_{2o} = i\frac{\Omega}{\alpha K_n'(\alpha a)}\sum_{m=1}^{\infty} C_m \varphi_m^*(\alpha). \tag{2.65}$$

The external perturbation pressure is, therefore,

$$\bar{p}_e^* = \rho_f \frac{\Omega^2}{\alpha}\frac{K_n(\alpha a)}{K_n'(\alpha a)}\sum_{m=1}^{\infty} C_m \varphi_m^*(\alpha). \tag{2.66}$$

Considering the general form of the unsteady pressure, the term q is given by:

$$q = \sum_{n=1}^{\infty} \bar{q}(x,r) \cos n\theta \, e^{i\Omega t} \quad \text{with} \quad \bar{q} = \bar{p}_i - \bar{p}_o|_{r=a}. \tag{2.67}$$

To get the expression of $\bar{q}$, we have to take the inverse Fourier transform of (2.63) and (2.66). But, as it will be more convenient afterwards, we should first nondimensionalize these equations. We define the following reference velocity, frequency and pressure:

$$U_0 = \left[\frac{E}{\rho_s(1-\nu^2)}\right]^{1/2}, \quad \Omega_0 = \left[\frac{E}{\rho_s a^2(1-\nu^2)}\right]^{1/2}, \quad Q_0 = \rho_s h L \Omega_0^2; \tag{2.68}$$

and the dimensionless parameters:

$$\begin{gathered} \bar{U} = \frac{U}{U_0}, \quad \bar{\Omega} = \sqrt{\gamma}\Omega = \frac{\Omega}{\Omega_0}, \quad \varepsilon = \frac{a}{L}, \quad \bar{\alpha} = \alpha L, \\ \xi = \frac{x}{L}, \quad \overline{A_m} = \frac{A_m}{L}, \quad \overline{B_m} = \frac{B_m}{L}, \quad \overline{C_m} = \frac{C_m}{L}. \end{gathered} \tag{2.69}$$

We can therefore express the perturbation pressures as

$$\bar{p}_i^* = \rho_f \frac{LU_0^2}{\bar{\alpha}} \left(\frac{\bar{\Omega}}{\varepsilon} - \bar{\alpha}\bar{U}\right)^2 \frac{I_n(\bar{\alpha}\varepsilon)}{I_n'(\bar{\alpha}\varepsilon)} \sum_{m=1}^{\infty} \overline{C_m} \varphi_m^*(\bar{\alpha}), \tag{2.70}$$

$$\bar{p}_o^* = \rho_f \frac{LU_0^2}{\bar{\alpha}} \left(\frac{\bar{\Omega}}{\varepsilon}\right)^2 \frac{K_n(\bar{\alpha}\varepsilon)}{K_n'(\bar{\alpha}\varepsilon)} \sum_{m=1}^{\infty} \overline{C_m} \varphi_m^*(\bar{\alpha}), \tag{2.71}$$

where $\varphi_m^*(\bar{\alpha}) = \int_{-\infty}^{+\infty} \varphi_m(\xi) e^{i\bar{\alpha}\xi} d\xi$.

Finally we obtain the expression of $\bar{q}$ by taking the difference of the Fourier transform of the two equations above. It has the general form

$$\begin{aligned} \bar{q} = \frac{1}{2\pi} \int_{-\infty}^{\infty} e^{-i\bar{\alpha}\xi} \frac{d\bar{\alpha}}{L} \Bigg\{ \rho_f \frac{LU_0^2}{\bar{\alpha}} \Bigg[\left(\frac{\bar{\Omega}}{\varepsilon} - \bar{\alpha}\bar{U}\right)^2 \frac{I_n(\bar{\alpha}\varepsilon)}{I_n'(\bar{\alpha}\varepsilon)} \\ - \left(\frac{\bar{\Omega}}{\varepsilon}\right)^2 \frac{K_n(\bar{\alpha}\varepsilon)}{K_n'(\bar{\alpha}\varepsilon)} \Bigg] \sum_{m=1}^{\infty} \overline{C_m} \varphi_m^*(\bar{\alpha}) \Bigg\} = \sum_{m=1}^{\infty} \overline{C_m} Q_{mn}(\xi), \end{aligned} \tag{2.72}$$

where

$$Q_{mn}(\xi) = \rho_f \frac{U_0^2}{2\pi} \int_{-\infty}^{\infty} \frac{e^{-i\bar{\alpha}\xi}}{\bar{\alpha}} d\bar{\alpha} \left\{ \left[\left(\frac{\bar{\Omega}}{\varepsilon} - \bar{\alpha}\bar{U} \right)^2 \frac{I_n(\bar{\alpha}\varepsilon)}{I'_n(\bar{\alpha}\varepsilon)} - \left(\frac{\bar{\Omega}}{\varepsilon} \right)^2 \frac{K_n(\bar{\alpha}\varepsilon)}{K'_n(\bar{\alpha}\varepsilon)} \right] \varphi_m^*(\bar{\alpha}) \right\}. \tag{2.73}$$

So far, we considered a simplified model: the unsteady pressure becomes suddenly non-zero when the fluid enters the shell. To get more realistic results, it might be better to consider more elaborate models describing the behaviour of the flow before entering the shell at its free end. Here, we present different models that ensure some continuity of the pressure at the intake of the shell and where the pressure is close to zero at a finite distance *l* ahead of the intake. The characteristics of the models are as follows:

- Model 1: continuity of the pressure at ξ=1 and ξ=*l*;
- Model 2: continuity of the pressure at ξ=1 and ξ=*l* and of its derivative at ξ=1;
- Model 3: continuity of the pressure and its derivative at ξ=1 and ξ=*l*;
- Model 4: continuity of the pressure and its derivative at ξ=1 and ξ= *l*, $l \to +\infty$.

To implement the above, in the previous equations, we replace φ_m by $\varphi_m + R_m$. R_m is non-zero only over [1,*l*]. A more detailed description of these models and their expressions are presented by Nguyen in his thesis (1992) and in Nguyen et al. (1993). Equation (2.73) now becomes

$$Q_{mn}(\xi) = \rho_f \frac{U_0^2}{2\pi} \int_{-\infty}^{\infty} \frac{e^{-i\bar{\alpha}\xi}}{\bar{\alpha}} d\bar{\alpha} \left\{ \left[\left(\frac{\bar{\Omega}}{\varepsilon} - \bar{\alpha}\bar{U} \right)^2 \frac{I_n(\bar{\alpha}\varepsilon)}{I'_n(\bar{\alpha}\varepsilon)} - \left(\frac{\bar{\Omega}}{\varepsilon} \right)^2 \frac{K_n(\bar{\alpha}\varepsilon)}{K'_n(\bar{\alpha}\varepsilon)} \right] (\varphi_m^* + R_m^*)(\bar{\alpha}) \right\}. \tag{2.74}$$

Furthermore, we shall use the extended Galerkin method. The comparison functions will be the beam eigenfunctions and the domain of integration [0,1] with respect to the variable ξ. Thus, the nondimensionalized general force is given by

$$\overline{Q_{kmn}} = \frac{1}{Q_0}\int_0^1 Q_{mn}(\xi)\varphi_k(\xi)d\xi$$

$$= \frac{\rho_f a}{\rho_s h}\frac{\varepsilon}{2\pi}\int_{-\infty}^{\infty}\frac{1}{\bar{\alpha}}\left\{\left[\left(\frac{\bar{\Omega}}{\varepsilon}-\bar{\alpha}\bar{U}\right)^2\frac{I_n(\bar{\alpha}\varepsilon)}{I'_n(\bar{\alpha}\varepsilon)} - \left(\frac{\bar{\Omega}}{\varepsilon}\right)^2\frac{K_n(\bar{\alpha}\varepsilon)}{K'_n(\bar{\alpha}\varepsilon)}\right]\right\}H_{km}(\bar{\alpha})d\bar{\alpha}, \tag{2.75}$$

where $H_{km}(\bar{\alpha}) = \left(\int_0^1 \varphi_k(\xi)e^{-i\bar{\alpha}\xi}d\xi\right)\left(\int_0^1 \varphi_m(\xi)e^{i\bar{\alpha}\xi}d\xi + \int_1^l R_m(\xi)e^{i\bar{\alpha}\xi}d\xi\right)$.

The following notations will be used:

$$\mu_e = \frac{\rho_f a}{\rho_s h}, \quad E_n(\bar{\alpha}) = \frac{I_n(\bar{\alpha}\varepsilon)}{I'_n(\bar{\alpha}\varepsilon)}, \quad F_n(\bar{\alpha}) = \frac{K_n(\bar{\alpha}\varepsilon)}{K'_n(\bar{\alpha}\varepsilon)}. \tag{2.76}$$

Regrouping the terms depending of the square of the velocity, of the velocity and of the frequency and of the square of the frequency in (2.75), we can write

$$\overline{Q_{kmn}} = q_{kmn}^{(1)}\bar{\Omega}^2 + 2q_{kmn}^{(2)}\bar{U}\bar{\Omega} + q_{kmn}^{(3)}\bar{U}^2, \tag{2.77}$$

where

$$q_{kmn}^{(1)} = \frac{\mu_e}{2\pi\varepsilon}\int_{-\infty}^{\infty}\frac{E_n(\bar{\alpha}) - F_n(\bar{\alpha})}{\bar{\alpha}}H_{km}(\bar{\alpha})d\bar{\alpha}, \tag{2.78}$$

$$q_{kmn}^{(2)} = -\frac{\mu_e}{2\pi}\int_{-\infty}^{\infty}E_n(\bar{\alpha})H_{km}(\bar{\alpha})d\bar{\alpha}, \tag{2.79}$$

$$q_{kmn}^{(3)} = \frac{\mu_e\varepsilon}{2\pi}\int_{-\infty}^{\infty}\bar{\alpha}E_n(\bar{\alpha})H_{km}(\bar{\alpha})d\bar{\alpha}. \tag{2.80}$$

2.3.3 Solution to the Equations of Motion

The expression of the perturbation pressure has now been fully determined. We can now look for solutions for the problem of the cantilevered shell aspirating fluid governed by the equation (2.14) to (2.16) and subjected to the boundary conditions (2.34) to (2.37) by introducing (2.77) into those equations. As explained before, the extended form of the Galerkin method is used. In this part, we consider the following nondimensionalized form of the perturbation displacements and of the corresponding variations

$$\begin{Bmatrix} u \\ v \\ w \end{Bmatrix} = L \sum_{n=1}^{\infty} \sum_{m=1}^{\infty} \begin{Bmatrix} \overline{A_m} \cos n\theta \left(\varepsilon \dfrac{\partial}{\partial \xi} \right) \\ \overline{B_m} \sin n\theta \\ \overline{C_m} \cos n\theta \end{Bmatrix} \varphi_m(\xi) e^{i\Omega t}, \tag{2.81}$$

$$\begin{Bmatrix} \delta u \\ \delta v \\ \delta w \end{Bmatrix} = L \sum_{l=1}^{\infty} \sum_{k=1}^{\infty} \begin{Bmatrix} \delta\overline{A_k} \cos l\theta \left(\varepsilon \dfrac{\partial}{\partial \xi} \right) \\ \delta\overline{B_k} \sin l\theta \\ \delta\overline{C_k} \cos l\theta \end{Bmatrix} \varphi_k(\xi) e^{i\Omega t}, \tag{2.82}$$

where *m* and *n* are respectively the axial and circumferential mode of the displacement and *k* and *l* are respectively the axial and circumferential mode of the corresponding variations.

The extended form of the Galerkin method is then given by

$$\begin{aligned} \delta E = \int_0^{2\pi} \Bigg\{ \frac{D}{\varepsilon} \int_0^1 & [L_1 \delta u + L_2 \delta v - L_3 \delta w] d\xi \\ & - D \left[R_1 \delta u + \frac{1-\nu}{2} R_2 \delta v \right. \\ & \left. + k_a (R_3 \varepsilon \delta w' + R_4 \delta w) \right]_{\xi=1} \Bigg\} d\theta = 0, \end{aligned} \tag{2.83}$$

where the derivative is now defined by $(\quad)' = \partial(\quad)/\partial\xi$.

Substituting (2.81) and (2.82) into the expressions of the boundary conditions, we obtain

$$R_1\delta u|_{\xi=1} = L^2 e^{2i\Omega t}\sum_{n=1}^{\infty}\sum_{l=1}^{\infty}\cos n\theta\cos l\theta\, f_{R1}(n), \tag{2.84}$$

$$R_2\delta v|_{\xi=1} = L^2 e^{2i\Omega t}\sum_{n=1}^{\infty}\sum_{l=1}^{\infty}\sin n\theta\sin l\theta\, f_{R2}(n), \tag{2.85}$$

$$R_3\varepsilon\delta w'|_{\xi=1} = L^2 e^{2i\Omega t}\sum_{n=1}^{\infty}\sum_{l=1}^{\infty}\cos n\theta\cos l\theta\, f_{R3}(n), \tag{2.86}$$

$$R_4\delta w|_{\xi=1} = L^2 e^{2i\Omega t}\sum_{n=1}^{\infty}\sum_{l=1}^{\infty}\cos n\theta\cos l\theta\, f_{R4}(n), \tag{2.87}$$

where

$$\begin{aligned} f_{R1}(n) = \sum_{m=1}^{\infty}\sum_{k=1}^{\infty}\delta\overline{A_k}\big[&\overline{B_m}\big(\nu n\varepsilon\varphi_m(1)\varphi'_k(1)\big) \\ &+ \overline{C_m}\big(\nu\varepsilon\varphi_m(1)\varphi'_k(1)\big)\big], \end{aligned} \tag{2.88}$$

$$\begin{aligned} f_{R2}(n) = \sum_{m=1}^{\infty}\sum_{k=1}^{\infty}\delta\overline{B_k}\big[&\overline{A_m}\big(-n\varepsilon\varphi'_m(1)\varphi_k(1)\big) \\ &+ \overline{B_m}\big(\varepsilon(1+3k)\varphi'_m(1)\varphi_k(1)\big) \\ &+ \overline{C_m}\big(3nk_a\varepsilon\varphi'_m(1)\varphi_k(1)\big)\big], \end{aligned} \tag{2.89}$$

$$\begin{aligned} f_{R3}(n) = \sum_{m=1}^{\infty}\sum_{k=1}^{\infty}\delta\overline{C_k}\big[&\overline{B_m}\big(-\nu n\varepsilon\varphi_m(1)\varphi'_k(1)\big) \\ &+ \overline{C_m}\big(-\nu n^2\varepsilon\varphi_m(1)\varphi'_k(1)\big)\big], \end{aligned} \tag{2.90}$$

$$\begin{aligned} f_{R4}(n) = \sum_{m=1}^{\infty}\sum_{k=1}^{\infty}\delta\overline{C_k}\Bigg[&\overline{A_m}\left(\frac{1-\nu}{2}n^2\varepsilon\varphi'_m(1)\varphi_k(1)\right) \\ &+ \overline{B_m}\left(\frac{3-\nu}{2}\varepsilon n\varphi'_m(1)\varphi_k(1)\right) \\ &+ \overline{C_m}\Bigg((2-\nu)n^2\varepsilon\varphi'_m(1)\varphi_k(1) \\ &+ \frac{\mu_e\varepsilon}{2k_a}\overline{U}\left[i\frac{\overline{\Omega}}{\varepsilon}\varphi_m(1) + \overline{U}\alpha\varphi'_m(1)\right]\varphi_k(1)\Bigg)\Bigg]. \end{aligned} \tag{2.91}$$

We obatin something similar for the equations of motion:

$$L_1\delta u = L^2 e^{2i\Omega t}\sum_{n=1}^{\infty}\sum_{l=1}^{\infty}\cos n\theta\cos l\theta\, f_{L1}(n,\xi), \tag{2.92}$$

$$L_2\delta v = L^2 e^{2i\Omega t}\sum_{n=1}^{\infty}\sum_{l=1}^{\infty}\sin n\theta\sin l\theta\, f_{L2}(n,\xi), \tag{2.93}$$

$$L_3\delta w = L^2 e^{2i\Omega t}\sum_{n=1}^{\infty}\sum_{l=1}^{\infty}\cos n\theta\cos l\theta\, f_{L3}(n,\xi), \tag{2.94}$$

with

$$\begin{aligned} f_{L1}(n,\xi) = \sum_{m=1}^{\infty}\sum_{k=1}^{\infty}\delta\overline{A_k}\Bigg[&\overline{A_m}\Bigg(\varepsilon^2{\varphi'}_m(\xi){\varphi'}_k(\xi)\Bigg[\overline{\Omega}^2 \\ &-\frac{1-\nu}{2}n^2(1+k_a)-\tau_\theta(\xi)n^2\Bigg] \\ &+\varepsilon^4{\varphi'''}_m(\xi){\varphi'}_k(\xi)[1+\tau_x(\xi)]\Bigg) \\ &+\overline{B_m}\Bigg(\frac{1+\nu}{2}n\varepsilon^2{\varphi'}_m(\xi){\varphi'}_k(\xi) \\ &+\tau(\xi)n\varepsilon\varphi_m(\xi){\varphi'}_k(\xi)\Bigg) \\ &+\overline{C_m}\Bigg(\varepsilon^2{\varphi'}_m(\xi){\varphi'}_k(\xi)\Bigg[\nu-k_a\frac{1-\nu}{2}n^2-\tau_\theta(\xi)\Bigg] \\ &-k_a\varepsilon^4{\varphi'''}_m(\xi){\varphi'}_k(\xi)+\tau(\xi)\varepsilon\varphi_m(\xi){\varphi'}_k(\xi)\Bigg)\Bigg], \end{aligned} \tag{2.95}$$

$$\begin{aligned} f_{L2}(n,\xi) = \sum_{m=1}^{\infty}\sum_{k=1}^{\infty}\delta\overline{B_k}\Bigg[&\overline{A_m}\Bigg(-\frac{1+\nu}{2}n\varepsilon^2{\varphi''}_m(\xi)\varphi_k(\xi)\Bigg) \\ &+\overline{B_m}\Bigg(\varphi_m(\xi)\varphi_k(\xi)[\overline{\Omega}^2-\mathrm{n}^2(1+\tau_\theta(\xi))] \\ &+\varepsilon^2{\varphi''}_m(\xi)\varphi_k(\xi)\Bigg[\frac{1-\nu}{2}(1+3k_a)+\tau_x(\xi)\Bigg]\Bigg) \\ &+\overline{C_m}\Bigg(\varphi_m(\xi)\varphi_k(\xi)[-n(1+\tau_\theta(\xi))] \\ &+\varepsilon^2{\varphi''}_m(\xi)\varphi_k(\xi)k_a\frac{3-\nu}{2}n\Bigg)\Bigg], \end{aligned} \tag{2.96}$$

$$\begin{aligned} f_{L3}(n,\xi) = \sum_{m=1}^{\infty}\sum_{k=1}^{\infty}\delta\overline{C_k}\Bigg[\overline{A_m}\Big(&\varphi_m(\xi)\varphi_k(\xi)[-k_a\lambda_m^4\varepsilon^4] \\ &+\varepsilon^2\varphi''_m(\xi)\varphi_k(\xi)\left[\nu-k_a\frac{1-\nu}{2}n^2-\tau_\theta(\xi)\right]\Big) \\ &+\overline{B_m}\Big(\varphi_m(\xi)\varphi_k(\xi)n[1+\tau_\theta(\xi)] \\ &-\varepsilon^2\varphi''_m(\xi)\varphi_k(\xi)\frac{3-\nu}{2}k_a n\Big) \\ &+\overline{C_m}\Bigg(\varphi_m(\xi)\varphi_k(\xi)[1+k_a\lambda_m^4\varepsilon^4+k_a(n^2-1)^2 \\ &+\tau_\theta(\xi)n^2-\overline{\Omega}^2\,]-\varepsilon^2\varphi''_m(\xi)\varphi_k(\xi)[2n^2k_a+\tau_x(\xi)] \\ &-\frac{Q_{mn}(\xi)}{Q_0}\varphi_k(\xi)\Bigg)\Bigg]. \end{aligned} \tag{2.97}$$

In the above, we took into account that $\varphi''_m(1)=\varphi'''_m(1)=0$ and $\varphi''''_m(\xi)=\lambda_m^4\varphi_m(\xi)$. We can now re-write the expression of the variation of the energy:

$$\begin{aligned} \delta E = L^2 e^{2i\Omega t}\int_0^{2\pi}\Bigg\{\frac{D}{\varepsilon}\int_0^1\Bigg[\sum_{n=1}^{\infty}\sum_{l=1}^{\infty}\big(&\cos n\theta\cos l\theta\, f_{L1}(n,\xi) \\ &+\sin n\theta\sin l\theta\, f_{L2}(n,\xi) \\ &-\cos n\theta\cos l\theta\, f_{L3}(n,\xi)\big)\Bigg]d\xi \\ &-D\sum_{n=1}^{\infty}\sum_{l=1}^{\infty}\Big(\cos n\theta\cos l\theta\,[f_{R1}(n,\xi)+k_a f_{R3}(n,\xi) \\ &+k_a f_{R4}(n,\xi)]+\frac{1-\nu}{2}\sin n\theta\sin l\theta\, f_{R2}(n,\xi)\Big)\Bigg\}d\theta. \end{aligned} \tag{2.98}$$

We can invert the order of the integral and we also know that

$$\int_0^{2\pi}\cos n\theta\cos l\theta\,d\theta=\int_0^{2\pi}\sin n\theta\sin l\theta\,d\theta=\begin{cases}0\ if\ n\neq l\\ \pi\ if\ n=l\end{cases} \tag{2.99}$$

Thus, only the terms corresponding to *n=l* are not equal to zero, and

$$\begin{aligned}\delta E = L^2 e^{2i\Omega t} D\pi \sum_{n=1}^{\infty} \Bigg\{ \frac{1}{\varepsilon} \int_0^1 [f_{L1}(n,\xi) + f_{L2}(n,\xi) - f_{L3}(n,\xi)] d\xi \\ - \Big[f_{R1}(n,\xi) + k_a f_{R3}(n,\xi) + k_a f_{R4}(n,\xi) \\ + \frac{1-\nu}{2} f_{R2}(n,\xi) \Big] \Bigg\}.\end{aligned} \tag{2.100}$$

To simplify the writing, we define some new notations:

$$\begin{aligned} a_{km} &= \int_0^1 \varphi'_k(\xi)\varphi_m(\xi)d\xi\,, & b_{km} &= \int_0^1 \varphi'_k(\xi)\varphi'_m(\xi)d\xi\,, \\ c_{km} &= \int_0^1 \varphi_k(\xi)\varphi''_m(\xi)d\xi\,, & d_{km} &= \int_0^1 \varphi'_k(\xi)\varphi'''_m(\xi)d\xi\,, \\ g_{km} &= \int_0^1 \xi\varphi_k(\xi)\varphi_m(\xi)d\xi\,, & h_{km} &= \int_0^1 \xi\varphi'_k(\xi)\varphi'_m(\xi)d\xi\,, \\ k_{km} &= \int_0^1 \xi\varphi_k(\xi)\varphi''_m(\xi)d\xi, & l_{km} &= \int_0^1 \xi\varphi'_k(\xi)\varphi'''_m(\xi)d\xi\,, \\ e_{km} &= \varphi'_k(1)\varphi_m(1) = 4\lambda_k\sigma_k(-1)^{k+m}, & f_{km} &= e_{mk}, \end{aligned} \tag{2.101}$$

where $\sigma_k = \frac{\sinh\lambda_k - \sin\lambda_k}{\cosh\lambda_k + \cos\lambda_k}$. The values of the eigenfunctions at both ends of the shell and of the previous expressions are given in Nguyen (1992). We also nondimensionalized the expression of the basic stresses and loads:

$$\tau_x = \hat{A}_1\xi + \hat{B}_1, \qquad \tau = \hat{B}_2, \qquad \tau_\theta = \hat{A}_3\xi + \hat{B}_3, \tag{2.102}$$

where

$$\begin{aligned} \hat{A}_1 &= -\mu_e \bar{U}^2 \frac{\lambda_f}{8\varepsilon}, \qquad \hat{B}_2 = \mu_e \bar{U}^2 \frac{\lambda_f}{8}, \qquad \hat{A}_3 = -\mu_e \bar{U}^2 \frac{\lambda_f}{4\varepsilon}, \\ \hat{B}_1 &= \mu_e \bar{U}^2 \left(\frac{\lambda_f}{8\varepsilon} + \frac{1}{2}(1-\alpha)(1+\bar{\gamma}) \right), \quad \hat{B}_3 = \mu_e \bar{U}^2 \left(\frac{\lambda_f}{4\varepsilon} - (1-\alpha) \right). \end{aligned} \tag{2.103}$$

Thus, we can write:

$$\begin{aligned}\int_0^1 f_{L1}(n,\xi)d\xi = \sum_{m=1}^{\infty}\sum_{k=1}^{\infty}\delta\overline{A_k}\Big[\overline{A_m}\Big(&\varepsilon^2 b_{km}\Big[\overline{\Omega}^2-\frac{1-\nu}{2}n^2(1+k_a)\\&-\hat{B}_3 n^2\Big]-n^2\varepsilon^2\hat{A}_3 h_{km}+\varepsilon^4\big[1+\hat{B}_1\big]d_{km}\\&+\varepsilon^4\hat{A}_1 l_{km}\Big)+\overline{B_m}\Big(\frac{1+\nu}{2}n\varepsilon^2 b_{km}+\hat{B}_2 n\varepsilon a_{km}\Big)\\&+\overline{C_m}\Big(\varepsilon^2 b_{km}\Big[\nu-k_a\frac{1-\nu}{2}n^2-\hat{B}_3\Big]-\varepsilon^2 h_{km}\hat{A}_3\\&-k_a\varepsilon^4 d_{km}+\hat{B}_2\varepsilon a_{km}\Big)\Big],\end{aligned}\tag{2.104}$$

$$\begin{aligned}\int_0^1 f_{L2}(n,\xi)d\xi = \sum_{m=1}^{\infty}\sum_{k=1}^{\infty}\delta\overline{B_k}\Big[\overline{A_m}\Big(&-\frac{1+\nu}{2}n\varepsilon^2 c_{km}\Big)\\&+\overline{B_m}\Big(\delta_{km}\big[\overline{\Omega}^2-\mathrm{n}^2\big(1+\hat{B}_3\big)\big]-n^2\hat{A}_3 g_{km}\\&+\varepsilon^2 c_{km}\Big[\frac{1-\nu}{2}(1+3k_a)+\hat{B}_1\Big]+\varepsilon^2 k_{km}\hat{A}_1\Big)\\&+\overline{C_m}\Big(\delta_{km}\big[-n\big(1+\hat{B}_3\big)\big]-n\hat{A}_3 g_{km}\\&+\varepsilon^2 c_{km}k_a\frac{3-\nu}{2}n\Big)\Big],\end{aligned}\tag{2.105}$$

$$\begin{aligned}\int_0^1 f_{L3}(n,\xi)d\xi = \sum_{m=1}^{\infty}\sum_{k=1}^{\infty}\delta\overline{C_k}\Big[\overline{A_m}\Big(&\delta_{km}[-k_a\lambda_m^4\varepsilon^4]\\&+\varepsilon^2 c_{km}\Big[\nu-k_a\frac{1-\nu}{2}n^2-\hat{B}_3\Big]-\varepsilon^2 k_{km}\hat{A}_3\Big)\\&+\overline{B_m}\Big(\delta_{km}n\big[1+\hat{B}_3\big]+n\hat{A}_3 g_{km}-\varepsilon^2 c_{km}\frac{3-\nu}{2}k_a n\Big)\\&+\overline{C_m}\Big(\delta_{km}[1-\overline{\Omega}^2+k_a\lambda_m^4\varepsilon^4+k_a(n^2-1)^2\\&+\hat{B}_3 n^2]+n^2\hat{A}_3 g_{km}-\varepsilon^2 c_{km}\big[2n^2 k_a+\hat{B}_1\big]\\&-\varepsilon^2 k_{km}\hat{A}_1-\Big[q_{kmn}^{(1)}\overline{\Omega}^2+2q_{kmn}^{(2)}\overline{U}\overline{\Omega}+q_{kmn}^{(3)}\overline{\mathrm{U}}^2\Big]\Big)\Big].\end{aligned}\tag{2.106}$$

Finally, the expression of δE can simply be written as

$$L^2 e^{2i\Omega t}\frac{D}{\varepsilon}\pi\sum_{n=1}^{\infty}\sum_{k=1}^{\infty}[W_{1kn}\delta\overline{A_k}+W_{2kn}\delta\overline{B_k}+W_{3kn}\delta\overline{C_k}]=0,\tag{2.107}$$

where

$$
\begin{aligned}
W_{1kn} = \sum_{m=1}^{\infty} \Bigg[& \overline{A_m} \Big(\varepsilon^2 b_{km} \Big[\overline{\Omega}^2 - \frac{1-\nu}{2} n^2 (1+k_a) - \hat{B}_3 n^2 \Big] \\
& - n^2 \varepsilon^2 \hat{A}_3 h_{km} + \varepsilon^4 \big[1+\hat{B}_1\big] d_{km} + \varepsilon^4 \hat{A}_1 l_{km} \Big) \\
& + \overline{B_m} \bigg(\frac{1+\nu}{2} n \varepsilon^2 b_{km} + \hat{B}_2 n \varepsilon a_{km} \\
& - \nu n \varepsilon^2 \varphi_m(1) \varphi'_k(1) \bigg) \\
& + \overline{C_m} \bigg(\varepsilon^2 b_{km} \Big[\nu - k_a \frac{1-\nu}{2} n^2 - \hat{B}_3 \Big] - \varepsilon^2 h_{km} \hat{A}_3 \\
& - k_a \varepsilon^4 d_{km} + \hat{B}_2 \varepsilon a_{km} - \nu \varepsilon^2 \varphi_m(1) \varphi'_k(1) \bigg) \Bigg],
\end{aligned}
\tag{2.108}
$$

$$
\begin{aligned}
W_{2kn} = \sum_{m=1}^{\infty} \Bigg[& \overline{A_m} \Big(-\frac{1+\nu}{2} n \varepsilon^2 c_{km} + \frac{1-\nu}{2} n \varepsilon^2 \varphi'_m(1) \varphi_k(1) \Big) \\
& + \overline{B_m} \bigg(\delta_{km} \big[\overline{\Omega}^2 - \mathrm{n}^2 \big(1+\hat{B}_3\big) \big] - n^2 \hat{A}_3 g_{km} \\
& + \varepsilon^2 c_{km} \Big[\frac{1-\nu}{2} (1+3k_a) + \hat{B}_1 \Big] + \varepsilon^2 k_{km} \hat{A}_1 \\
& - \frac{1-\nu}{2} \varepsilon^2 (1+3k_a) \varphi'_m(1) \varphi_k(1) \bigg) \\
& + \overline{C_m} \bigg(\delta_{km} \big[-n \big(1+\hat{B}_3\big) \big] - n \hat{A}_3 g_{km} \\
& + \varepsilon^2 c_{km} k_a \frac{3-\nu}{2} n - \frac{1-\nu}{2} 3 n k_a \varepsilon^2 \varphi'_m(1) \varphi_k(1) \bigg) \Bigg],
\end{aligned}
\tag{2.109}
$$

$$
\begin{aligned}
W_{3kn} = \sum_{m=1}^{\infty} \Bigg[& \overline{A_m}\Bigg(\delta_{km} k_a \lambda_m^4 \varepsilon^4 - \varepsilon^2 c_{km}\left[\nu - k_a \frac{1-\nu}{2} n^2 - \hat{B}_3\right] \\
& + \varepsilon^2 k_{km} \hat{A}_3 - \frac{1-\nu}{2} n^2 \varepsilon^2 \varphi'_m(1)\varphi_k(1)\Bigg) \\
& + \overline{B_m}\Bigg(-\delta_{km} n\big[1+\hat{B}_3\big] - n\hat{A}_3 g_{km} \\
& + \varepsilon^2 c_{km}\frac{3-\nu}{2} k_a n + k_a \nu n \varepsilon^2 \varphi_m(1)\varphi'_k(1) \\
& - \frac{3-\nu}{2}\varepsilon^2 k_a n \varphi'_m(1)\varphi_k(1)\Bigg) \\
& + \overline{C_m}\Bigg(\bar{\Omega}^2 \left(\delta_{km} + q_{kmn}^{(1)}\right) \\
& + \bar{\Omega}\bar{U}\left(2q_{kmn}^{(2)} - i\frac{\mu_e \varepsilon}{2}\varphi_m(1)\varphi_k(1)\right) \\
& - \delta_{km}\big[1 + k_a \lambda_m^4 \varepsilon^4 + k_a (n^2-1)^2 + \hat{B}_3 n^2\big] \\
& - n^2 \hat{A}_3 g_{km} + \varepsilon^2 c_{km}\big[2n^2 k_a + \hat{B}_1\big] + \varepsilon^2 k_{km}\hat{A}_1 \\
& + \bar{U}^2\left(q_{kmn}^{(3)} - \frac{\mu_e \varepsilon^2}{2}\alpha\varphi'_m(1)\varphi_k(1)\right) \\
& + \nu n^2 \varepsilon^2 k_a \varphi_m(1)\varphi'_k(1) \\
& - (2-\nu) n^2 \varepsilon^2 k_a \varphi'_m(1)\varphi_k(1)\Bigg)\Bigg].
\end{aligned}
\tag{2.110}
$$

The small displacements we chose are totally arbitrary. As the series is equal to zero, each coefficient of these small displacements has to vanish. This implies that

$$
\forall k: \quad \begin{cases} \sum_{n=1}^{\infty} W_{1kn} = 0 \\ \sum_{n=1}^{\infty} W_{2kn} = 0 \\ \sum_{n=1}^{\infty} W_{3kn} = 0 \end{cases}
\tag{2.111}
$$

Furthermore, in the previous three series, each term depends on *n*, so that each term is independent from the others. The series being null, this means that:

$$\forall k, \forall n: \quad \begin{cases} W_{1kn} = 0 \\ W_{2kn} = 0 \\ W_{3kn} = 0. \end{cases} \tag{2.112}$$

Each of these terms takes the following general form:

$$W_{ikn} = \sum_{m=1}^{\infty} J_{kmn}^{i,1} \overline{A_m} + J_{kmn}^{i,2} \overline{B_m} + J_{kmn}^{i,3} \overline{C_m}, \quad i = 1, 2, 3. \tag{2.113}$$

The terms of equation (2.113) are given in Appendix C. To get solutions, we need to solve these sets of equations. Because the numerical method does not allow us to find solutions when these series are infinite, we need to choose a finite number of comparison functions to be used to solve the problem. We define *M* as this number. The summations on the axial wave number *m* will be limited to $1 \leq m \leq M$, so that the summation on the admissible function number, $1 \leq k \leq M$. That implies that the resolution of the problem (2.112) is equivalent to the resolution of a 3*M* equation system, the 3*M* unknowns being $\overline{A_m}$, $\overline{B_m}$ and $\overline{C_m}$ where $1 \leq m \leq M$. In the terms of these equations, there is still one unknown: the frequency $\overline{\Omega}$. The resolution of equation (2.112) is finally equivalent to the resolution of the following matrix equation:

$$([M]\overline{\Omega}^2 + [\mathrm{C}]\overline{\Omega} + [\mathrm{K}])\{X\} = \{0\}, \tag{2.114}$$

where $\{X\} = \{\overline{A_1} \cdots \overline{A_M}\, \overline{B_1} \cdots \overline{B_M}\, \overline{C_1} \cdots \overline{C_M}\}^{\mathrm{T}}$.

We chose this way of ordering the unknowns, so that the different matrices take a simple form, as follows:

$$[M] = \begin{bmatrix} M_{km}^{1,1} & 0 & 0 \\ 0 & M_{km}^{2,2} & 0 \\ 0 & 0 & M_{km}^{3,3} \end{bmatrix}, \tag{2.115}$$

$$[C] = \begin{bmatrix} 0 & 0 & 0 \\ 0 & 0 & 0 \\ 0 & 0 & C_{km}^{3,3} \end{bmatrix}, \tag{2.116}$$

$$[K] = \begin{bmatrix} K_{km}^{1,1} & K_{km}^{1,2} & K_{km}^{1,3} \\ K_{km}^{2,1} & K_{km}^{2,2} & K_{km}^{2,3} \\ K_{km}^{3,1} & K_{km}^{3,2} & K_{km}^{3,3} \end{bmatrix}. \tag{2.117}$$

Each element of those matrices is actually a *MxM* submatrix. They are given in Appendix C.

So far, we have taken into account the curvature of the shell, the steady viscous effects, new boundary conditions but not the internal dissipation of energy. We shall employ a two-parameter damping model, suitable for the elastomer material of the shells used in the experiments; thus, in effect, we consider two kinds of damping (see Païdoussis and Des Trois Maisons, 1971). The first one is called "structural damping", characterized by the structural damping coefficient μ. The second one is the "viscoelastic damping" and is characterized by the viscoelastic damping coefficient χ. Thus, in the model, Young's modulus *E* has to be replaced by $E\left[1+\left(\frac{\mu}{\Omega}+\chi\right)\frac{\partial}{\partial t}\right]$ where Ω is the radian frequency of the motion. Thus, equation (2.114) takes the form

$$([M']\bar{\Omega}^2 + [\mathrm{C}']\bar{\Omega} + [\mathrm{K}'])\{X\} = \{0\}, \tag{2.118}$$

where $\begin{cases} [M'] = [M], \\ [C'] = [C] + i\chi\Omega_0[K], \\ [K'] = (1+\mu i)[K]. \end{cases}$

To solve this system, we use the standard method, effectively reducing the second-order system to a first-order one, by introducing a new variable

$$\{Y\} = \begin{Bmatrix} \{\mathrm{X}\} \\ \bar{\Omega}\{\mathrm{X}\} \end{Bmatrix}. \tag{2.119}$$

Thus, the former equation takes the form

$$([\mathrm{P}] + \bar{\Omega}[\mathrm{Q}])\{Y\} = \{0\}, \tag{2.120}$$

where $$\begin{cases} [\mathrm{P}] = \begin{bmatrix} [0] & [\mathrm{I_M}] \\ [\mathrm{K}] & [\mathrm{C}] \end{bmatrix}, \\ [\mathrm{Q}] = \begin{bmatrix} [-\mathrm{I_M}] & [0] \\ [0] & [\mathrm{M}] \end{bmatrix}. \end{cases}$$

Here $[\mathrm{I_M}]$ is the *MxM* identity matrix. The problem has now been reduced to an ordinary eigenvalue problem. Its numerical solution will give us the eigenfrenquencies $\overline{\Omega}$ and eigenvectors $\{X\} = \{\overline{A_1} \cdots \overline{A_M}\, \overline{B_1} \cdots \overline{B_M}\, \overline{C_1} \cdots \overline{C_M}\}^{\mathrm{T}}$ of the problem. Matlab® will provide us efficient tools for solving this problem numerically.

2.4 Theoretical Results

2.4.1 Preliminary Calculations

Before applying the theory developed in the previous parts to the case of a cylindrical cantilevered shell aspirating shell, preliminary calculations were conducted considering the case of a discharging cantilevered shell for two main reasons: to validate the Matlab® program developed to get theoretical results and to determine a number of parameters involved in the program. Comparisons between existing results and the results obtained with this theory were carried out to validate the use of the extended Galerkin method to solve the equations of motion, of the Gaussian quadrature to calculate the unsteady fluid forces and of an out-flow model to describe the downstream flow behaviour. All these

Table 2.1: The parameters of the computer program

Number of Gaussian points	2
Integration stepsize	$\Delta = 2$
Domain of integration	[-300; 300]
Number of admissible functions	*M*=10
Chosen model	Model 3
Length *l*	$2 \le l \le 3$

calculations were conducted without considering steady viscous effects. The way to determine these parameters is presented more precisely in Appendix D. The results themselves are shown in Table 2.1.

2.4.2 Predicted Dynamics for an Aspirating Shell

All the parameters of the Matlab® program having been determined, it will now be used to study the theoretical dynamics of the cantilevered aspirating shell. In the experiments that will be presented in the next section, two different pipes were used. The first one is the pipe used in the Rinaldi (2009) experiments. The second one is a much thinner pipe. Both are made of the same elastomer material whose properties are:

$$\begin{gathered} \nu = 0.5, \qquad \mu = 0.041, \qquad \chi = 0.00028\mathrm{s}, \\ E = 2.6 * 10^6\ \mathrm{N/m^2}, \qquad \rho_s = 1108\ \mathrm{kg/m^3} \end{gathered} \tag{2.121}$$

The geometric properties of the two pipes are presented in Table 2.2. The fluid used in the experiments is air. In this theory, we consider the flow to be incompressible. So, we consider the fluid density to be the air density in the atmospheric conditions:

$$\rho_f = 1.17\ \mathrm{kg/m^3}. \tag{2.122}$$

The Argand diagrams as well as the graph of the imaginary part of the non-dimensional frequency versus the non-dimensional flow velocity and the real part of the non-dimensional frequency versus the non-dimensional flow velocity obtained with the present theory for Pipe A and Pipe B are presented in Figure 2.4 to Figure 2.11.

For comparison with the experimental results, the following dimensionless parameters were used:

$$U_0 = \left[\frac{E}{\rho_s(1-\nu^2)}\right]^{1/2}, \qquad \Omega_0 = \left[\frac{E}{\rho_s a^2(1-\nu^2)}\right]^{1/2}. \tag{2.123}$$

Table 2.2: The geometrical and physical properties of the pipes

Properties	Pipe A	Pipe B
a in meters (in)	$4.67*10^{-3}$ (0.184)	$6.35*10^{-3}$ (0.250)
h in meters (in)	$3.28*10^{-3}$ (0.129)	$7.87*10^{-4}$ (0.031)
L in meters (in)	0.445 (17.51)	0.182 (7.15)

From the figures, it is seen that, in both cases, the theory predicts that the effect of flow for small values of the non-dimensional flow velocities is to damp the system in all modes as the imaginary part of the non-dimensional frequency is positive. As the dimensionless flow velocity increases, all the modes become less damped and the imaginary part of the non-dimensional frequency eventually becomes negative while its real part is still positive. This corresponds to an instability threshold by flutter. Moreover, the real part of the non-dimensional frequency can be equal to zero at higher flow velocity while its imaginary part is still negative; this corresponds to a static instability.

More precisely, for Pipe A, the theory predicts a loss by flutter in the 2nd circumferential mode and the 1st axial mode at:

$$\begin{cases} u_{cr} = 0.092 \\ U_{cr} = 5.1\text{m/s.} \end{cases} \tag{2.124}$$

It is then followed by flutter in the 3rd circumferential mode and the 1st axial mode at:

$$\begin{cases} u_{cr} = 0.165 \\ U_{cr} = 9.15\text{ m/s.} \end{cases} \tag{2.125}$$

Finally, the pipe buckles in the 2nd circumferential mode and the 1st axial mode at

$$\begin{cases} u_{cr} = 0.228 \\ U_{cr} = 12.7\text{ m/s.} \end{cases} \tag{2.126}$$

For Pipe B, the theory predicts a loss by flutter in the 1st circumferential mode and the 1st axial mode at:

$$\begin{cases} u_{cr} = 0.169 \\ U_{cr} = 9.4\text{ m/s.} \end{cases} \tag{2.127}$$

It is then followed by flutter in the 2nd circumferential mode and the 1st axial mode at:

$$\begin{cases} u_{cr} = 0.270 \\ U_{cr} = 15 \text{ m/s.} \end{cases} \tag{2.128}$$

Finally, the pipe buckles in the same mode at:

$$\begin{cases} u_{cr} = 0.318 \\ U_{cr} = 17.5 \text{ m/s.} \end{cases} \tag{2.129}$$

Thus, for both cases, the theory predicts a loss of stability by flutter followed at higher flow velocity by buckling. Flutter occurs not in the same mode for both pipes; the buckling, however, arises in the same mode for Pipe A and Pipe B. For both instabilities, the predicted critical flow velocities are higher for Pipe B than for Pipe A.

2.5 Experimental Observations

As I mentioned it before, the initial motivation of this study was the observation of a shell-type instability in the experiments that were conducted by Rinaldi (2009) and that involved an aspirating cantilevered pipe. That is why the experimental apparatus that was utilized in this project is the same as the one she used.

The experimental apparatus, presented in Figure 2.12, consists of a large steel tank, an internal plexiglas flow-guiding protective conduit, a flexible elastomer pipe, a compressed air reservoir and a flow meter device. The tank possesses a plexiglas window for viewing purposes. The pipe is located inside the plexiglas flow-guiding protective conduit (Figure 2.13) whose function is to ensure that the air entering the tank does not disturb the pipe during the experiments. A screen, a honeycomb and an additional screen are located at the bottom of the conduit for flow-straightening purposes.

As mentioned in the previous section, two different pipes were tested in the experiments. Their geometrical and physical properties are recalled in (2.121)

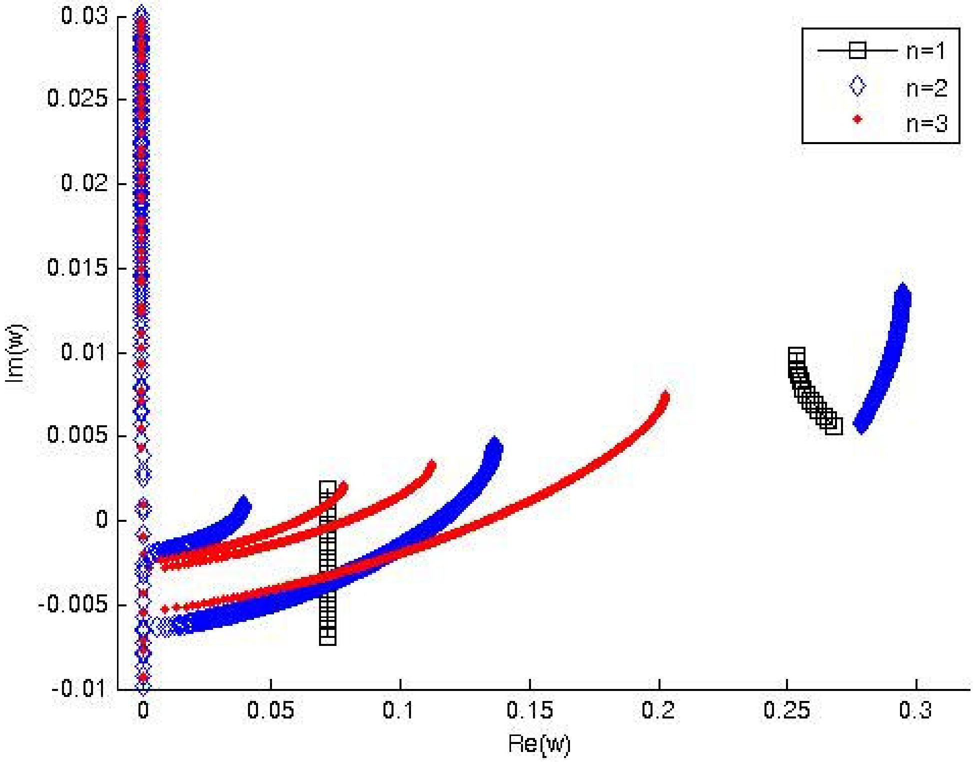

Figure 2.4: Argand diagram obtained with the present theory for Pipe A

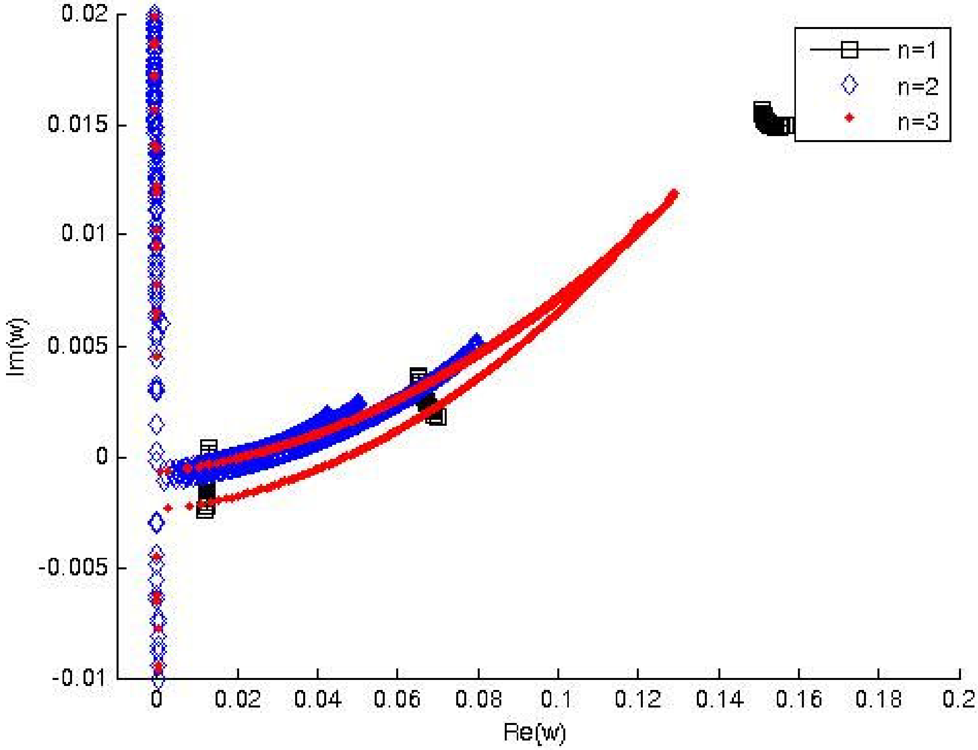

Figure 2.5: Argand diagram obtained with the present theory for Pipe B

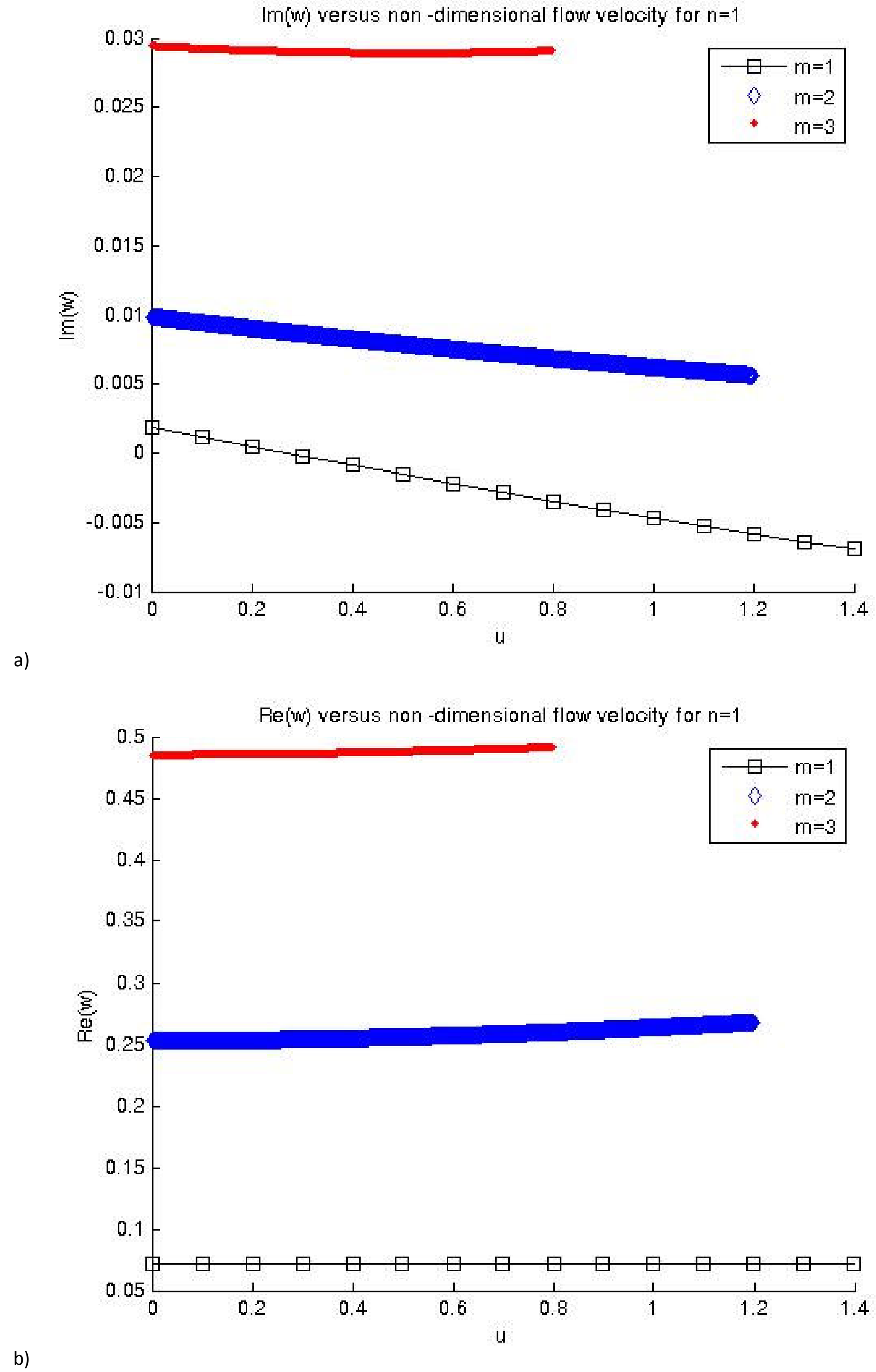

Figure 2.6: a) Im(ω) and b) Re(ω) as a function of u for the 1st circumferential mode of Pipe A

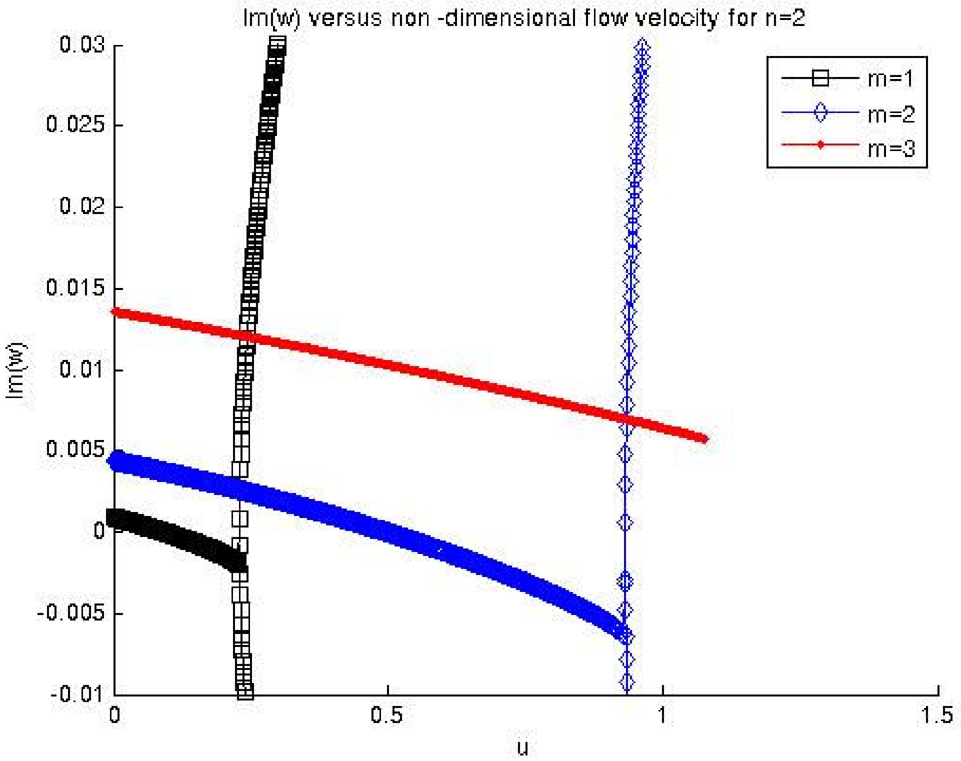

a)

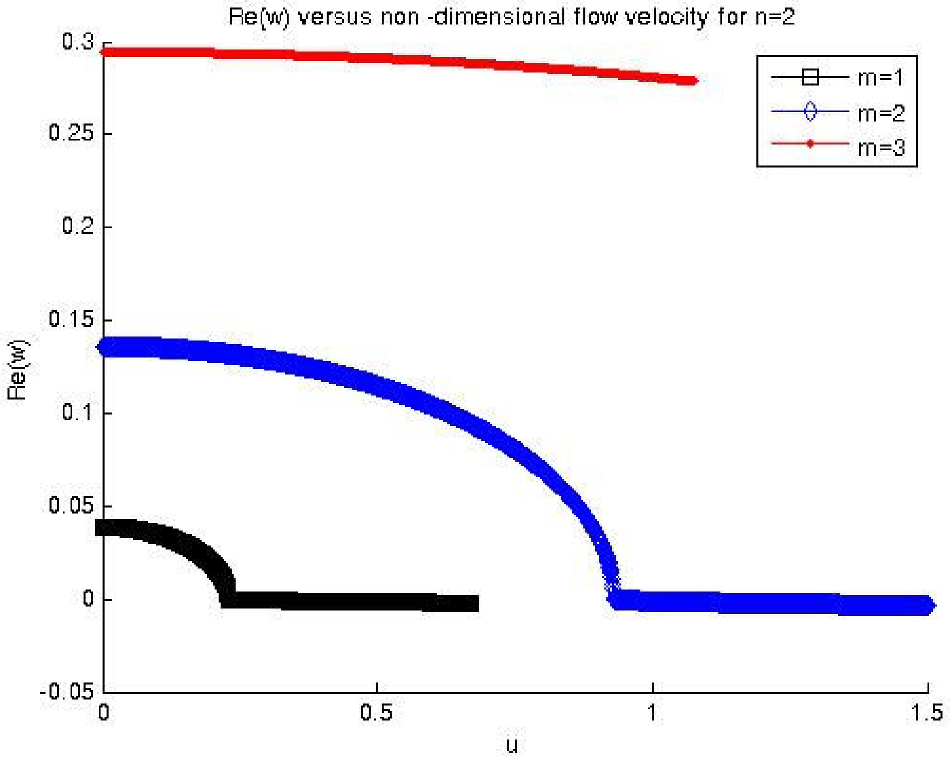

b)

Figure 2.7: a) Im(ω) and b) Re(ω) as a function of u for the 2nd circumferential mode of Pipe A

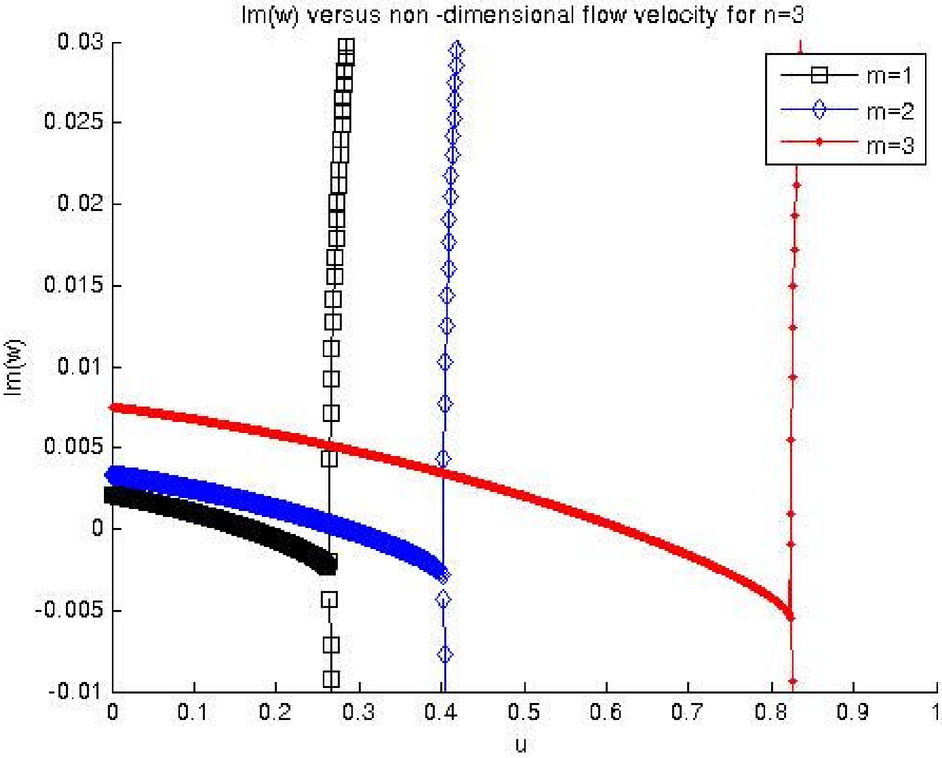

a)

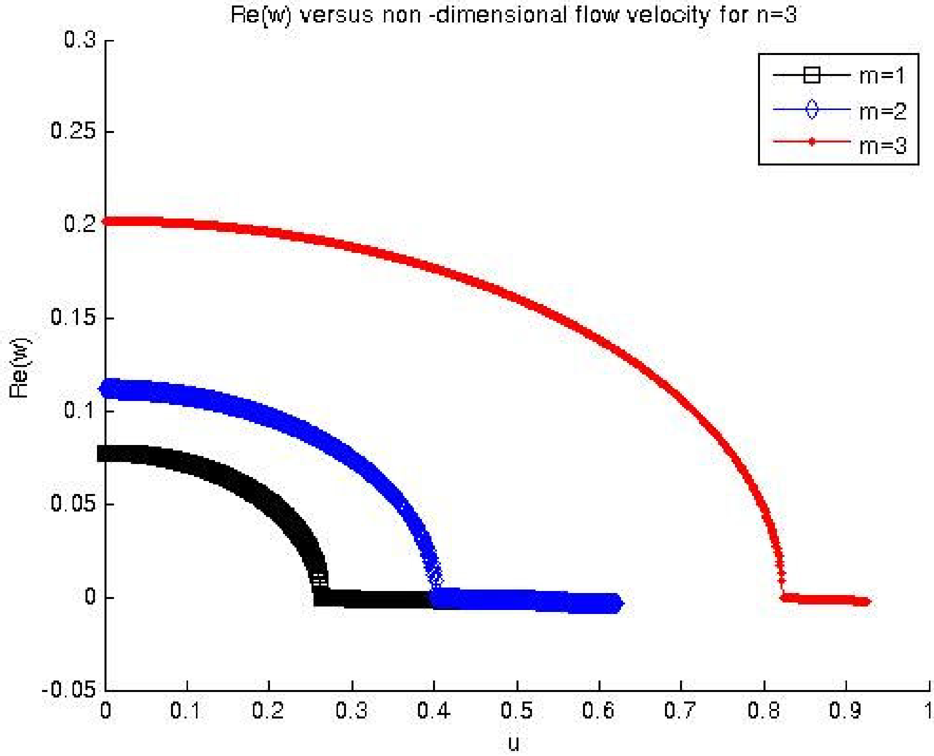

b)

Figure 2.8: a) Im(ω) and b) Re(ω) as a function of u for the 3rd circumferential mode of Pipe A

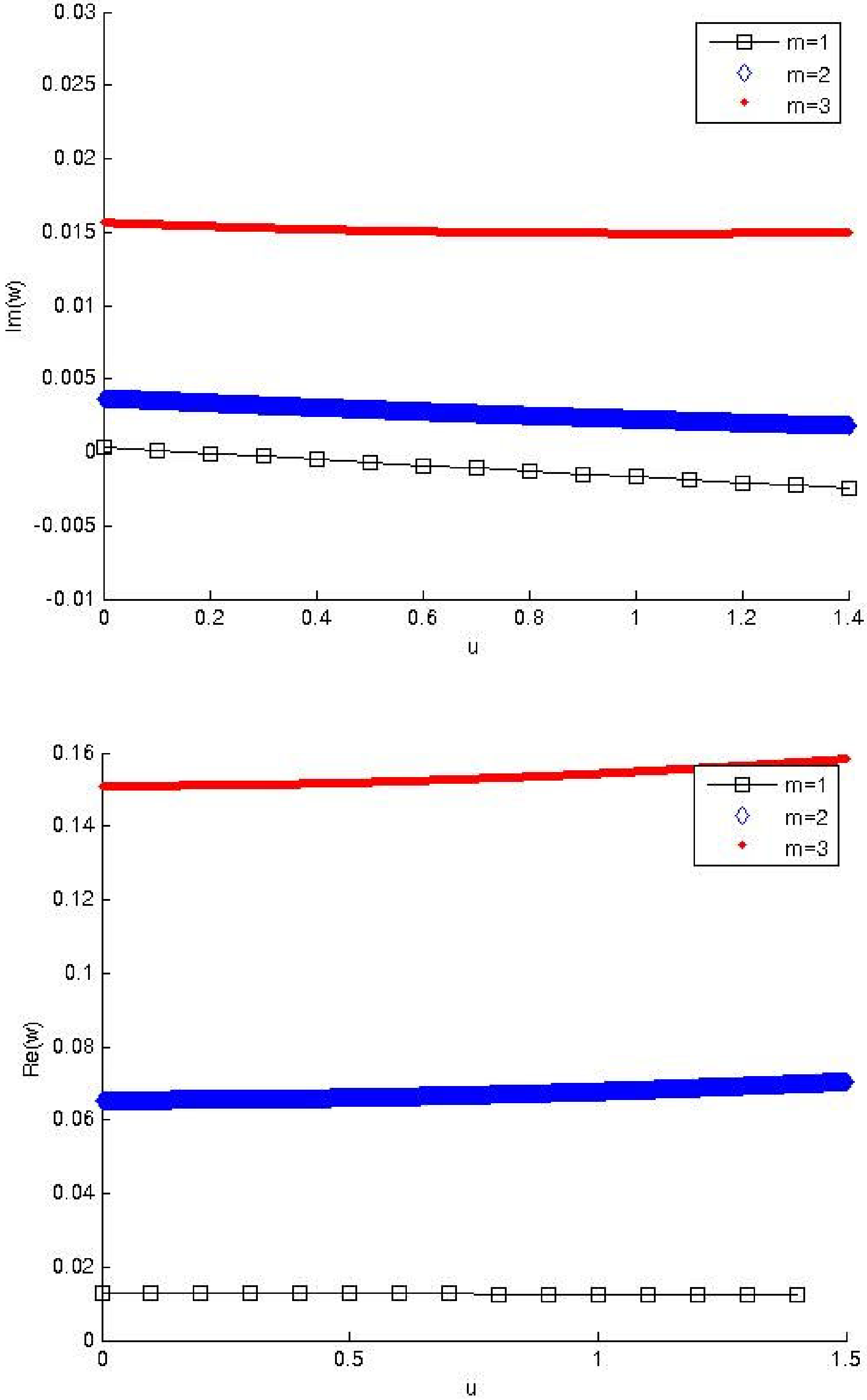

a)

b)

Figure 2.9: a) Im(ω) and b) Re(ω) as a function of u for the 1st circumferential mode of Pipe B

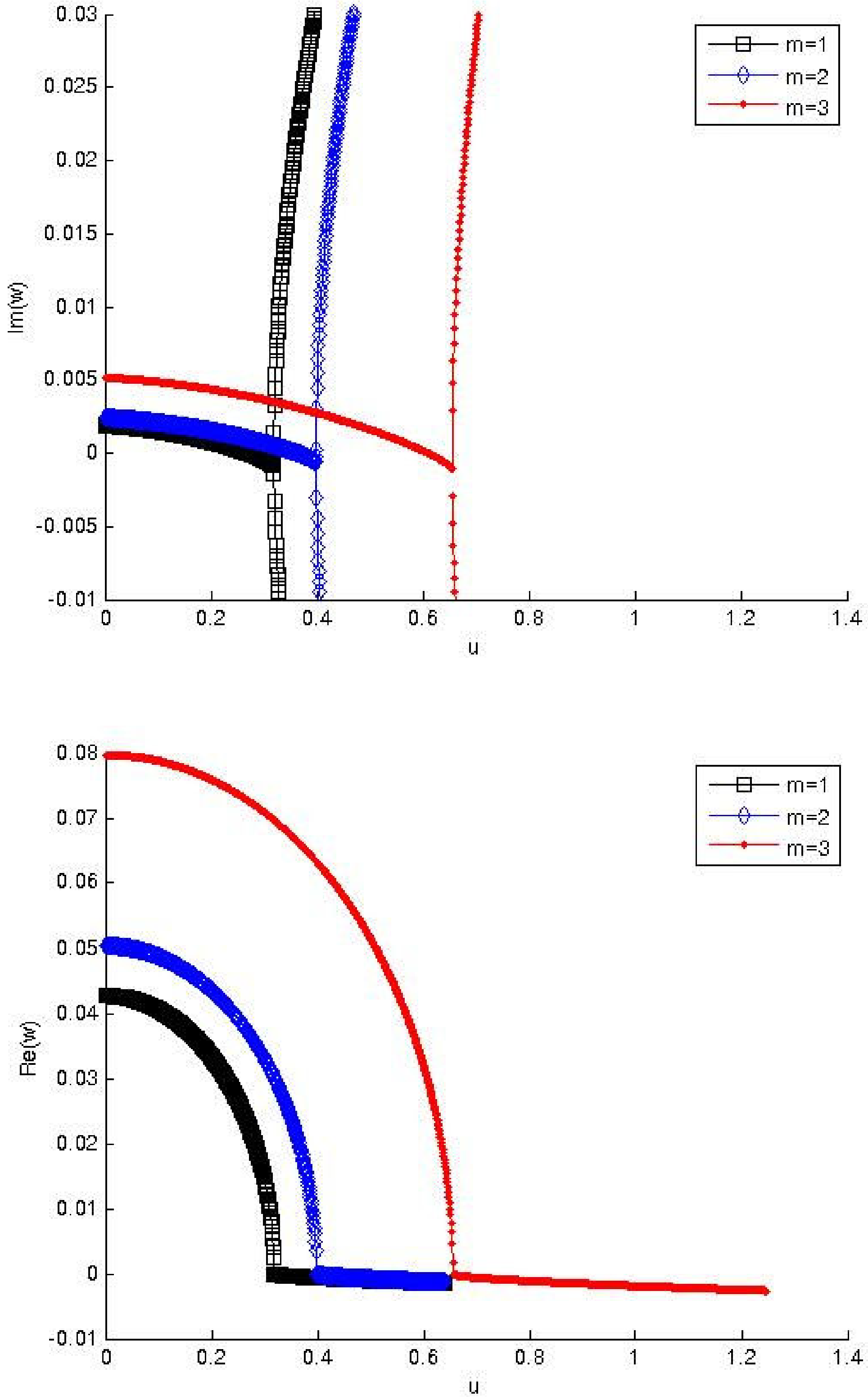

a)

b)

Figure 2.10: a) Im(ω) and b) Re(ω) as a function of u for the 2nd circumferential mode of Pipe B

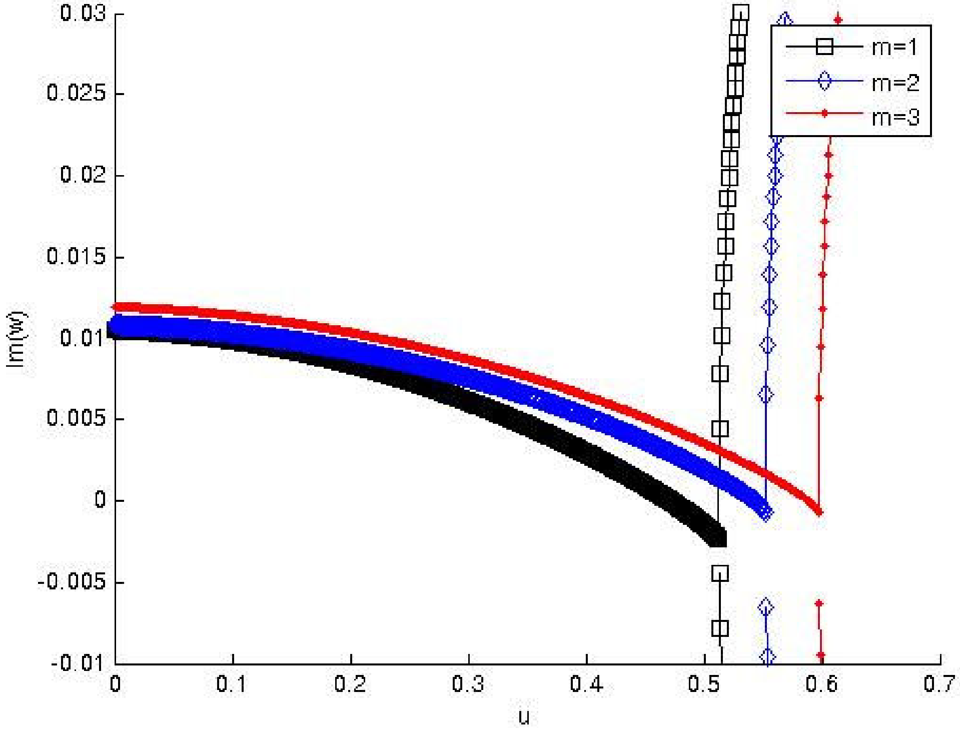

a)

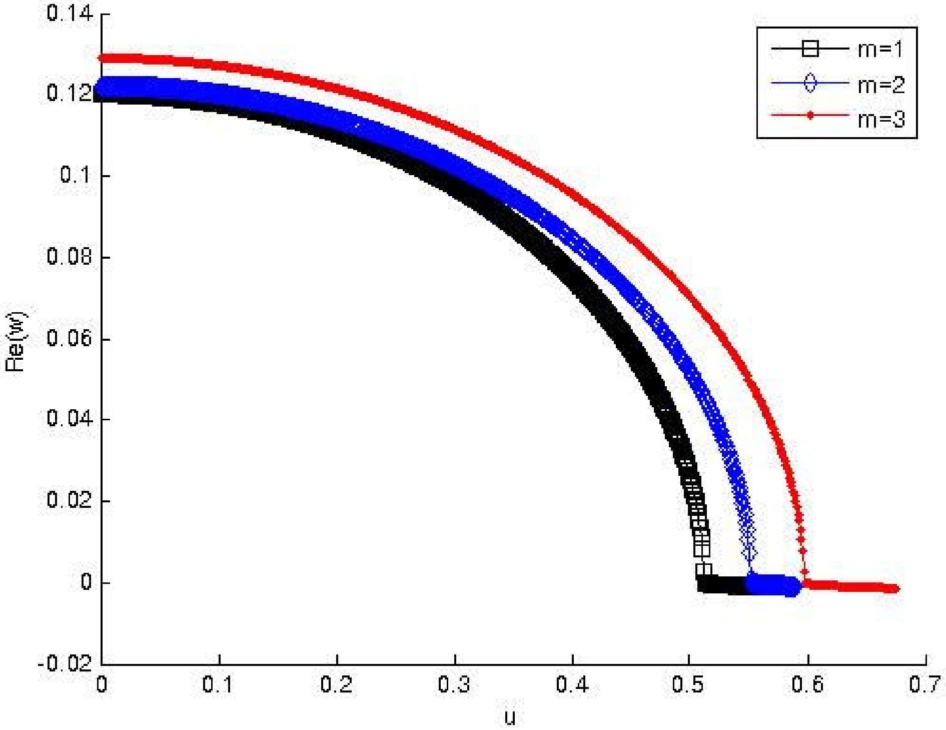

b)

Figure 2.11: a) Im(ω) and b) Re(ω) as a function of u for the 3rd circumferential mode of Pipe B

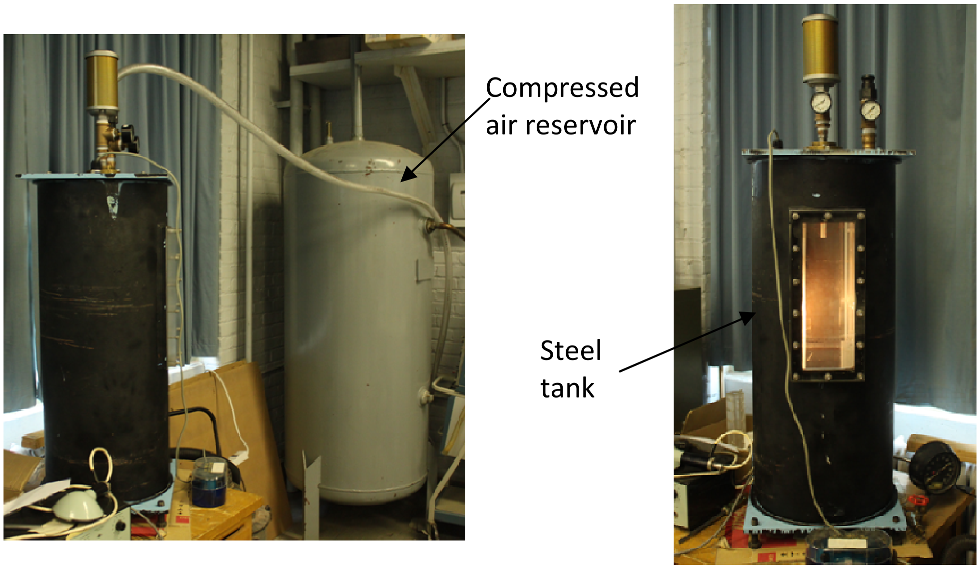

Figure 2.12: The experimental apparatus

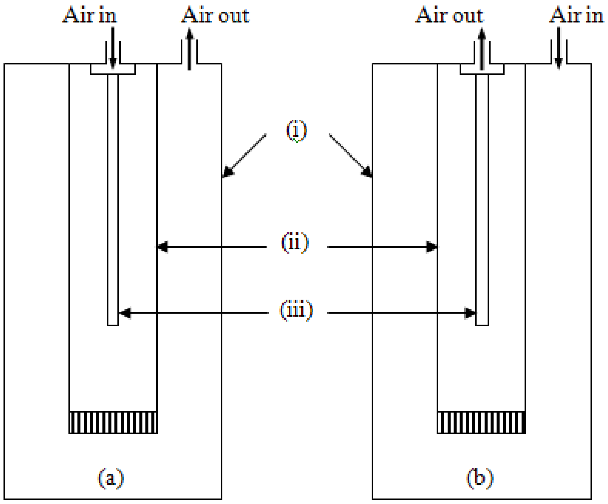

Figure 2.13: (a) Discharging configuration; (b) aspirating configuration.
(i) large steel tank; (ii) Plexiglas protective conduit; (iii) flexible elastomer pipe (after Rinaldi, 2009)

and Table 2.2. Pipe A is an ordinary elastomer pipe that is used in the laboratory for beam experiments. But it was with this pipe that the shell-type instability was first observed. That is why it was also studied here. As it appeared necessary to experimentally study the dynamics of a thinner pipe, a true shell, a new mould was designed to cast Pipe B. The schematics of the various pieces are given in Appendix E. For more details on the procedure of the conventional pipe casting process, on the determination of the Young's modulus and of the two damping parameters, and on the experimental procedure, the reader can refer to Rinaldi (2009).

For both pipes, the instability threshold is really sharp. The system is initially stable. When the velocity is increased, nothing happens up to a velocity at which the pipe suddenly loses stability.

For Pipe A, the system loses stability at:

$$\begin{cases} u_{cr} \approx 0.036 \\ U_{cr} \approx 2\ \mathrm{m/s} \end{cases} \quad (2.130)$$

As shown in Figure 2.14, the system loses stability by flutter in its second circumferential mode. But the phenomenon lasts only some seconds. Then, the pipe collapses rather quickly (Figure 2.15). If the air control valve is not closed, the pressure in the tank increases.

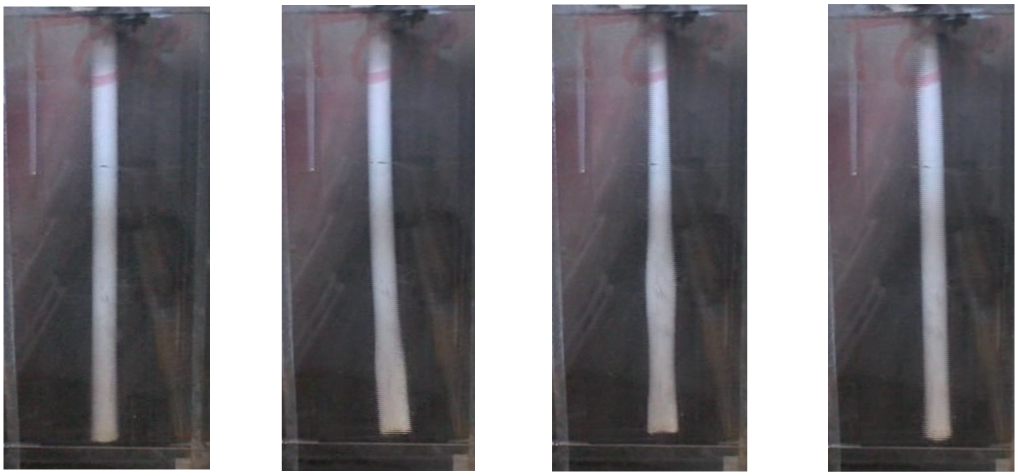

Figure 2.14: The observed shell-type instability with Pipe A

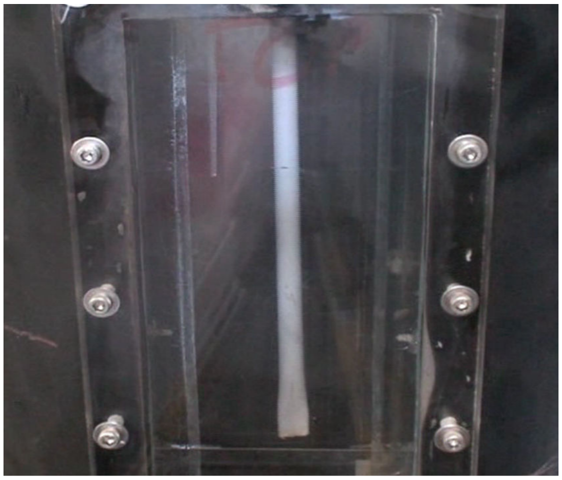

Figure 2.15: The collapse of Pipe A

With Pipe B, the critical flow velocity is even smaller:

$$\begin{cases} u_{cr} \approx 0.009 \\ U_{cr} \approx 0.5 \text{ m/s} \end{cases}. \tag{2.131}$$

To get a higher critical flow velocity, a PVC tube was placed inside the shell as shown in Figure 2.16. Despite making the observation easier, it did not change the critical flow velocity or the behaviour of the pipe.

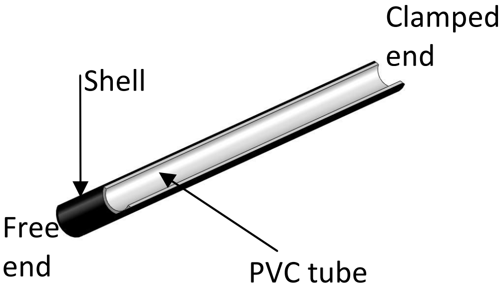

Figure 2.16: The thin shell and the PVC tube placed in it

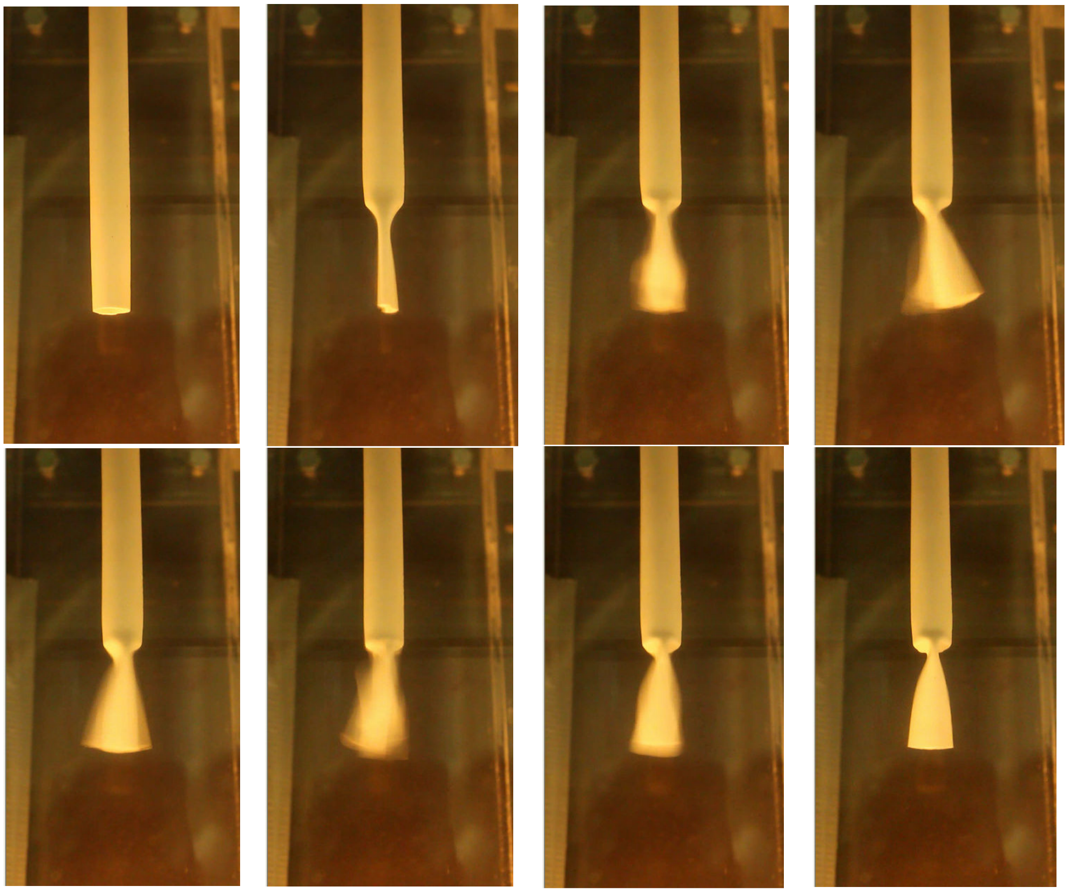

Figure 2.17: The observed shell-type instability followed by a collapse with Pipe B

As shown in Figure 2.17, at the critical flow velocity, the pipe collapses all along the shell, then experiences a shell-type instability in the second circumferential mode and finally collapses definitely in the same mode at the free end of the PVC tube.

2.6 Discussion

Table 2.3 presents a comparison between the theoretical and experimental results. The main comment that can be made is that the theory predicts qualitatively the first type of instability. However, the predicted critical flow velocity is overestimated: for Pipe A, it is more than two times higher and, for Pipe B, the ratio is close to nineteen. Furthermore, if experimental and theoretical predicted modes of instability are in good agreement for Pipe A, It is not the case for Pipe B. Actually, the theory predicts a loss of stability in the first circumferential mode while the experimental observation shows that the pipe exhibits a shell-type instability in its second circumferential mode. Finally, if the theory indeed predicts that the flutter is followed by buckling, the divergence is expected at higher flow velocity whereas, in the experiments, the flutter is followed by buckling at the same flow velocity.

Because of all these differences and especially the last one, a question arose: the phenomenon observed in the experiments, is it really flutter followed by buckling? Maybe, the first observed instability could be a divergence. In that case, what seems to be flutter in the experiments could be due to a frequent switch from one possible buckling state to another one, and the final buckling would be the final state of this phenomenon. But, these multiple collapses of the shell might not be exactly a flow-induced instability of the pipe. It could be due to the combination of the transmural pressure difference at the wall and of the really low stiffness of the material.

So it could be very interesting to conduct new experiments with a stiffer material. As it might be more difficult to reach sufficiently high flow velocity with air experiments, this work could be carried out with the new experimental apparatus, which is presented in Chapter 3, as the experiments could be conducted with water. Moreover, the analytical model certainly has to be improved. Firstly, the new boundary conditions developed for the case of an aspirating cantilevered shell should be reconsidered. Since the present theoretical model has been derived, a new insight has been has been developed by Giacobbi (2010) on this matter. It might be interesting to take that into account. Furthermore, as the flow at the free end is really not a jet, it should maybe not be considered that the flow is vertical before it enters the shell and the out-flow model should be modified to be closer to reality. To have a better understanding of the dynamics of the flow before it enters the pipe, it would be useful to develop a numerical approach. It might certainly help to develop this more realistic out-flow model.

Table 2.3: Comparison between the theoretical and experimental results

	Pipe A		Pipe B	
	Theory	Experiment	Theory	Experiment
u_{cr}	0.092	0.036	0.169	0.09
U_{cr} (m/s)	5.1	2	9.4	0.5
Type of instability	Flutter followed by buckling at higher flow velocity	Flutter followed by buckling at the same flow velocity	Flutter followed by buckling at higher flow velocity	Flutter followed by buckling at the same flow velocity
Mode of instability	n=2 and m=1	n=2	n=1 and m=1	n=2

Chapter 3: Experimental Study of the Stability of the Hanging Tubular Pipes Used in Salt Caverns

3.1 Introduction

Underground salt formations have been used over the past few decades as an alternative solution to store liquid hydrocarbons and natural gas. Salt dome caverns hollowed in these formations are very safe storage facilities. They are protected from fire, wilful damage and other hazards by the thousands of feet of rock above them. Furthermore, because of the extreme geological conditions at cavern depth, the salt walls are really hard and impermeable.

Underground salt deposits have been created through a natural process over the past millennia in certain areas throughout the world. They are present below the Earth's surface in two different configurations: salt domes and salt beds. Salt domes are really thick formations that can be as large as a mile in diameter and 30,000 feet in height. They can be found between 6,000 and 1,500 feet below the surface. Salt beds, on the other hand, are shallower and thinner formations that hardly exceed 1,000 feet in height; as a result, they are more prone to deterioration once a cavern has been formed. That is why salt domes are considered to be more suitable for salt cavern construction.

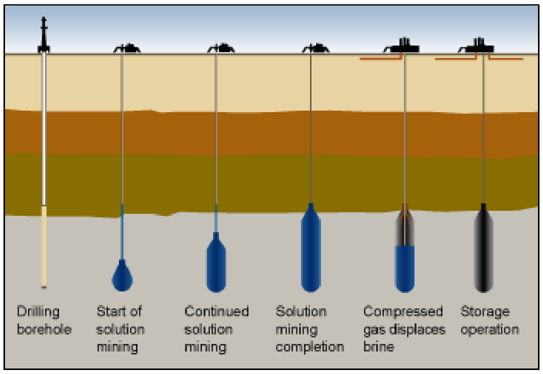

Figure 3.1: The different steps of the salt cavern formation and its use as storage facility (After AGL Resources website)

Salt caverns are hollowed in a process called “solution mining”. As shown in Figure 3.1, a well is first drilled down through the overlaying formations into the salt formation. Water is then injected into the well to dissolve the salt. The resulting very salty water, called brine, is then cycled back up the well. Thus salt has been extracted from the formation, leaving an empty space. Through this process, the cavern is gradually formed. Two different methods of circulation can be used. Either the fresh water is injected into the well tubing and brine is withdrawn through the annular space around it by a direct circulation process, or the water is injected through the annulus and the brine extracted via the tubing in a process called reverse circulation (see Figure 3.2).

Once the cavern is formed, it is ready to be used for storage. Even though it is sometimes used for disposal of waste, the main purpose is to store either natural gas or liquid hydrocarbons. Both of them are lighter than brine and will float on top of it. Thus, they are injected into the cavern through the annulus, while the brine is produced through the inner pipe. To withdraw the gas or hydrocarbons, the reverse process is applied.

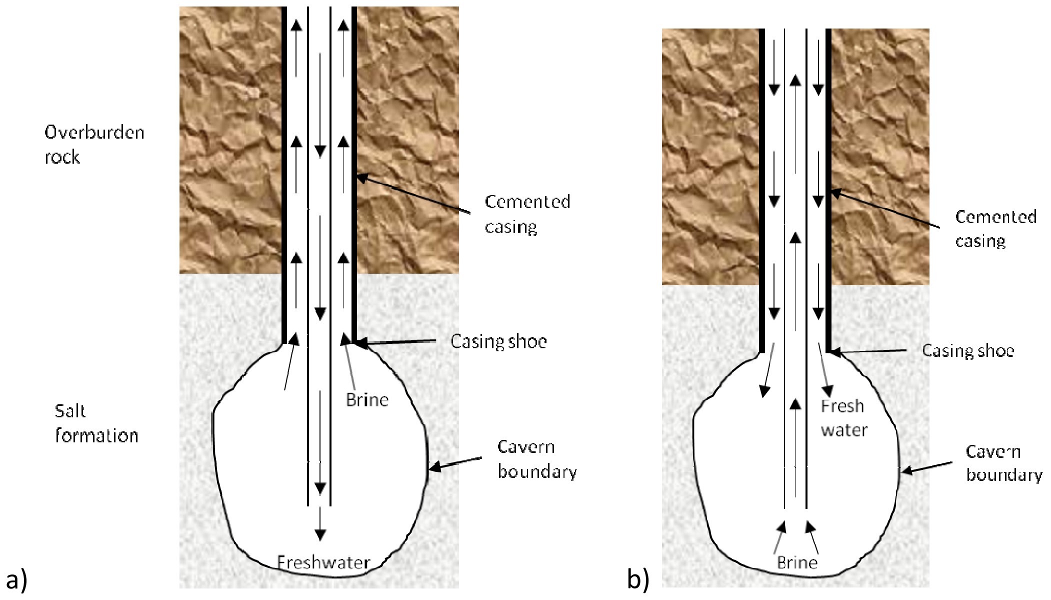

Figure 3.2: Flow direction in the so called a) direct circulation and b) reverse circulation

Salt caverns are very useful because they can be filled up more quickly than any other storage facilities and the product can be withdrawn on very short notice, which is of great interest in emergency situations.

As shown in Figure 3.2, the tubular system used for the injection or the withdrawal of the different fluids involved in the process consists of a cantilevered cylindrical pipe located inside a borehole cemented casing and then in the cavern. Thus, it can be seen as a system of two coaxial cylindrical structures simultaneously subjected to annular and internal flow. From what is known, it is not unreasonable to think that the system can experience a flow-induced instability, i.e. buckling or flutter, at high enough flow velocity. As a matter of fact, Ratigan (2008) reported that some industrial installations had experienced failures of the hanging tube (Figure 3.3). Here, by failure we understand a significant deformation of the tube, leading to a possible loss of isolation between the two flows inside and outside of the pipes. Ratigan listed four different possible reasons for failure: salt falls, pressure developed as a result of hydraulic transients, corrosion and wear, and fluid-elastic instability. The last one appeared to be the most often experienced; that is why Ratigan's report mainly focuses on that matter.

Data from more than 200 brine strings were collected, and sorted out according to different characteristics: if failure was experienced or not, if liquid or gas was stored in a domal or bedded salt cavern. Ratigan then compared this data with the theoretical critical flow velocities obtained from the linear theory of a hanging cantilevered beam conveying fluid. Such a system is presented in Figure 3.4. It consists of a uniform pipe of length L, mass per unit length m and flexural rigidity EI, conveying a fluid of mass per unit length M with mean axial flow velocity U. Figure 3.5 presents the dimensionless critical flow velocity u_{cf} for flutter of that system according to two dimensionless parameters. The first one,

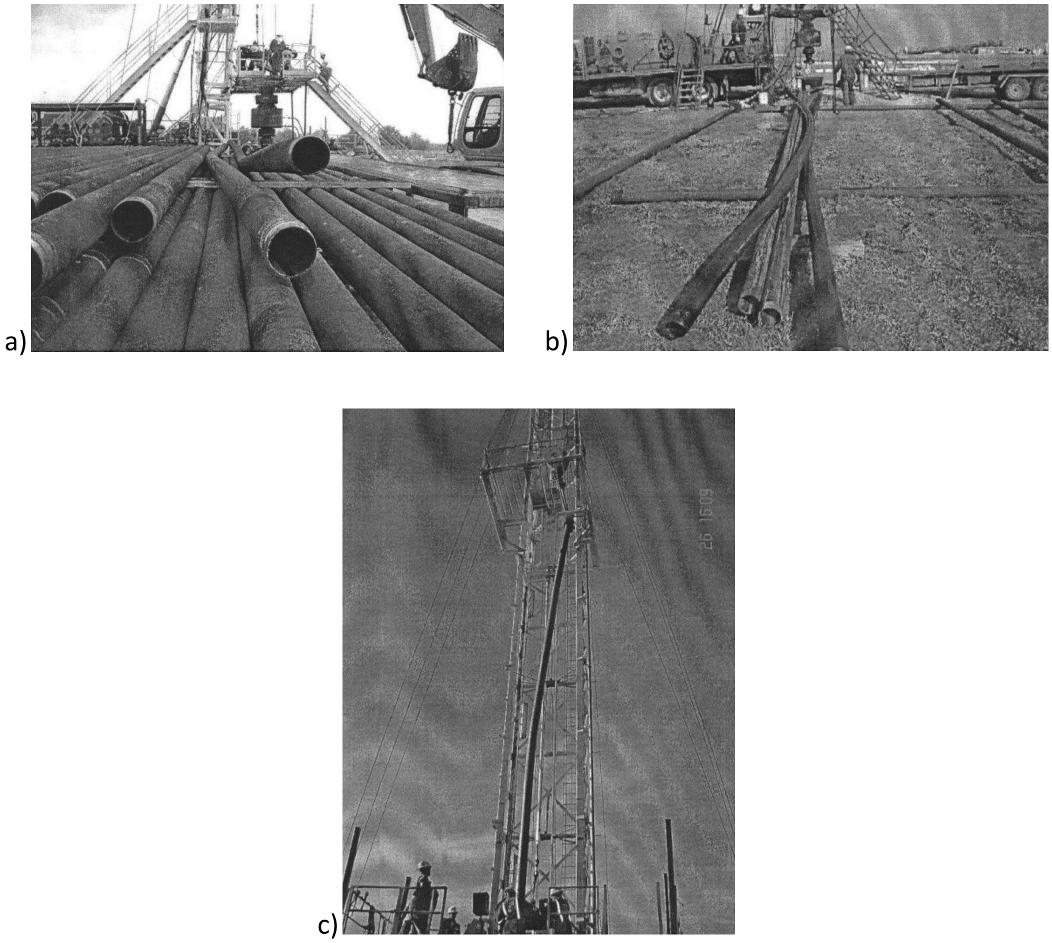

Figure 3.3: Brine string damage in a liquid storage well (a) in a salt dome, (b) in a bedded slat and (c) in a gas storage well in a salt dome (After Ratigan, 2008)

β, is a mass parameter. The second one, γ, is a nondimensionnal gravity parameter. These three parameters are defined by

$$u_{cf} = \sqrt{\frac{M}{EI}}LU, \qquad \beta = \frac{M}{m+M}, \qquad \gamma = \frac{(M+m)L^3}{EI}g. \tag{3.1}$$

It was found that the brine string should not have experienced any failure in almost any of the reported cases. The plotted data look quite the same whether the pipe failed or not. As it is highlighted in the report, some inconsistency between the theoretical model and reality could be the source of the incompatibilities in the results. As explained in the report, only the theory of a vertical cantilever has been considered. This means that only the dynamics of the part of the pipe hanging in the cavern was studied. Logically, Ratigan cast doubt on the validity of the boundary condition at the clamped end. Indeed, it is not correct to consider that the hanging pipe is fixed at the casing shoe because it is clamped at the top of the well. Thus, it is not possible to consider only the portion of the hanging beam in the cavern. And, as put forward by Ratigan, the annular flow between the string and the cemented casing, and the complex flows near the casing shoe and near the free end of the hanging pipe might be of great importance in the study of the dynamics of the system. Moreover, in the theory presented in the report, the clamped-free pipe is supposed to be surrounded by a very light fluid like air. Here, it is hung in water, brine, natural gas or liquid hydrocarbons. Finally, in this theory, only the case of a discharging pipe has been undertaken. The work done by Rinaldi (2009) shows that the dynamics of an aspirating pipe is very different. The above are some reasons that might explain why the collected data does not match with the theoretical results.

The present study was motivated by the failure problems presented by Ratigan, making obvious the necessity to understand better the dynamics of brine strings. The main work of this project has been to work out an experimental process to test the stability of the hanging pipe in various model configurations matching the industrial ones.

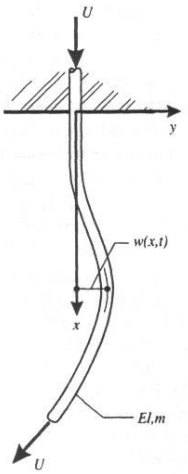

Figure 3.4: a flexible cantilevered pipe conveying fluid (After Païdoussis, 1998)

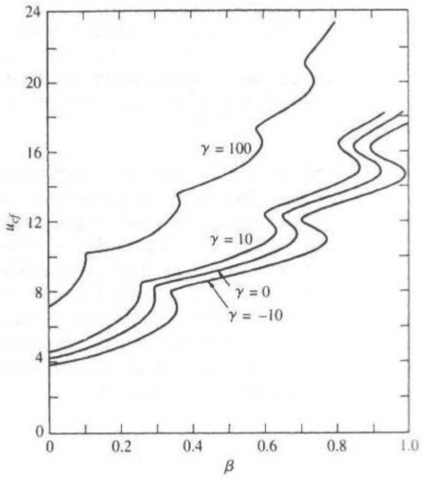

Figure 3.5: Dimensionless flow velocity for flutter of a vertical cantilevered pipe conveying fluid as a function of β for varying γ (After Païdoussis, 1998)

The main objectives of this set of experiments are to test whether or not a configuration can develop flow-induced instability and to measure the critical flow velocities. Thus, a quantitative comparison of those velocities can be undertaken. Moreover, as each model configuration corresponds to a specific cavern configuration, it might help to determine in which of those configurations the failures are more likely to occur. Furthermore, the amplitude and the frequency of oscillations should also be measured whenever it is possible.

The scope of this chapter is three-fold. Firstly, the model experiments and their correlation with the cavern configurations are described. Secondly, the design of the experimental apparatus that had to be assembled to observe the possible flutter or buckling of each configuration and determine the velocity at the onset of instability is detailed. Finally, the experimental results are presented and used to compare the relative stability of the various configurations.

3.2 The Experimental Configurations

In the process of solution mining and then of natural gas and liquid hydrocarbon storage, the flow path in the hanging pipe and in the annular region depends on the situation: drilling of the cavern with brine production, pressurization of a cavern for a Mechanical Integrity Test (MIT), or storage and withdrawal of the natural gas and liquid hydrocarbons. In the various possible configurations for storage and withdrawal, the cantilevered pipe can be hanging either in unconfined fluid (air or water) or confined by a larger rigid tube. In that case, the annulus is filled with quiescent or flowing fluid. That is why all these various configurations have to be defined and tested.

However, in the first configuration that has been tested, the hanging pipe discharges water in unconfined air. Although this configuration does not exist in industry, it is a really important one to test the apparatus because it is a reference case that has been widely studied. Table 3.1 and Figure 3.6 provide a detailed description and illustration of all the different configurations.

Table 3.1: The description of the different tested configurations

Configuration	Description
1	This is the reference configuration of a cantilevered pipe surrounded by unconfined air and discharging water.
2	This case is similar to the first one but in this case the pipe is surrounded by water in three ways: (i) in unconfined water, (ii) with the pipe confined by an outer rigid tube extending from 0 to ½*L* or (iii) from 0 to *L*.
3	Here the hanging pipe is aspirating the surrounding water. So this is the same as Configuration 2 but with the water flowing from the free end to the clamped one.
4	This is the same as Configuration 2ii and Configuration 2iii but with a discharging annular flow and no flow in the pipe.
5	This is the same as Configuration 4 but with an aspirating annular flow.
6	This is the same as Configuration 2ii and Configuration 2iii but also with an aspirating annular flow.
7	This is the same as Configuration 3ii and Configuration 3iii but also with a discharging annular flow.

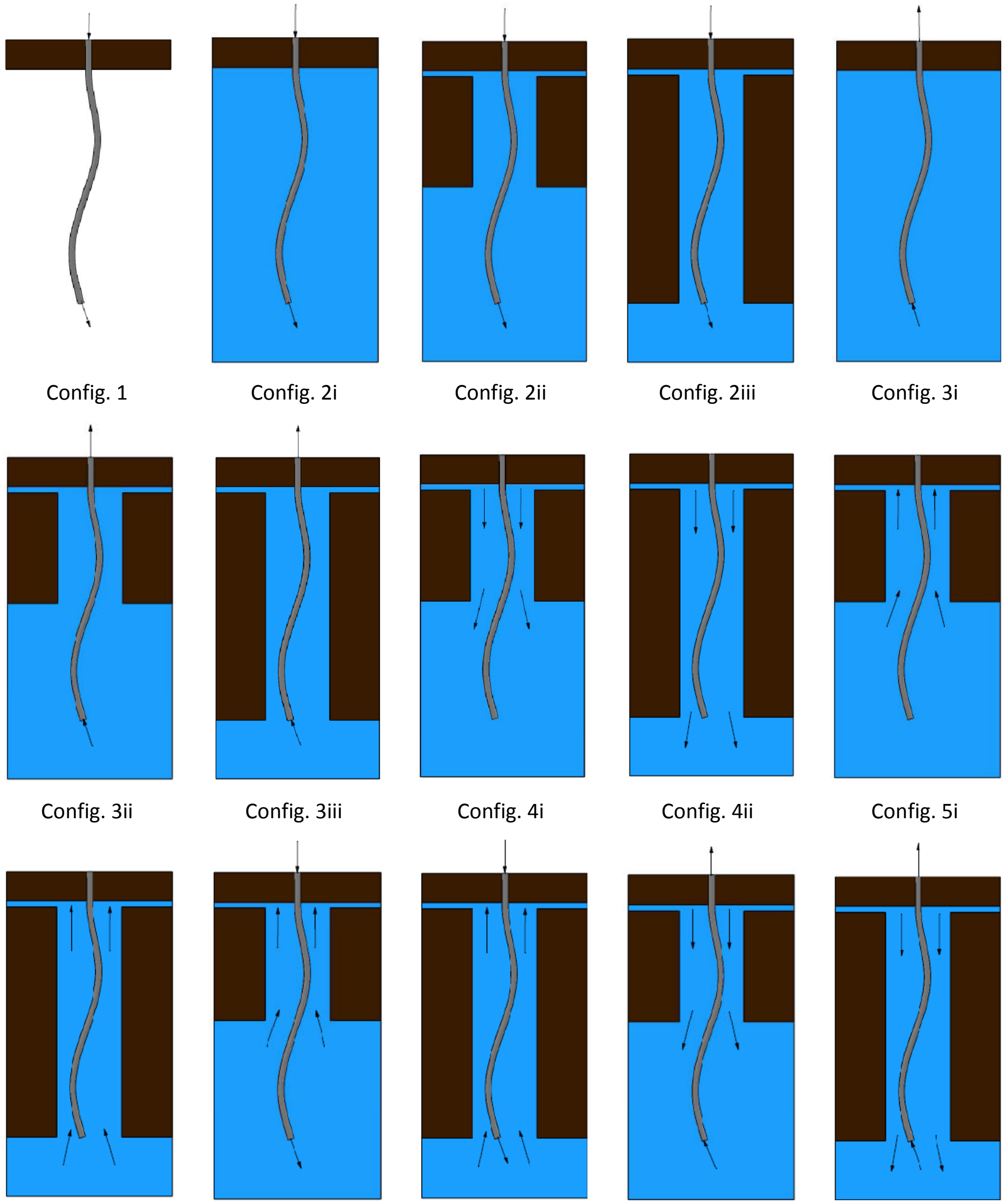

Config. 1 Config. 2i Config. 2ii Config. 2iii Config. 3i

Config. 3ii Config. 3iii Config. 4i Config. 4ii Config. 5i

Config. 5ii Config. 6i Config. 6ii Config. 7i Config.7ii

Figure 3.6: The experimental configurations

The experiments are to be run with different gap size and external tube length to determine the influence of these parameters on the stability of the coaxial system. To stay close to reality, the annular gap is ½ D_i or ¼ D_i in configurations involving an annulus, where D_i is the inner diameter of the inner pipe. The length of the outer rigid tube can be the same as the length of the inner pipe or half its length.

Furthermore, leakage-flow-induced instability was suggested as a possible explanation of brine string failure. Thus an additional ring constrictor can also be used in configurations involving an annular flow, to promote the onset of that kind of instability.

Table 3.2 provides a correlation of each model configuration with a specific cavern configuration.

Table 3.2: Correlation of models and cavern configuration

Configuration	Solution-mining or storage cavern configuration
1	Reference case of the cantilevered pipe discharging water
2i	Pressurization of a liquid cavern for a Mechanical Integrity Test (MIT)
2ii and 2iii	Pressurization of a liquid cavern for a MIT with cemented production casing modelled
3i	Depressurizing a liquid cavern after a MIT
3ii and 3iii	Depressurizing a liquid cavern after a MIT with cemented production casing modelled
4	Product injection in a liquid cavern without brine withdrawal
5	Product withdrawal from a liquid cavern without brine injection
6	Brine production in direct circulation or product withdrawal with brine injection
7	Brine production in reverse circulation or product injection with brine withdrawal

3.3 The Experimental Apparatus

Even though the flowing fluid can be water, brine, hydrocarbons or natural gas in the industrial applications, the experiments are all conducted with water, as described in the previous section. Two different flexible pipes made of elastomer were used in the experiments. Their geometry and properties are presented in the Table 3.3. The only difference between these two pipes is their internal diameter. The cemented casing is modelled by a rigid plexiglas tube. The transparency of the material allows the observation of the motion of the pipe located inside it. Because the flow velocities are not higher than 12 m/s (≈40 ft/s) and because the elastomer pipe is more flexible, the outer plexiglas tube can be considered as motionless. Various outer tubes can be used. Their characteristics are presented in Table 3.4. The free end of these tubes can be located either at the same height as the free end of the pipe or at half the length of the pipe.

To conduct these experiments, the first idea was to use an already existing apparatus, the same as used in the experiments of Chapter 2. It consists of a large steel tank connected to a reservoir of compressed air. It would have required significant modifications to conduct experiments with water flow – for example, the sealing has to be perfect – and with a possible outer tube. Because of these difficulties, it appeared more realistic to build an entirely new apparatus. It is presented in Figure 3.7. The experiments themselves are conducted in a large stainless steel tank connected on its top to a vessel which is of great importance. The whole is then connected to two pumps, a flow-meter and a water reservoir. The schematics of the various pieces are given in Appendix F.

Table 3.3: The geometrical and physical properties of the pipes

Properties	Pipe 1	Pipe 2
D_0 in meters (in)	0.0159 (0.626)	0.0159 (0.626)
D_i in meters (in)	0.00934 (0.368)	0.00635 (0.250)
L in meters (in)	0.445 (17.52)	0.445 (17.52)
EI in N.m^2	$7.28*10^{-3}$	$8.35*10^{-3}$
m in kg/m	0.144	0.189
M in kg/m	0.0686	0.0317
M_a in kg/m	$2.48*10^{-3}$	$2.48*10^{-3}$

Table 3.4: The properties of the different outer tube

	Tube 1	Tube 2	Tube 3	Tube 4	Tube 5	Tube 6
D_0 in inches (m)	1-1/4'' (0.0318)	1-1/4'' (0.0318)	1'' (0.0254)	1'' (0.0254)	1'' (0.0254)	1'' (0.0254)
D_i in inches (m)	1'' (0.0254)	1'' (0.0254)	7/8'' (0.0222)	7/8'' (0.0222)	3/4'' (0.0191)	3/4'' (0.0191)
L in inches (m)	7.445'' (0.189)	16.570'' (0.421)	7.445'' (0.189)	16.570'' (0.421)	7.445'' (0.189)	16.570'' (0.421)
Associated pipe	Pipe 1	Pipe 1	Pipe 2	Pipe 2	Pipe 2	Pipe 2

The tank (Figure 3.7) is made of stainless steel and was designed big enough so that the tested configuration could be considered as in an unconfined environment. The four plexiglas windows allow easy observation inside and the recording of the motion of the elastomer pipe. In the configurations that do not involve coaxial flows, the water has to enter at the bottom of the tank. To achieve a flow as straight as possible, two solutions were developed. Firstly, instead of letting the flow enter through one hole, a four-outlet manifold was added and connected to four holes located at the bottom of the tank (Figure 3.8). Secondly, in the configurations with a flow coming from the bottom, a perforated plastic plate was placed between the pipe and the bottom of the tank to decrease the intensity of the jet coming out of these four inlets. Nevertheless, the jets did not diffuse totally, so that a second perforated plate was added. In the other cases, a stainless steel mesh was added instead of the plastic one. It decreases the intensity of the jet coming from the pipe or the annular flow and, thus, it diminishes any a possible recirculation.

The vessel sitting on the top of the tank was a very difficult part to design. Its very important function is to separate the two coaxial flows. It has the same function as a BNC connector at the end of a coaxial cable that physically separates the electric current from the two conductors: the centre core and the metallic shield. In the configurations involving two counter-current coaxial flows, it is necessary that the flow reaches and leaves the tank through two different hoses and that there is absolutely no connection between the two flows. To achieve this, the vessel presented in Figure 3.8 and Figure 3.9 was designed. The most serious difficulty was to ensure the sealing of the apparatus and still be able to open the vessel in case a piece had to be changed. The flow going through the inner pipe runs inside a straight tube in the vessel. At the top of the vessel, the sealing between this tube and the top cover is provided by an O-ring located in an additional part attached to the cover by bolts (Figure 3.9). The water from the annular flow surrounds the straight pipe in the vessel and is collected by a six-outlet manifold connected to six holes located on the side of the vessel. It was decided to use more than one hole so that the incoming flow would be split equally in the vessel. The flow then goes from the vessel to the annular region through ten equally spaced holes; that guarantees the homogeneity of the flow in the annular region.

Figure 3.7: The experimental apparatus

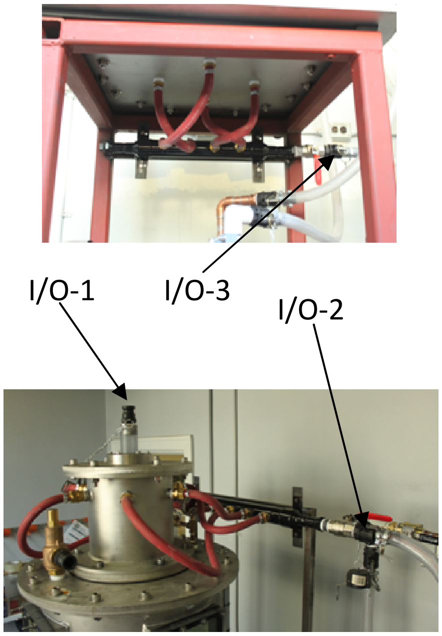

Figure 3.8: The vessel, the bottom of the tank and the three input/output ports

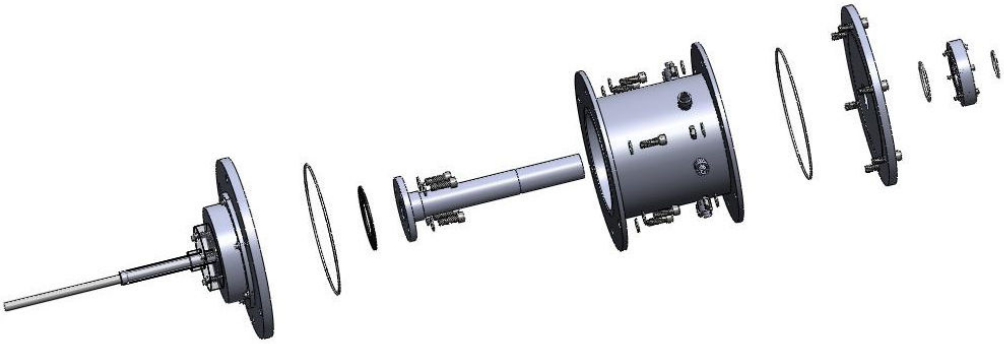

Figure 3.9: Exploded view of the vessel

A white plastic reservoir located on the right side of Figure 3.7 is also an important part of the apparatus. It has multiple functions. Firstly, as pointed out by its name, it is used as a water reservoir. It is from this reservoir that the water is aspirated and injected in the system. It then goes back to the reservoir. It is also useful when the tank has to be emptied. Thus the water is not wasted every time the pipe configuration has to be changed. It is also used to gather the water coming from the release valve described later if the pressure in the tank becomes too high. It has an overflow in case there is too much water in the system. Finally, as it is opened to air through a vent, the system is not hermetically closed and the water surface of the reservoir is at atmospheric pressure; it prevents the existence of too high a pressure in the apparatus.

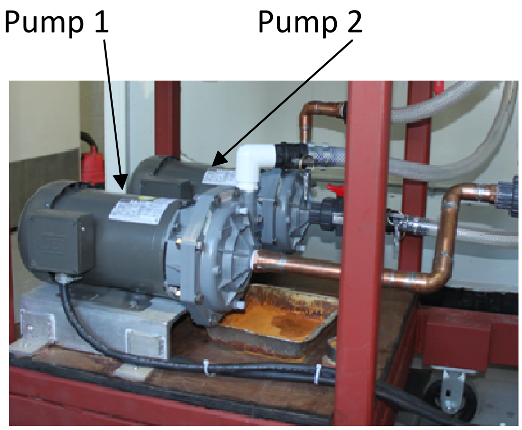

Figure 3.10: The two pumps

Figure 3.11: The quick connect system

As shown at the bottom of Figure 3.7, two drives modulate the power of two pumps (Figure 3.10). These two pumps are not used in the same way. One injects water (Pump 1) while the other one aspirates it from the tank (Pump 2). Depending on the configuration, each pump is connected to one of the three input/output piping systems described above: one for the pipe flow (I/O-1), one for the annular flow (I/O-2) and one at the bottom of the tank (I/O-3). For example, in the usual case of a pipe discharging water and surrounded by air, Pump 1 connected to I/O-1 injects water in the pipe, while Pump 2 connected to I/O-3 is used to maintain a constant water level in the tank; I/O-2 is closed. As the connections need to be changed for each configuration, a quick connect system (Figure 3.11) is used, so that this can be done easily and quickly. For measurement and safety reasons, a pressure gauge and a release valve are located at the top of the tank (Figure 3.12). Thus, this pressure cannot be higher than 75 psi, otherwise the release valve opens and the overflow goes to the plastic reservoir.

To measure the flow velocity, a magnetic flow-meter (Figure 3.13) is located after the first pump. It operates as a noncontacting instrumentation that consists of a sensor and a transmitter with a local operator interface. It uses the conducting properties of water that contains ions to get the fluid flow rate. The other useful information that was recorded whenever possible is the frequency and the amplitude of oscillation of the cantilevered pipe.

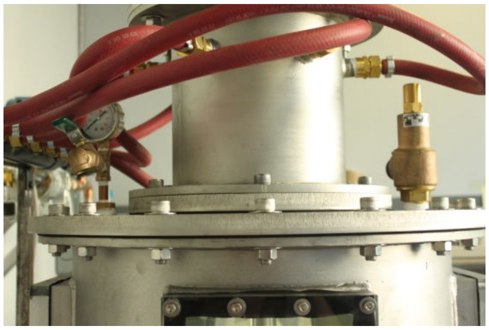

Figure 3.12: The pressure gauge and the release valve located on the top cover of the tank

Figure 3.13: The magnetic flow-meter and its local operator interface

To acquire the frequency of the oscillations, a laser (Figure 3.14) is used. It allows to measure the distance between the instrument and the pipe, and, thus, to get a time signal of the motion of a point on the pipe. At first, it appeared possible to calibrate it to know the conversion between the signal given by the laser and the effective displacement of the pipe. But it is not that simple, firstly because the motion of the pipe is not always planar and, secondly, when it is planar, the plane of motion is rarely the same as the measurement plane of the laser. So the laser measurements were used to get the frequency of the motion by analysing the acquired time signal using a Matlab® program. In the end, the amplitude was more roughly measured using a ruler attached to one of the windows of the tank. To be as accurate as possible, pictures were taken with a camera attached to a tripod. It was always placed at the same location, so that it is possible to get the effective displacement of the pipe by multiplying the measured displacement, with the ruler graduated in centimetres, by a factor dependent on the fluid inside the tank (Figure 3.15).

Figure 3.14: The laser device

Figure 3.15: The amplitude measurement device

3.4 Experimental Observations

Because of the great diversity of studied configurations, the observations made for each of them are presented separately in this section. However, comparisons between different configurations are made on some occasions, e.g. to say that the pipe has the same dynamical behaviour. A whole set of experiments is presented using Pipe 1 and Tubes 1 and 2. The configuration of a cantilevered pipe discharging water in air was first studied and compared to the theory, as it is the reference case.

For each experiment, the velocity is gradually increased from zero to the velocity after which the dynamics of the pipe does not change anymore. When there is flow inside the pipe, flow velocities cited are the flow velocities in the pipe. Otherwise, it is the flow velocity in the annular gap. The motion amplitude is denoted by *A* and the frequency by *f*.

3.4.1 Configuration 1

In this configuration, the very first vibrations of the pipe are observed at *U*=6.57 m/s but their amplitude is really small (*A*<1 cm) and there is no definite frequency. The Fast Fourier Transform (FFT) algorithm shows the existence of two or three peaks around 4.1 Hz. At $U_{cf} = 6.94\ \mathrm{m/s}$, the amplitude suddenly increases as shown in Figure 3.16.b. This is the instability threshold. At this point, we have $f = 4.15\ \mathrm{Hz}$ and $A = 21\ \mathrm{cm}$. In that case, the motion of the pipe is really simple and simple-harmonic. It oscillates in a plane that does not change with time. From this point, the pipe dynamics remains qualitatively the same. It is a planar oscillation in the third mode of the pipe. The frequency of oscillation gradually increases with flow velocity (Figure 3.16.a) as well as the amplitude, to reach $f = 4.61\ \mathrm{Hz}$ and $A = 26\ \mathrm{cm}$ at $U = 8.0\ \mathrm{m/s}$.

The standard theoretical model for a cantilevered pipe discharging water in air predicts a loss of stability by flutter in the third mode at $U_{cf} = 6.84\ \mathrm{m/s}$

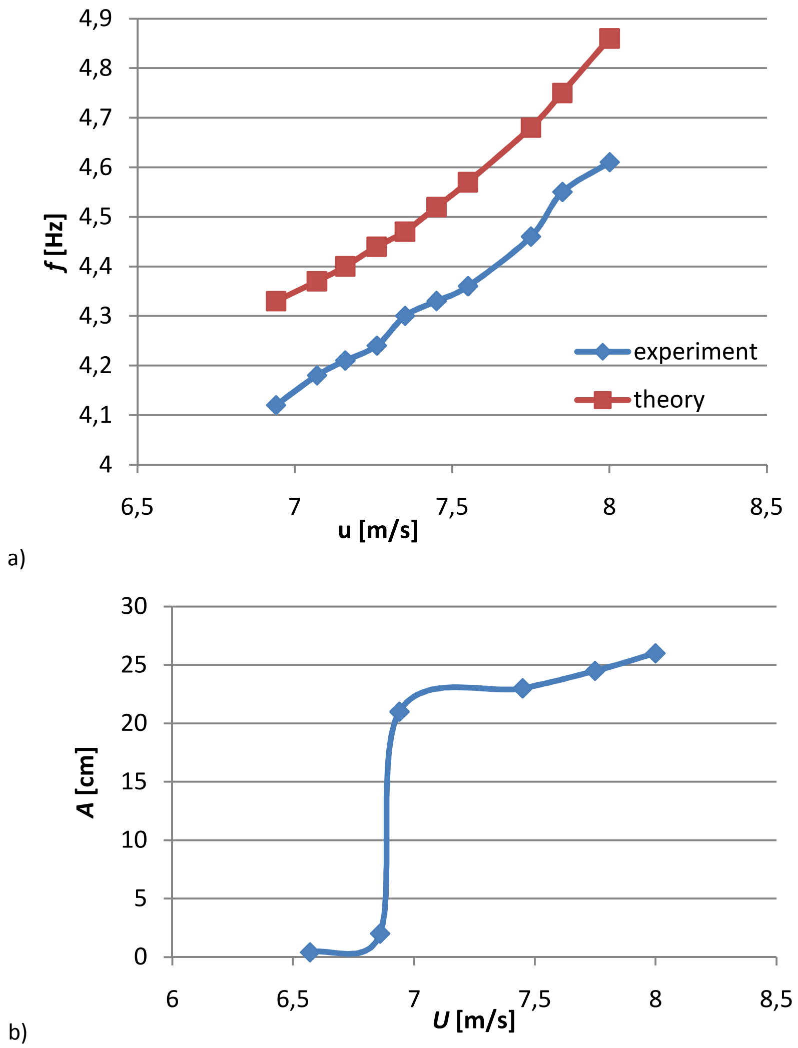

Figure 3.16: a) The comparison between theoretical and experimental frequencies and b) the observed amplitude with Pipe 1 in configuration 1

with a frequency $f = 4.24\text{Hz}$. Furthermore, Figure 3.16.a shows the comparison between predicted and experimental frequencies with increasing flow velocity. It shows that the experimental results differ from the theoretical ones by less than 5%. They are therefore judged to be in really good agreement.

3.4.2 Configuration 2i

Unlike the case of a cantilevered pipe discharging water in air, the instability of the pipe immerged in water develops much more gradually. The critical flow velocity, $U = 3.93\ \text{m/s}$, is much lower than in Configuration 1. This was expected (see Figure 3.5) as the coefficient β is smaller because of the surrounding water. From the threshold of instability, as shown in Figure 3.17, the pipe dynamics is divided into two parts. For $3.93 \leq U \leq 4.69$, the amplitude increases slowly from $A = 0.4$ cm to $A = 8$ cm, while the frequency displays the opposite behaviour, decreasing from $f = 1.40$ Hz to $f = 1.10$ Hz. The axial mode of oscillations is the second one. For $3.93 \leq U \leq 4.45$, the oscillations are planar but the plane of oscillation is regularly changing. At higher flow velocities, the frequency of motion is clearly distinguishable but the pipe motion is more complex and comprises two phases: (i) a periodic planar motion alternating with (ii) a phase during which the free end of the pipe performs figure-of-eight motion.

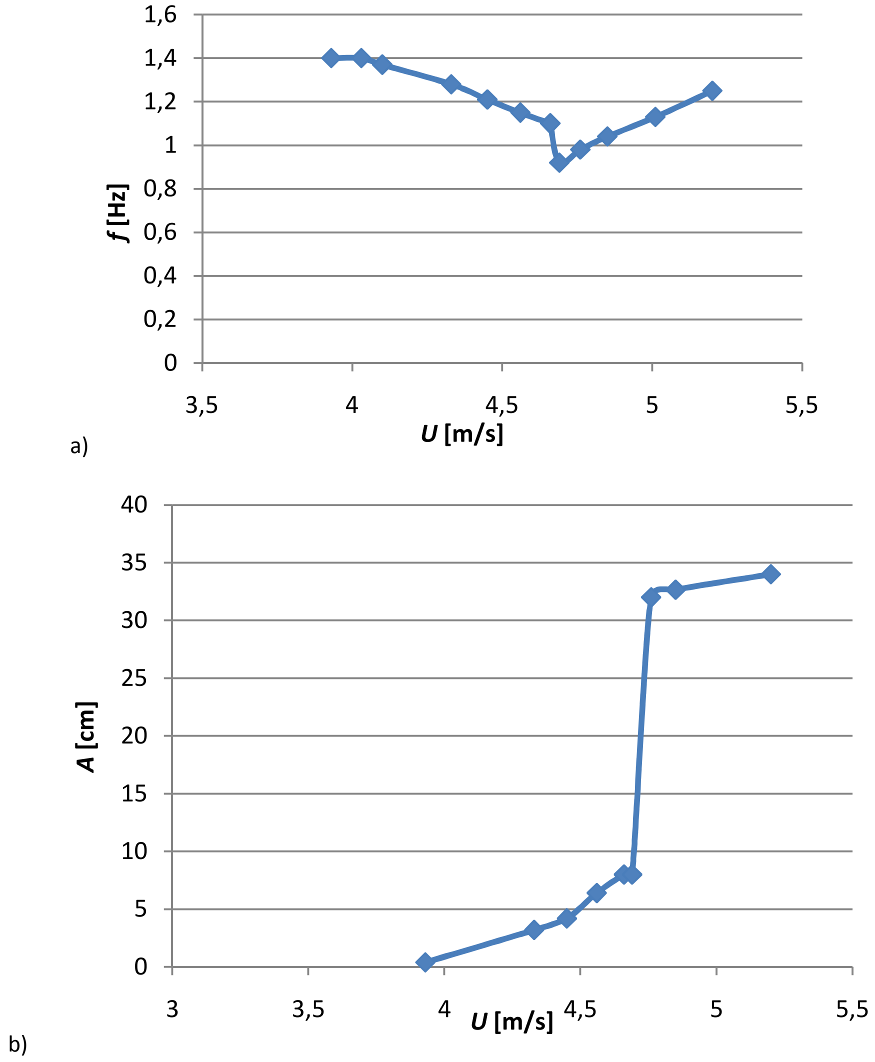

Figure 3.17: a) The experimental frequency and b) amplitude versus velocity with Pipe 1 in configuration 2i

Figure 3.18: Successive instantaneous views of the rotating motion of the pipe at $\boldsymbol{U = 5.20\ \mathrm{m/s}}$

The pipe dynamics suddenly changes at $U = 4.76\ \mathrm{m/s}$. The amplitude increases suddenly to $A = 32\ \mathrm{cm}$ and the frequency drops to $f = 0.92\ \mathrm{Hz}$. At the beginning, the oscillations are planar and still in the second mode but, after a while, the free end of the pipe performs a rotating motion along the wall of the tank (see Figure 3.18). It appears that this 3-D motion might be due to the vicinity of the tank wall when the amplitude of oscillation is really high ($A \approx 32\ \mathrm{cm}$) as a result of the jet issuing from the pipe impacting this wall. But the dynamics of the pipe in configuration 2ii lets us think that this is the natural behaviour of this cantilevered pipe discharging water in essentially unconfined water. From this point on, the pipe does not stop its rotating motion, and the amplitude as well as the frequency increase slowly.

3.4.3 Configuration 2ii

In this configuration, the pipe motion is constrained by the presence of an outer plexiglas tube whose length is half that of the pipe. This, it has been found, does not change the critical flow velocity and frequency, but it has a great influence on the dynamics of the pipe. In this configuration, the behaviour of the pipe can be divided into three ranges, as shown in Figure 3.19.

Firstly, for $4.21 \leq U \leq 5.77$, the pipe oscillates in its second mode with small amplitude in a plane that sometimes changes. The amplitude slowly increases and, in contrast to configuration 2i, the frequency also increases from 1.25 Hz to 2.25 Hz. The pipe impacting on the outer tube is certainly the reason for this difference in behaviour between configurations 2i and 2ii.

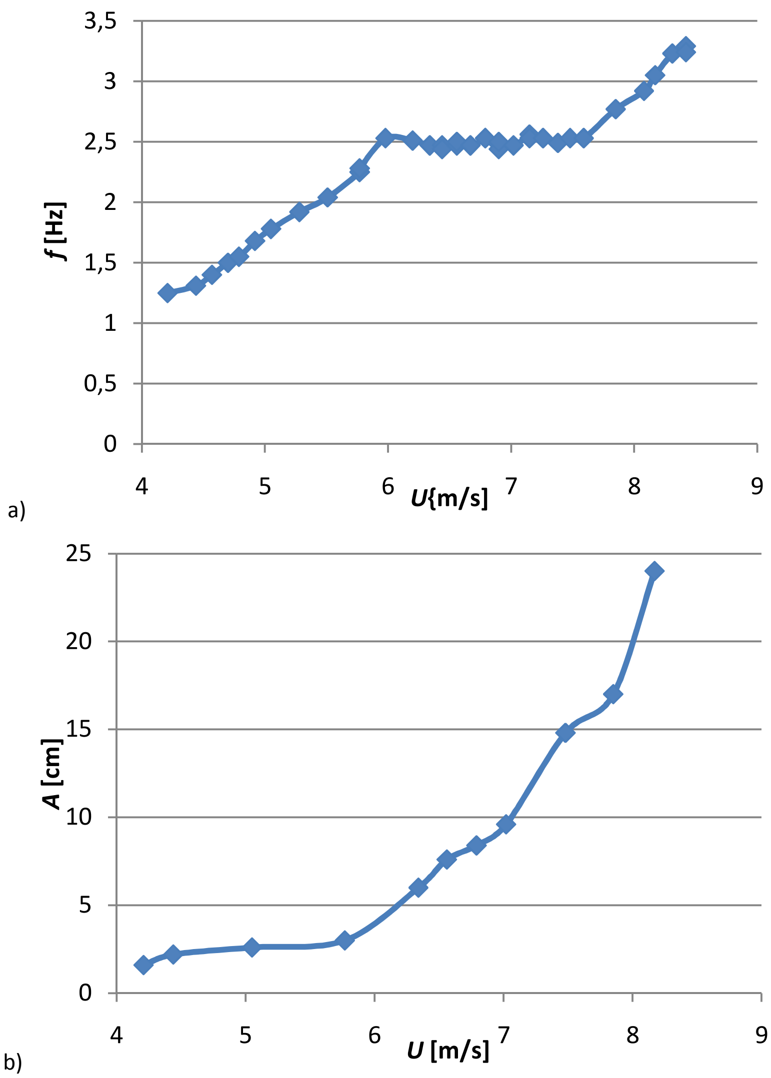

Figure 3.19: a) The experimental frequency and b) amplitude versus velocity with Pipe 1 in configuration 2ii

Then, for $5.77 \leq U \leq 6.34$, the oscillation mode smoothly changes from second to third axial mode. At $U = 6.34\ \mathrm{m/s}$, the pipe oscillates mainly in its third mode. At the same time, the motion of the pipe becomes more complex. Periods of chaotic motion without a definite frequency alternate with periods of periodic planar oscillations. This behaviour extends as far as $U = 7.38\ \mathrm{m/s}$. The frequency remains stable at $f = 2.50\ \mathrm{Hz}$ but the amplitude increases more rapidly than in the previous flow range.

Finally, the amplitude abruptly increases from 9.6 cm to 14.8 cm at $U = 7.59\ \mathrm{m/s}$. There is no jump in the frequency but, from this point, the frequency increases again and the slope of the amplitude curve is really steep. At $U = 7.85\ \mathrm{m/s}$, the pipe begins to rotate as in configuration 2i, but rotation periods alternate with third mode planar motion periods. Thus, in the presence of the outer tube, the pipe begins to rotate at higher flow velocity ($U = 4.76\ \mathrm{m/s}$ in configuration 2i and $U = 7.85\ \mathrm{m/s}$ in configuration 2ii) and the frequency of oscillation or rotation is around twice the one without the outer tube. Thus, the presence of the outer tube really changes the dynamical behaviour of the pipe. This, at first sight, seems surprising, as the only change to the system, due to the presence of the outer tube, is to increase the added mass on the upper part.

3.4.4 Configuration 2iii

Overall, the only instability that is observed with an outer tube all along the pipe is buckling. It appears around $U = 1\ \mathrm{m/s}$. The free end of the pipe moves away from its equilibrium position until it touches the plexiglas tube at $U = 2.69\ \mathrm{m/s}$ (see Figure 3.20.a). From that point to $U = 6.80\ \mathrm{m/s}$, the pipe diverges in its first mode. While the velocity is increased, a greater part of the pipe is in contact with the outer tube as shown in Figure 3.20.b. The opposite behaviour is observable for $6.33 \leq U \leq 6.80$. At this velocity, the upper part of the pipe moves away from the outer tube and the pipe suddenly diverges in its second mode (see Figure 3.20.c). At higher flow velocity up to $U = 9.70\ \mathrm{m/s}$, there is no change in the dynamics of the pipe.

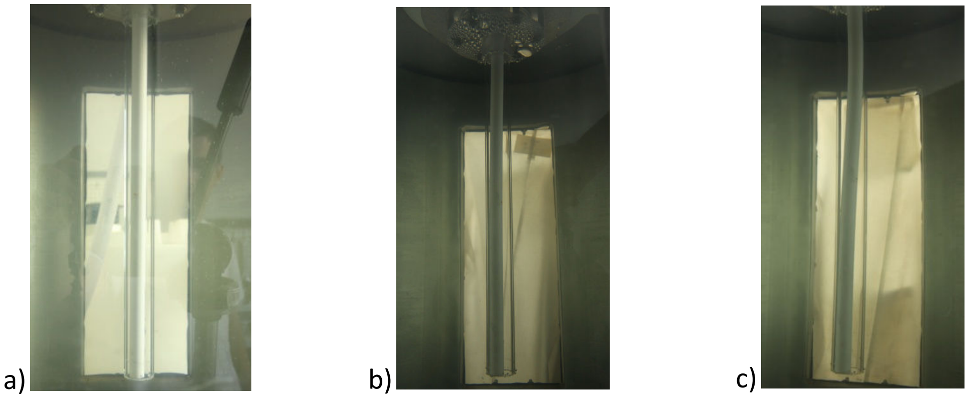

Figure 3.20: The buckling of the pipe 1 in Configuration 2iii at a) *U*=2.69, b) *U*=5.37 and c) *U*=8.06 m/s

Thus, the longer outer tube completely changes the dynamics of the system, as only buckling is experienced and only in the first and second modes; whereas in configurations 2i and 2ii, the pipe develops oscillations successively in its second and third mode. Whether this change in dynamical behaviour is due to the presence of the longer tube or to imperfection-initiated buckling against the plexiglas tube, which is then perpetuated nonlinearly, is not clear.

3.4.5 Configuration 3i

In this configuration, the pipe is hanging in unconfined water as in Configuration 2i, but, here, the pipe is aspirating water, i.e. the water is flowing from the free end to the clamped end. In this configuration and all the other configurations in which the pipe is aspirating the fluid, a shell-type collapse of the pipe was experienced at low flow velocity and persisted thereafter. To avoid this occurrence without constraining the motion of the pipe, a helical spring was added inside and all along the pipe.

At zero flow velocity, there is a slight bending of the pipe, which is due to the inside spring not being perfectly straight. But, as shown in Figure 3.21.b and Figure 3.22, the flow has a stabilizing effect on the pipe at low flow velocities and the bending decreases and dies out at $U = 3.13\ \mathrm{m/s}$.

The pipe then loses stability by flutter in its first mode at $U = 3.39\ \mathrm{m/s}$. At the beginning, the amplitude is really small, increasing smoothly. The frequency of oscillation is $f = 0.37\ \mathrm{Hz}$ and it remains the same during the experiments. Although the oscillation is planar, the behaviour of the pipe is not that simple. In fact, periods of periodic planar motion alternate with periods of chaotic motion. First, the periods of periodic motion are not observable for more than a few seconds, but they last longer as the flow velocity increases and can last as long as fifteen seconds.

At $U = 4.19\ \mathrm{m/s}$, a new instability arises. A first mode buckling overlaps the first mode flutter. Its amplitude increases very quickly to $A = 1\ \mathrm{cm}$ at

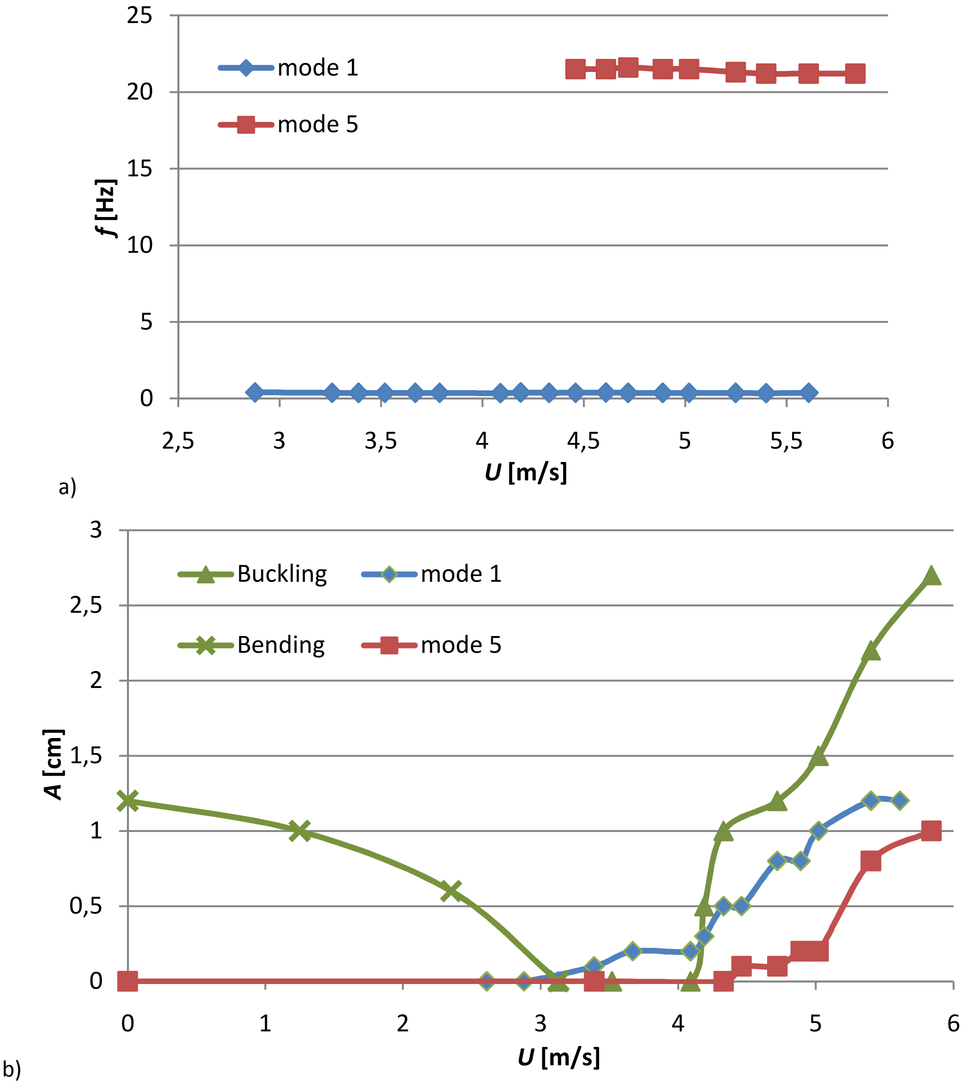

Figure 3.21: a) The experimental frequency and b) amplitude versus velocity with Pipe 1 in configuration 3i

$U = 4.33\ \mathrm{m/s}$ and, then, to $A = 2.7\ \mathrm{cm}$ at $U = 5.84\ \mathrm{m/s}$. From this velocity, the amplitude of the first mode flutter increases more rapidly, reaching $A = 1.2\ \mathrm{cm}$ at $U = 5.40\ \mathrm{m/s}$.

At $U = 4.46\ \mathrm{m/s}$, another instability is observable: a flutter of the pipe in its fifth mode superimposed on the first mode flutter. First, it is difficult to determine the mode of this instability because the amplitude is really small, but it becomes obvious at higher flow velocities. The frequency is close to $f = 21.5\ \mathrm{Hz}$ and it does not change much with flow. Thus, from this flow velocity on, the pipe exhibits at the same time a first mode flutter, a first mode buckling and a fifth mode flutter (Figure 3.23). At first, the peak corresponding to the fifth mode frequency, in the power spectrum, is a minor peak in comparison to the peak corresponding to the first mode flutter. But, it becomes more important as the flow velocity is increased. In the mean time, the periods of shuddering motion of the first mode are more and more frequently observable. At $U = 5.40\ \mathrm{m/s}$, the amplitude of the fifth mode increases suddenly to $A = 0.8\ \mathrm{cm}$ and its frequency becomes the main frequency of the oscillations. The observation of the first mode flutter becomes more difficult. At the highest reachable flow velocity, $U = 5.84\ \mathrm{m/s}$, the first mode instability is not present anymore and the pipe only exhibits a first mode buckling and a fifth mode oscillatory instability.

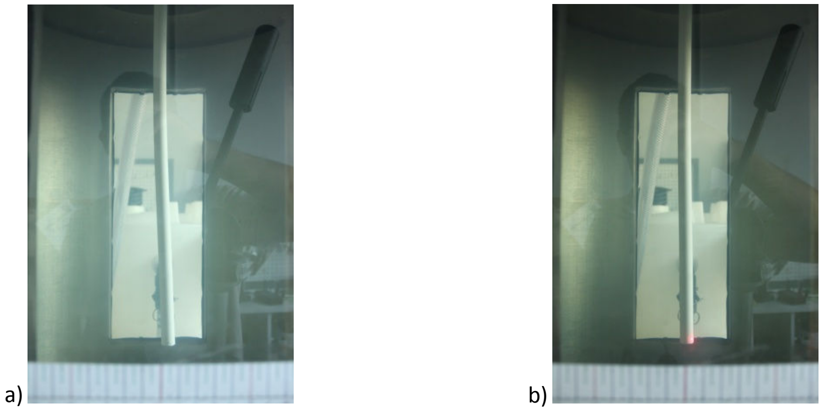
a) b)

Figure 3.22: View of the pipe at a) $\boldsymbol{U = 0\ \mathrm{m/s}}$ and b) $\boldsymbol{U = 3.13\ \mathrm{m/s}}$ showing the disappearing of the static bending (bowing)

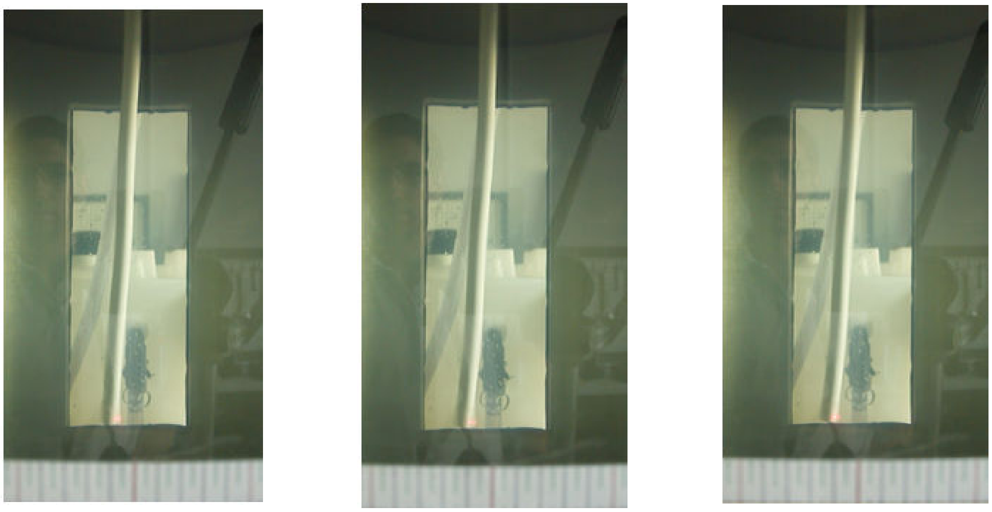

Figure 3.23: Superposition of the three observable instabilities at $\boldsymbol{U = 5.40\ \mathrm{m/s}}$ over half a period of the first mode oscillations

3.4.6 Configuration 3ii

The difference from the previous configuration is that the pipe motion is contained in an outer rigid tube whose length is half that of the pipe. At low flow velocity, this does not affect the dynamics of the pipe. As shown in Figure 3.25, the pipe is slightly bent at zero flow velocity but the bend then smoothly disappeared at $U = 2.83\ \mathrm{m/s}$. Then, at $U = 3.25\ \mathrm{m/s}$, a first mode flutter arises with a small amplitude and a frequency $f = 0.39\ \mathrm{Hz}$. As in Configuration 3i, periods of periodic motion alternate with periods of chaotic motion. As in Configuration 3i, the pipe also exhibits a first mode buckling instability but, here, this appears at $U = 3.51\ \mathrm{m/s}$. Its amplitude grows rather quickly.

Up to this point, the dynamics is very similar to that of Configuration 3i. But, as the amplitude of the buckling increases, the pipe comes closer to the plexiglas tube and finally touches it at $U = 4.06\ \mathrm{m/s}$. At this velocity, the amplitude of first mode flutter suddenly increases to $A = 0.7\ \mathrm{cm}$ and the frequency of oscillations to $f = 0.67\ \mathrm{Hz}$. Thus, contact with the outer tube has a great influence on the dynamics of the pipe. At higher flow velocities the amplitude of the buckling increases to reach $A = 1.8\ \mathrm{cm}$ at $U = 4.88\ \mathrm{m/s}$. The frequency of oscillations also increases up to $f = 0.85\ \mathrm{Hz}$ at $U = 5.03\ \mathrm{m/s}$.

Then, at $U = 5.21\ \mathrm{m/s}$, the dynamics of the pipe suddenly changes. Sometimes, it loses contact with the outer tube. As a result, the amplitude of the first mode flutter grows suddenly to $A = 1\ \mathrm{cm}$ and it continues to increase

Figure 3.24: The motion of Pipe 1 in Configuration 3ii at $U = 6.01\ \mathrm{m/s}$

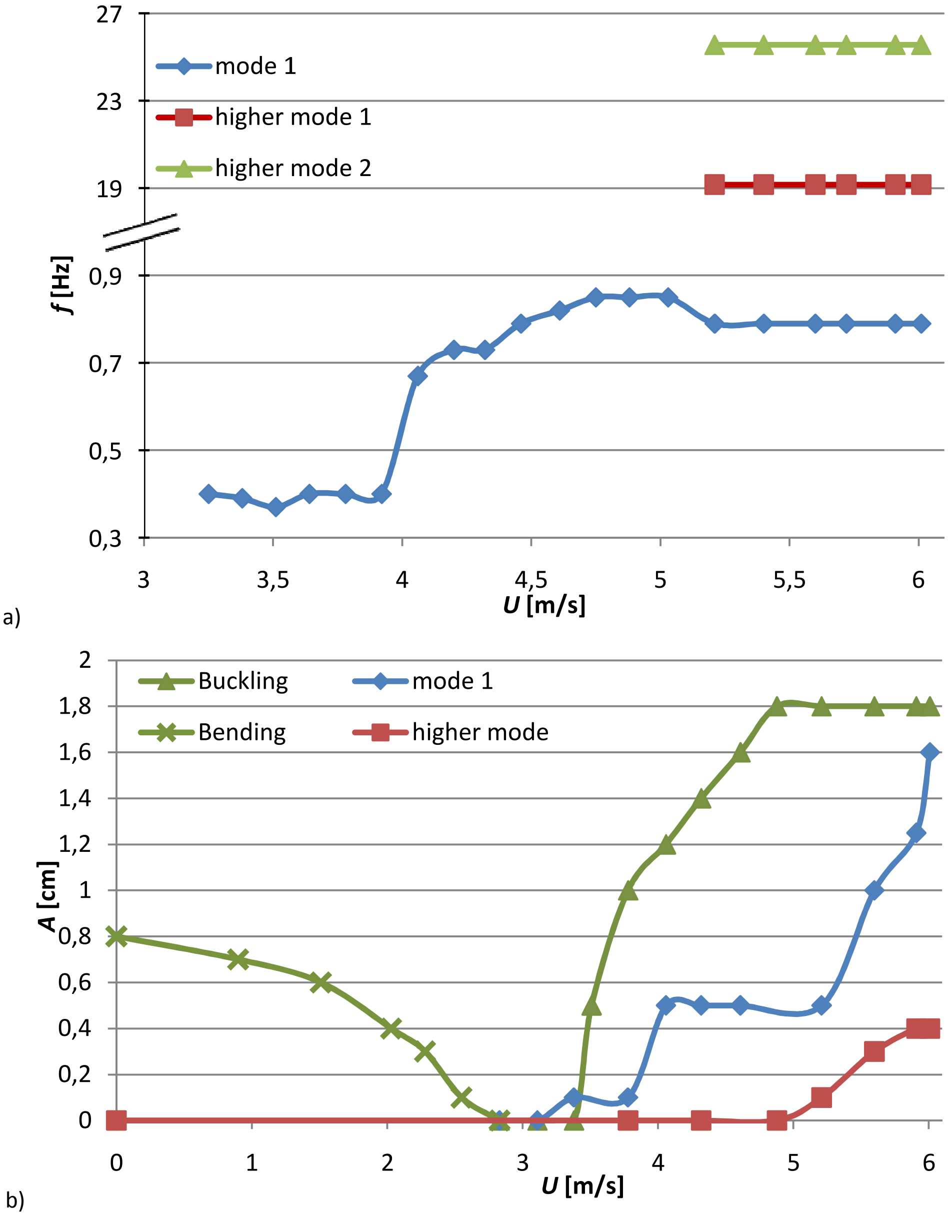

Figure 3.25: a) The experimental frequency and b) amplitude versus velocity with Pipe 1 in configuration 3ii

quickly at higher flow velocity. The frequency jumps down to $f = 0.79$ Hz, but does not change anymore thereafter. However, the most important thing is that the pipe also exhibits higher mode oscillations when it is not in contact with the outer tube (Figure 3.24). It is difficult to determine the mode of the oscillations; they might be a combination of different modes because, in the power spectrum, two minor peaks appear at $f = 19.2\text{Hz}$ and $f = 27.2$ Hz. These frequencies remain the same during the experiment. The amplitude of these oscillations increases as the flow velocity increases and it reaches $A = 0.4\ \mathrm{cm}$ at the highest flow velocity.

3.4.7 Configuration 3iii

This is the same as the previous configuration, except that the outer tube is as long as the pipe. As in the other configurations involving a spring, there is a bending of the pipe at zero flow velocity. But, in this configuration, the outer tube has a stabilizing effect too, as the bending disappears at $U = 3.91\ \mathrm{m/s}$.

At $U = 4.04\ \mathrm{m/s}$, a first mode buckling appears. This is a transition velocity at which the pipe alternates between two positions: (i) the position of the pipe at lower flow velocity in which the pipe does not touch the outer tube and (ii) a first mode buckling instability in which the free end of the pipe is in contact with the free end of the plexiglas tube.

The pipe then exhibits a complex motion at $U = 4.20\ \mathrm{m/s}$. Its free end performs a cyclic motion. As shown Figure 3.26, at the beginning of the cycle, the pipe exhibits a first mode buckling instability and there is contact with the outer tube free end. The free end of the pipe then remains in contact with the outer tube but the point of contact moves; it travels all over half the circumference of the free end of the outer tube. The contact is finally broken and the pipe comes back to its initial position through the centre of the plexiglas tube.

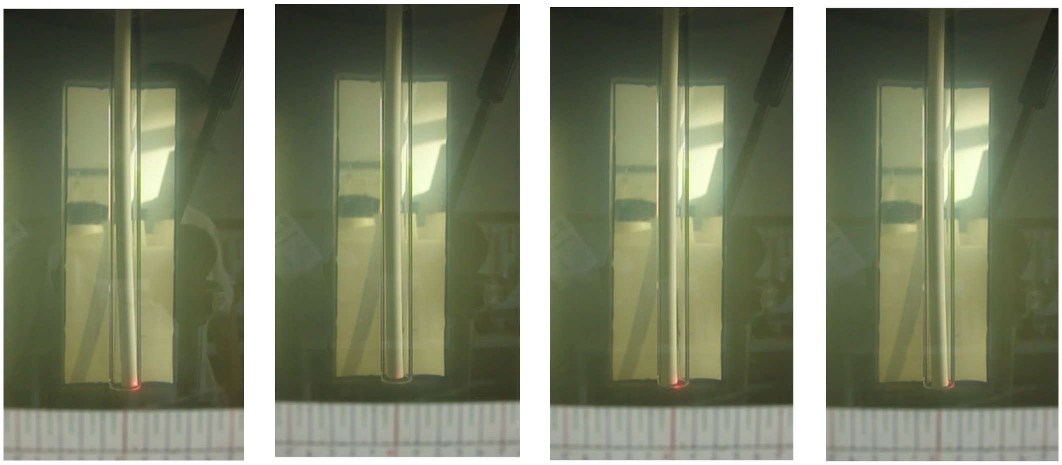

Figure 3.26: The cyclic motion of Pipe 1 in Configuration 3iii at $\boldsymbol{U = 4.20\ \mathrm{m/s}}$

The transition period ends at $U = 4.33\ \mathrm{m/s}$. Then, the pipe exhibits only a first mode buckling instability. As shown in Figure 3.27, approximately half of the pipe length touches the outer tube at this velocity. At higher flow velocity, the pipe gradually pulls away from the outer tube, beginning by the upper part. At $U = 5.95\ \mathrm{m}/s$, the highest reachable flow velocity, only the lower part of the pipe is still in contact with the outer tube.

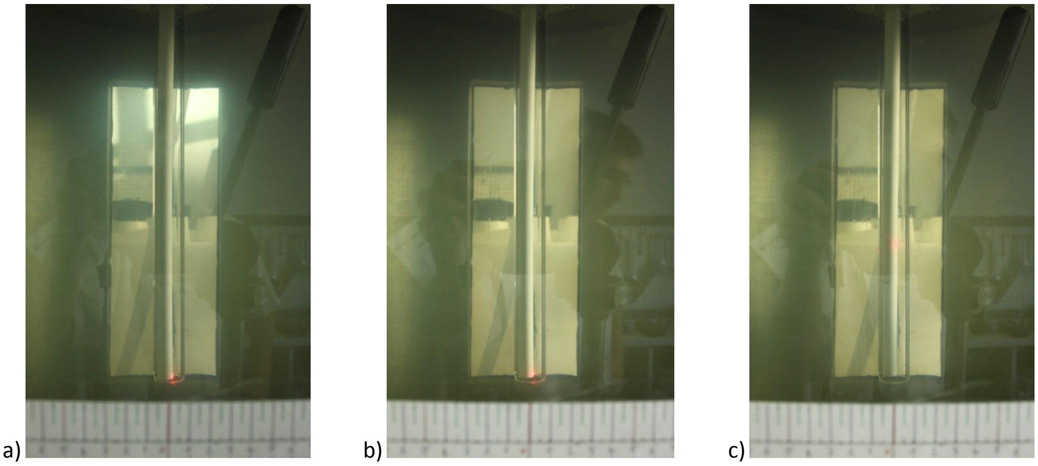

Figure 3.27: The first mode buckling of Pipe 1 in Configuration 3iii at a) $\boldsymbol{U = 4.33\ \mathrm{m/s}}$, b) $\boldsymbol{U = 5.53\ \mathrm{m/s}}$ and c) $\boldsymbol{U = 5.95\ \mathrm{m/s}}$

3.4.8 Configuration 4i

In that configuration, the flow velocity is that of the flow in the annular gap. At $U = 1.14\ \mathrm{m/s}$, a really weak instability arises. The amplitude is small ($A \approx 0.25\ \mathrm{cm}$) and there is absolutely no definite frequency in the signal. These small oscillations could be due to some imperfections inherent to the experiments. For example, there is a plate between the vessel and the tank. Some holes are drilled in it so that the water can go through and then flows in the annular gap; thus, the flow might not be homogeneous in the annular region. The small oscillations might also be due to some imperfections that can be present on the outside part of the pipe or to a Bernoulli phenomenon. If the tube comes only slightly closer to the outer tube, then the velocity is locally increased and this can produce a local pressure reduction. Each of these reasons might cause these small and non-periodic oscillations. At $U = 2.88\ \mathrm{m/s}$, an instability arises (Figure 3.28). It is not always observable. In fact, periods of periodic oscillations alternate with periods of quasi-chaotic motion of smaller amplitude. The frequency of oscillation is $f = 4.8\ \mathrm{Hz}$ and the amplitude is increased to $A = 1.3\ \mathrm{cm}$. Both second and third modes are present in the pipe motion. From this velocity to $U = 3.84\ \mathrm{m/s}$, the highest reachable, the frequency of oscillations does not change a lot and it remains around $f = 5\ \mathrm{Hz}$. The amplitude first increases to reach $A = 3.5\ \mathrm{cm}$ at $U = 3.38\ \mathrm{m/s}$ before decreasing. Furthermore, it should be noted that the intervals of small chaotic motion become longer than the intervals of periodic motion as the velocity is increased. Thus, for $U = 3.84\ \mathrm{m/s}$, the periodic motions are hardly observable. It seems that, in this configuration, the pipe loses stability at $U = 3.07\ \mathrm{m/s}$ before regaining stability at a velocity higher than $U = 3.84\ \mathrm{m/s}$.

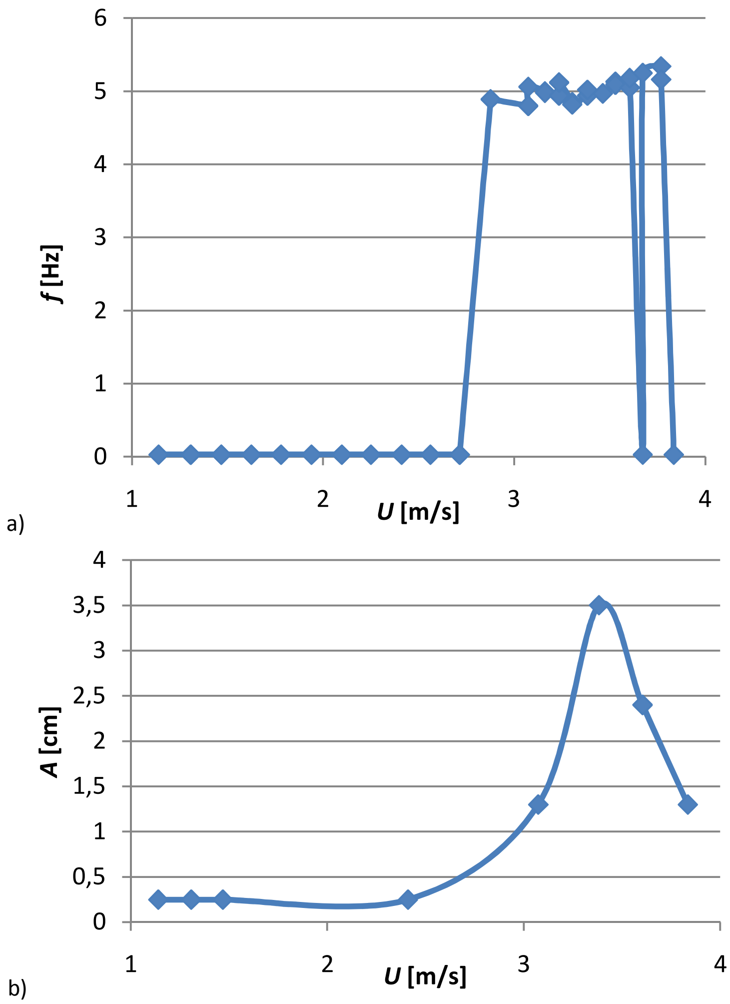

Figure 3.28: a) The experimental frequency and b) amplitude versus velocity with Pipe 1 in configuration 4i

3.4.9 Configuration 4ii

In this configuration, there is no observable instability. From $U = 1.38\ \mathrm{m/s}$, there are some really small oscillations but they are not periodic. For example, Figure 3.29 shows the time signal and the power spectrum obtained by Welch’s method and the FFT method. There is no discernible main frequency. These small perturbations can be due to the same reasons as in configuration 4i. As the free end of the pipe is blunt, the non-occurrence of instability was expected from the theory of a solitary clamped-free cylinder in axial flow.

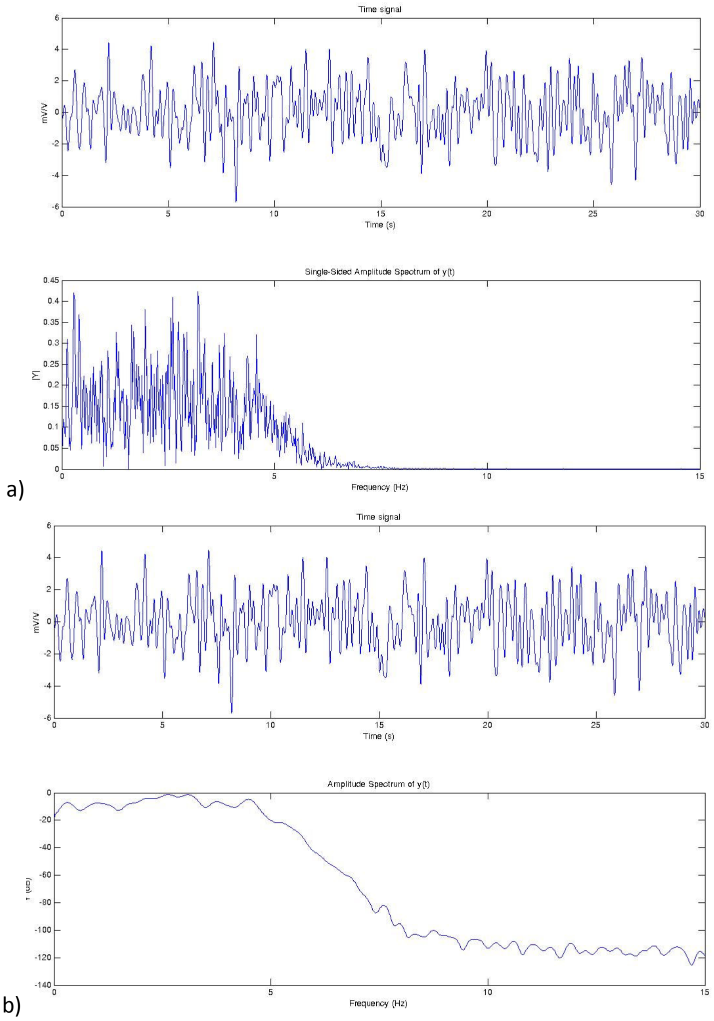

Figure 3.29: Power spectra obtained for pipe 1 in configuration 4ii at $\boldsymbol{U = 3.094\ \mathrm{m/s}}$ by a) the FFT method and b) Welch’s method

3.4.10 Configuration 5i

In this configuration, a first mode buckling instability arises at the first measurable flow velocity, $U = 0.10\ \mathrm{m/s}$. The amplitude is really small, $A = 0.1\ \mathrm{cm}$, but increases quickly. It reaches a maximum, $A = 0.8\ \mathrm{cm}$, at $U = 0.37\ \mathrm{m/s}$. At this velocity, the pipe is really close to the free end of the outer tube. Despite appearing to be in contact in Figure 3.30.a, water is actually flowing between the pipe and the outer tube even if the gap is really small. They remain not in contact until $U = 1.54\ \mathrm{m/s}$. However, the rest of the pipe gradually comes closer to the plexiglas tube (Figure 3.30.b). That is why the amplitude of the buckling that is measured at the free end of the pipe decreases for $U \geq 0.10\ \mathrm{m/s}$ and finally reaches a constant value, $A = 0.5\ \mathrm{cm}$.

At $U = 1.14\ \mathrm{m/s}$, another instability is overimposed on the buckling. The amplitude is first rather small, $A = 0.2\ \mathrm{cm}$. The motion of the pipe is rather complex. The pipe seems to be virtually separated into two parts: the upper part located in the plexiglas tube and the lower part in unconfined water. Only the lower part is subjected to the first mode flutter that arises at this velocity. For now, the upper part is only subjected to buckling.

At $U = 1.22\ \mathrm{m/s}$, a third mode flutter appears. Here, the whole pipe is subjected to this new instability and the point of the pipe close to the free end of the outer tube is a node for this mode. The frequency is always close to 5 Hz. The amplitude of both the first and third mode flutter first increases (Figure 3.31) to

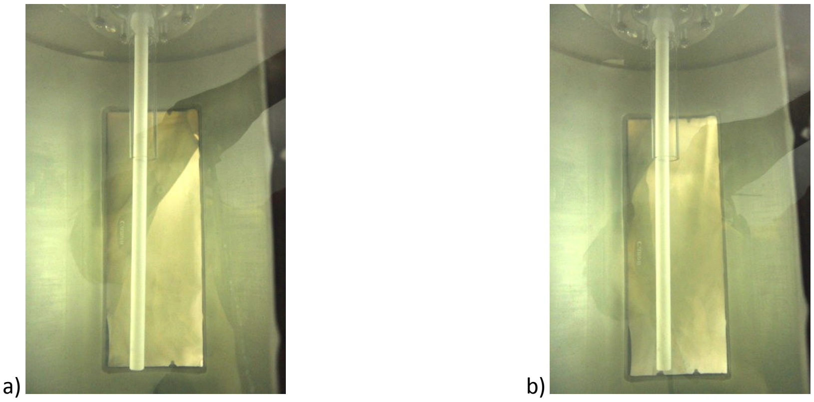

Figure 3.30: The buckling of the pipe at a) $U = 0.37\ \mathrm{m/s}$ and b) $U = 1.14\ \mathrm{m/s}$

reach a maximum at $U = 1.38\ \mathrm{m/s}$. It then decreases, certainly because a greater part of the pipe is close to the plexiglas: buckling works against flutter.

At $U = 1.54\ \mathrm{m/s}$, There is a sudden change in the buckling instability. The pipe is suddenly touching the free end of the outer tube, whereas the rest of the pipe moves away from it. From this velocity on, the amplitude of the two flutter modes increases again rather quickly. One might think that this sudden change would affect the dynamics of the pipe, but the two frequencies remain

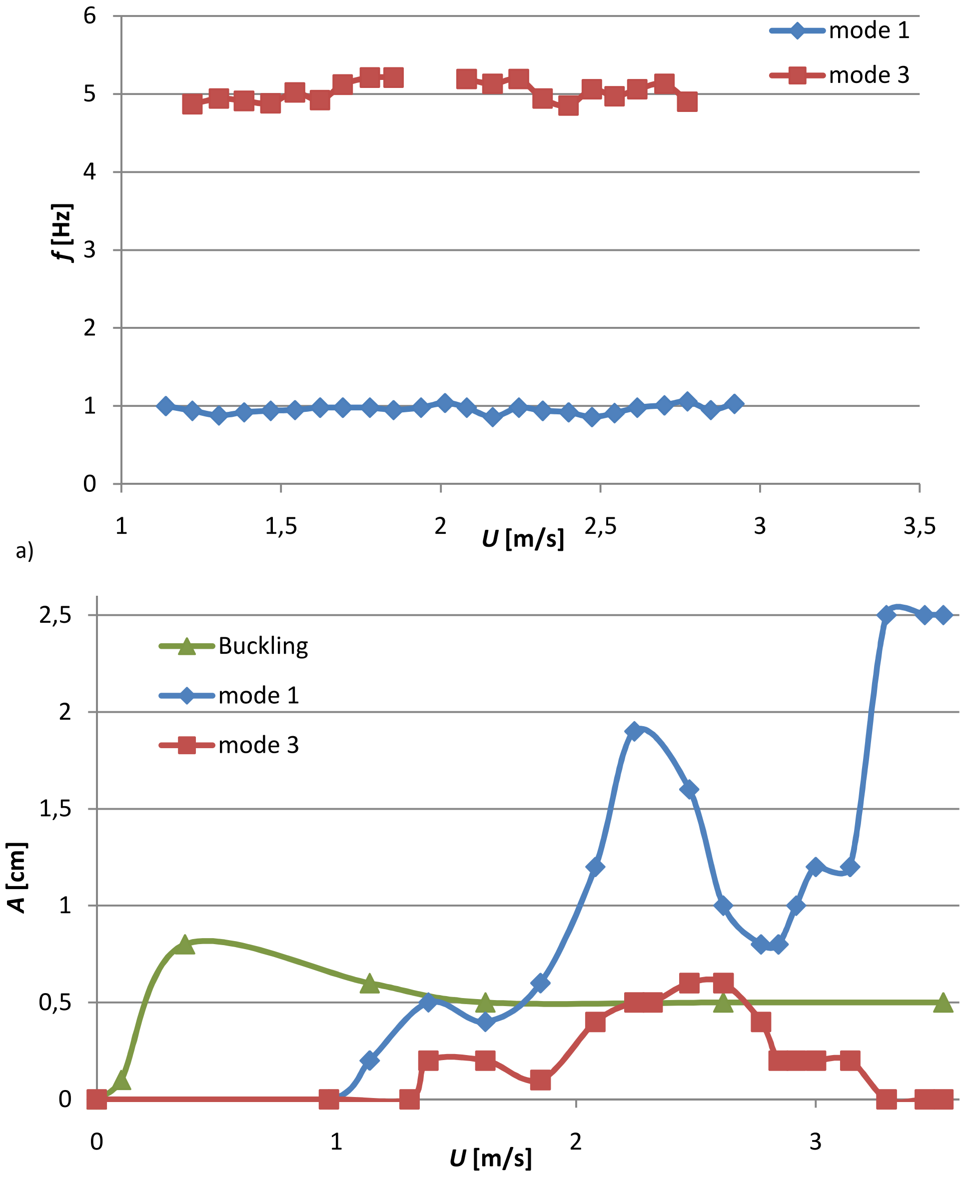

Figure 3.31: a) The experimental frequency and b) amplitude versus velocity with Pipe 1 in configuration 5i

the same. However, from this flow velocity on, the peak corresponding to third mode flutter is less sharp, not so high and rather wide. Because of the contact, the frequency of the third mode flutter seems to be close to $f = 5\ \mathrm{Hz}$ but might not be perfectly constant and, so, not very well defined. Furthermore, the pipe located in the plexiglas tube is gradually coming in contact with it as the velocity increases. All these different causes might explain why the third mode flutter exhibits no main frequency for $1.85 \leq U \leq 2.08$.

At $U = 2.08\ \mathrm{m/s}$, the previous behaviour seems to begin again. The pipe loses contact again with the outer tube except at the free end of the plexiglas tube. Here, this point of contact regularly changes. The third mode appears again and its amplitude suddenly increases. The amplitude of both modes goes through a maximum around $U = 2.4\ \mathrm{m/s}$. At higher flow velocity, once again, the pipe gradually comes into contact with the outer tube and the amplitude of both modes decreases again. Furthermore, the frequency of the third mode becomes less well defined, as in the previous step, and the motion of the third mode flutter becomes totally erratic at $U > 2.77\ \mathrm{m/s}$.

From $U = 2.85\ \mathrm{m/s}$ on, the pipe seems in the mood to lose contact with the outer tube. It suddenly moves a lot; the amplitude increases and, then, becomes smaller again. At $U = 3.00\ \mathrm{m/s}$, the pipe sometimes loses contact with the outer tube and suddenly touches it again. The behaviour is highly erratic and there is no main frequency. However, the amplitude of the motion increases.

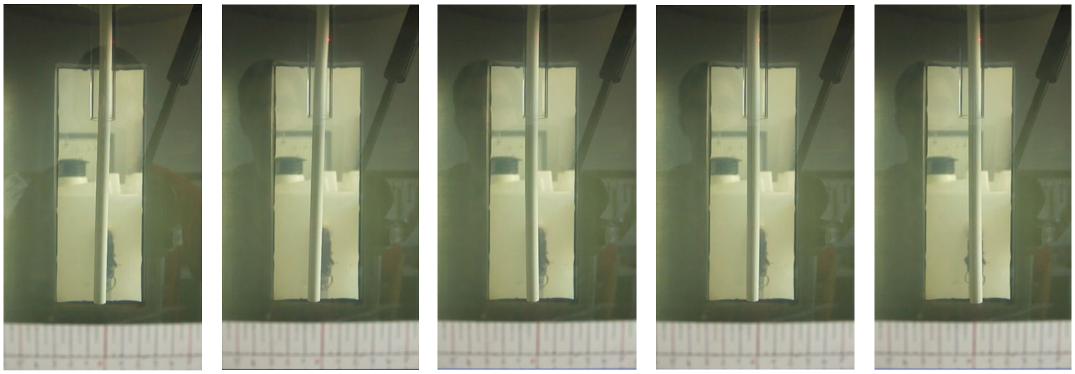

Figure 3.32: The complex behaviour of the pipe at $U = 3.53\ \mathrm{m/s}$ with the first mode buckling on the left and the flutter represented on the other pictures

The flow velocity $U = 3.30\ \mathrm{m}/s$ is a particular one. The point of contact between the pipe and the outer tube travels continuously all over the circumference of the free end of the outer tube with no frequency. Then, the pipe suddenly exhibits periodic planar motion for a few seconds ($f = 0.85\ \mathrm{Hz}$) and, finally, diverges. At higher flow velocities, the pipes exhibits alternately two different behaviours: a first mode buckling alternates with periods of flutter (Figure 3.32). When the pipe undergoes flutter, the oscillations impact the outer tube at each extreme of the motion but they have no frequency. Maybe it is not really flutter and it is a change of the position of buckling.

3.4.11 Configuration 5ii

As in Configuration 5i, in this configuration, an instability arises at the first measurable flow velocity, $U = 0.13\ \mathrm{m}/s$. The amplitude of this first mode buckling is $A = 0.3\ \mathrm{cm}$ (Figure 3.33). It increases until it reaches its maximum ($A = 0.5\ \mathrm{cm}$), determined by the presence of the outer tube, at $U = 0.42\ \mathrm{m/s}$. At this velocity only the free end of the pipe is touching the free end of the outer tube. At higher flow velocity, the rest of the pipe gradually comes in contact with the plexiglas tube. At $U = 0.89\ \mathrm{m/s}$ and at $U = 1.61\ \mathrm{m/s}$, respectively, half and three-quarters of the pipe is touching the plexiglas.

At $U = 1.38\ \mathrm{m}/s$, small vibrations of the pipe are observable but the amplitude is small and the frequency is $f = 1.70\ \mathrm{Hz}$. Furthermore, because the pipe is coming more and more in contact with the outer tube at the same time, periods of periodic motion alternate with periods in which the pipe has no definite frequency: buckling set against flutter. As a longer part of the pipe is in contact with the plexiglas tube, the periods with no definite frequency become longer. From $U = 2.00\ \mathrm{m/s}$, the opposite behaviour is observable and a smaller part of the pipe is in contact with the outer tube. Until this point, the frequency and the amplitude of oscillation slightly increased. Both suddenly increase at $U = 2.00\ \mathrm{m/s}$.

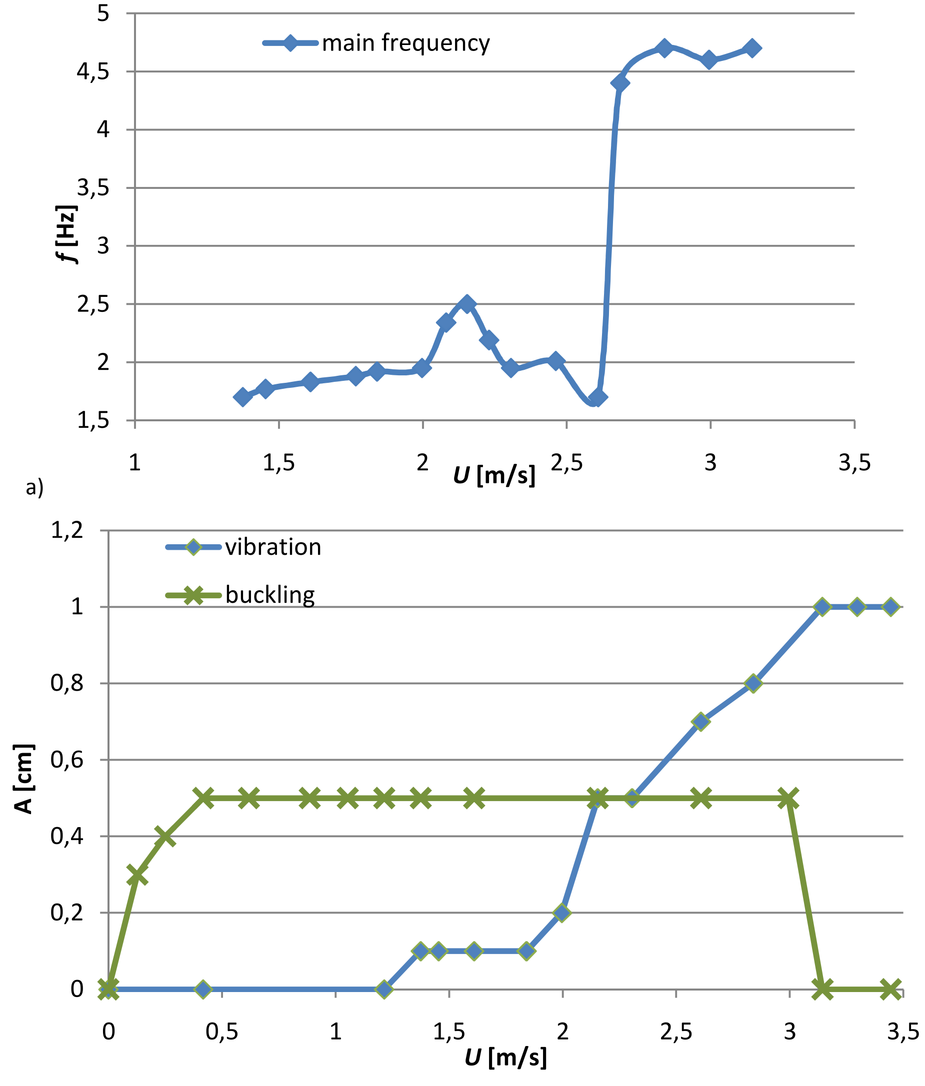

Figure 3.33: a) The experimental frequency and b) amplitude versus velocity with Pipe 1 in configuration 5ii

For $2.00 \leq U < 2.69$, the pipe seems to alternate between two configurations: a second mode buckling and a third mode buckling. Sometimes, even the first mode is observable (Figure 3.34). In fact, only the free end of the pipe is always in contact with the outer tube whereas the rest of the pipe alternates between contact and non-contact. The frequency goes through a maximum at $U = 2.15\ \mathrm{m/s}$. It then decreases to $f = 1.70\ \mathrm{Hz}$ at $U = 2.61\ \mathrm{m/s}$.

At $U = 2.69\ \mathrm{m/s}$, the power spectrum exhibits no peak around 2 Hz but a new one appears at $f = 4.24\ \mathrm{Hz}$. The pipe seems to exhibit vibrations in its third mode. The plane of oscillations changes constantly. At $U = 2.84\ \mathrm{m/s}$, the free end of the pipe travels continuously all over the circumference of the free end of the outer tube. At $U = 3.14\ \mathrm{m/s}$, the amplitude of oscillations reaches its maximum possible magnitude and the end of the pipe suddenly loses contact with the outer tube. There is no more buckling and the whole pipe is now oscillating, but there is no main frequency at all. At higher flow velocities, the pipe exhibits an erratic behaviour whose amplitude is limited by the presence of the plexiglas tube.

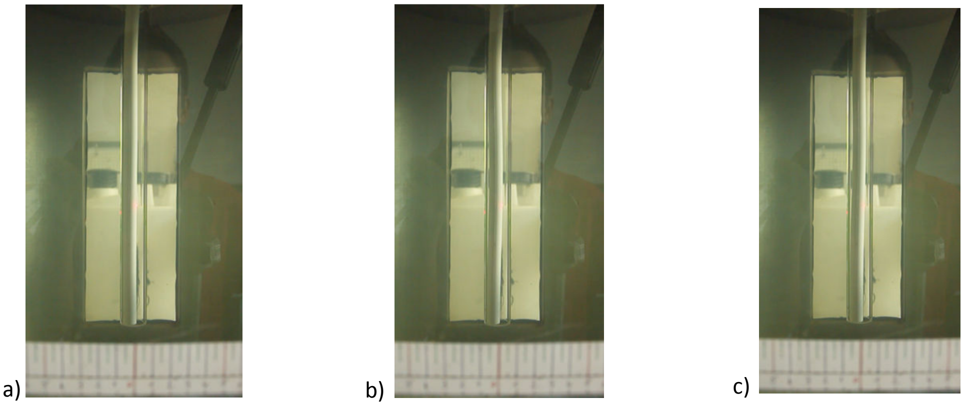

Figure 3.34: The a) first, b) third and c) second mode buckling successively observable at $\boldsymbol{U = 2.61\ \mathrm{m/s}}$

3.4.12 Configuration 6i

At the beginning, the pipe is very stable. The combination of the flow in the pipe from the top to the free end and a counter-current flow in the annular space has a stabilizing effect on the pipe (Figure 3.35.a). But, rather quickly, buckling in the first mode is experienced. At $U = 1.93\ \mathrm{m/s}$, the pipe touches the outer tube at its free end (Figure 3.35.b). It then remains the same until $U = 5.35\ \mathrm{m/s}$ when really small non-periodic oscillations of the pipe appear. This continues only over a brief interval. At $U = 5.59\ \mathrm{m/s}$, the pipe is still in contact with the free end of the plexiglas tube but begins to flutter in its second mode. This corresponds to the first increase of the amplitude in Figure 3.37. The frequency is $f = 3.20\ \mathrm{Hz}$ at the critical flow velocity and it begins to decrease, reaching $f = 2.99\ \mathrm{Hz}$ at $U = 5.82\ \mathrm{m/s}$ before increasing again to $f = 4.08\ \mathrm{Hz}$ at $U = 6.94\ \mathrm{m/s}$. Meanwhile, the amplitude remains the same to $U = 6.28\ \mathrm{m/s}$ ($A = 3.2\ \mathrm{cm}$) before decreasing to $A = 1.2\ \mathrm{cm}$.

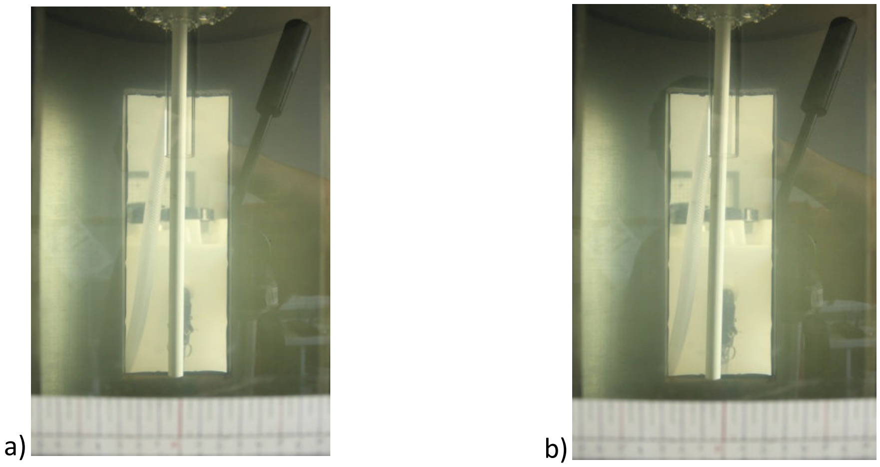

Figure 3.35: Pipe 1 in configuration 6i at a) $\boldsymbol{U = 1.37\ \mathrm{m/s}}$ and b) $\boldsymbol{U = 1.93\ \mathrm{m/s}}$

At $U \geq 6.94\ \mathrm{m/s}$, the dynamics of the pipe seems to change. The motion of the pipe gives the impression that the pipe behaves as if it was separated in two parts: one located in the outer tube and the other in unconfined flow. Even if the oscillations of both parts have the same frequency, it seems that the lower part is in the mood to flutter and the upper one to diverge. The pipe does not touch the plexiglas tube only in one point; it is rather a part of the pipe that is in contact with the outer tube. The contact line is around 3 cm long. The dynamics of the pipe is the result of a combination of these two effects. This might explain the decrease of the oscillation amplitude.

At $U = 7.23\ \mathrm{m/s}$, the dynamics of the pipe changes suddenly. The upper part seems to want to diverge in the second mode, so that the general motion of the pipe is flutter in the third mode. Figure 3.36 shows the shape of the pipe at different instants at $U = 7.68\ \mathrm{m/s}$. From $U = 7.42\ \mathrm{m/s}$, the motion of the pipe is more complex: sometimes in a plane, sometimes the free end performs a figure-of-eight oscillation, and sometimes it appears to be chaotic. The interaction between the possible buckling of the upper part and the flutter of the lower part might explain the complex behaviour. This kind of motion is observable until $U = 7.91\ \mathrm{m/s}$. Meanwhile, the amplitude of oscillation increased again to $A = 6.40\ \mathrm{cm}$ and the frequency decreased to $f = 2.26\ \mathrm{Hz}$.

Figure 3.36: Pipe 1 in configuration 6i at $U = 7.68\ \mathrm{m/s}$ at different instants

At $U = 7.91\ \mathrm{m/s}$, as the frequency goes through a minimum, the dynamics of the pipe changes again. The whole pipe begins to move again. There is no more perpetual contact between the flexible and outer tubes and there is no buckling anymore. The motion of the pipe alternates between planar oscillations in the third mode and circular motion. The amplitude is abruptly increased to $A = 26\ \mathrm{cm}$, but it then increases further more slowly. The frequency also increases to $f = 3.54\ \mathrm{Hz}$ at $U = 9.31\ \mathrm{m/s}$. A comparison with configuration 2ii shows that the pipe has the same behaviour in this configuration. For example, at $U \approx 8.15\ \mathrm{m/s}$, the pipe oscillates in its third mode, the amplitude of motion is $A = 24\ \mathrm{cm}$ and $A = 28\ \mathrm{cm}$, respectively, in configurations 2ii and 6i, and the frequency is $f = 3.05\ \mathrm{Hz}$ and $f = 2.44\ \mathrm{Hz}$, respectively, in configurations 2ii and 6i.

To conclude, the presence of the outer counter-current flow has a lot of influence on the dynamics of the system in comparison with configuration 2ii. First at relatively low flow velocity, the pipe diverges in its first mode. It then keeps the buckling shape and flutters close to this equilibrium position but at a higher flow velocity than in configuration 2ii. Subsequently, it undergoes a complex motion due to the virtual separation of the pipe into two parts, with the upper part close to buckling and the lower to flutter. However, at higher flow velocity, the influence of the annular flow seems to die out and the dynamics of the pipe is the same as in configuration 2ii.

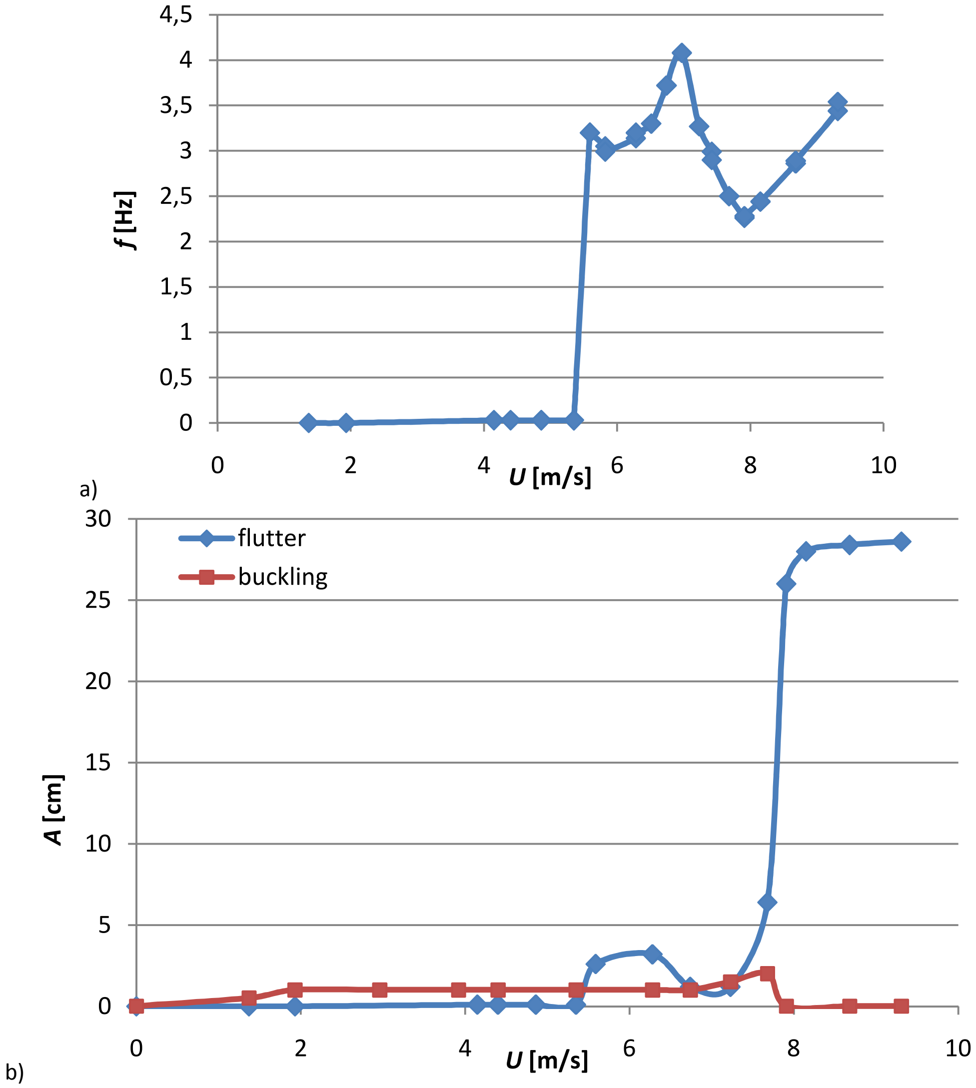

Figure 3.37: a) The experimental frequency and b) amplitude versus velocity with Pipe 1 in configuration 6i

3.4.13 Configuration 6ii

As in Configuration 2iii involving only a discharging pipe, a first mode buckling arises at $U = 1\ \mathrm{m/s}$ (Figure 3.39.a). The amplitude is very small but increases with flow velocity, and the free end of the pipe finally touches the free end of the outer tube at $U = 1.61\ \mathrm{m/s}$. The two remain in contact until the end of the experiment. Also, as in configuration 2iii, a greater part of the pipe is in contact with the outer tube as the velocity increases, and the opposite behaviour is observable for $2.60 \leq U \leq 3.14$. At this velocity, $U = 3.14\ \mathrm{m/s}$, only the free end of the pipe is touching the plexiglas tube. This is a particular velocity as the pipe suddenly exhibits a periodic motion with a frequency $f = 1.20\ \mathrm{Hz}$ that immediately dies out as the flow velocity increases (Figure 3.38). The pipe then demonstrates a second mode buckling. Thus, this particular velocity marks the transition from first mode buckling to second mode buckling.

Up to $U = 4.56\ \mathrm{m/s}$, the pipe displays a second mode buckling (Figure 3.39.b) but also very small vibrations with no dominant frequency. They might be due to the same reasons as those presented in Configuration 4i.

For $4.56 \leq U \leq 6.88$, the dynamics of the pipe go through a period of transition from second mode buckling to third mode buckling. Over this range, the pipe exhibits a complex behaviour: periods of chaotic motion alternate with periods of oscillatory divergence. Both second mode buckling and third mode buckling are alternately observable, the pipe switching from one to the other. For some velocities as $U = 5.26\ \mathrm{m/s}$, the motion of the pipe is almost entirely erratic and there is no definite frequency. But, as the velocity increases, the third mode is more and more present and finally, at $U = 6.17\ \mathrm{m/s}$, only the instability in the third mode is observed.

At $U = 6.88\ \mathrm{m/s}$, the oscillatory divergence is not observable anymore and the pipe exhibits a third mode buckling (Figure 3.39.c). It remains in this position until $U = 9.44\ \mathrm{m/s}$. At this velocity, the pipe suddenly exhibits a fourth mode buckling (Figure 3.39.d) without any interval of transition.

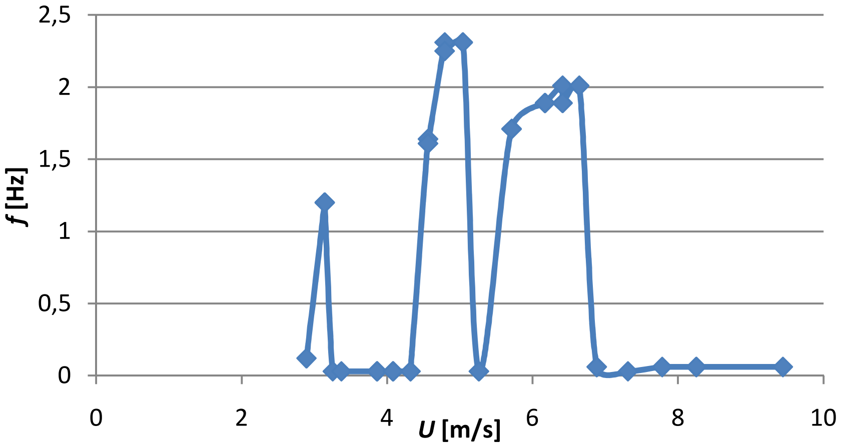

Figure 3.38: The experimental frequency versus velocity with Pipe 1 in configuration 6ii

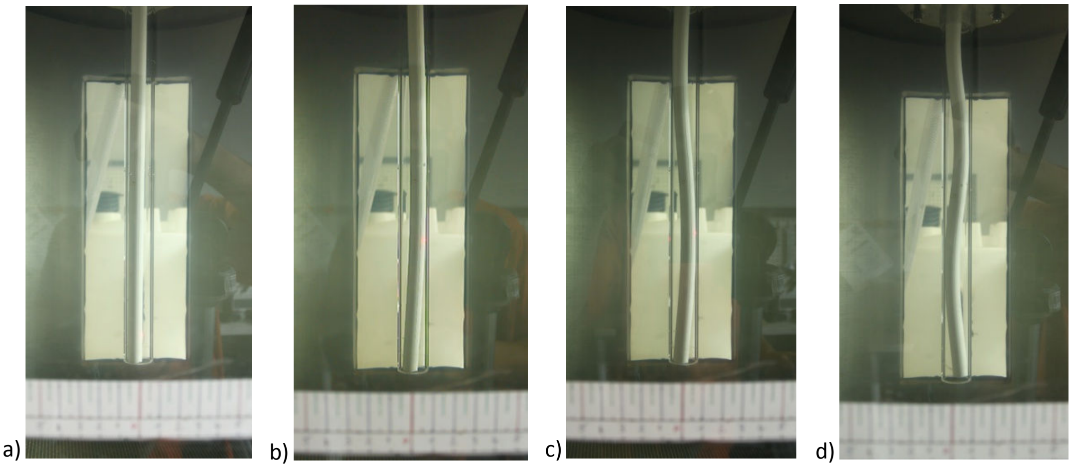

Figure 3.39: the a) first, b) second, c) third and d) fourth mode observed successively with Pipe 1 in Configuration 6ii

3.4.14 Configuration 7i

In this configuration again, a spring is inserted in the pipe because the pipe is aspirating fluid. Thus, the pipe is slightly bent at zero flow velocity. As in configuration 3ii, the amplitude is 0.8 cm. It then smoothly decreases with increasing flow velocity and disappears at $U = 1.34 \text{ m/s}$. So, because of the discharging annular flow, the bending dies out much more quickly than in configuration 3ii.

In this configuration, the pipe loses stability by flutter in its first mode at really low flow velocity. Hence, the first oscillations arise at $U = 0.37 \text{ m/s}$ with a frequency $f = 0.45 \text{ Hz}$. In this configuration also, the pipe does not exhibit continuous periodic motions. The periodic motion alternates with chaotic motion. At first, periods of chaotic motion are hardly observable. Furthermore, the amplitude is really small, $A = 0.2 \text{ cm}$, but increases quite rapidly to $A = 2.5 \text{ cm}$ at $U = 1.85 \text{ m/s}$. At this velocity, the pipe impacts the free end of the plexiglas tube for the first time. This contact has a great influence on the dynamics of the pipe. From that point, the frequency will always increase. For $1.85 \leq U < 2.90$, the amplitude remains constant. Furthermore, periods of shuddering motion are really long and periods of periodic motion do not last more than a few seconds. This is because the collision with the plexiglas disturbs the dynamics of the pipe

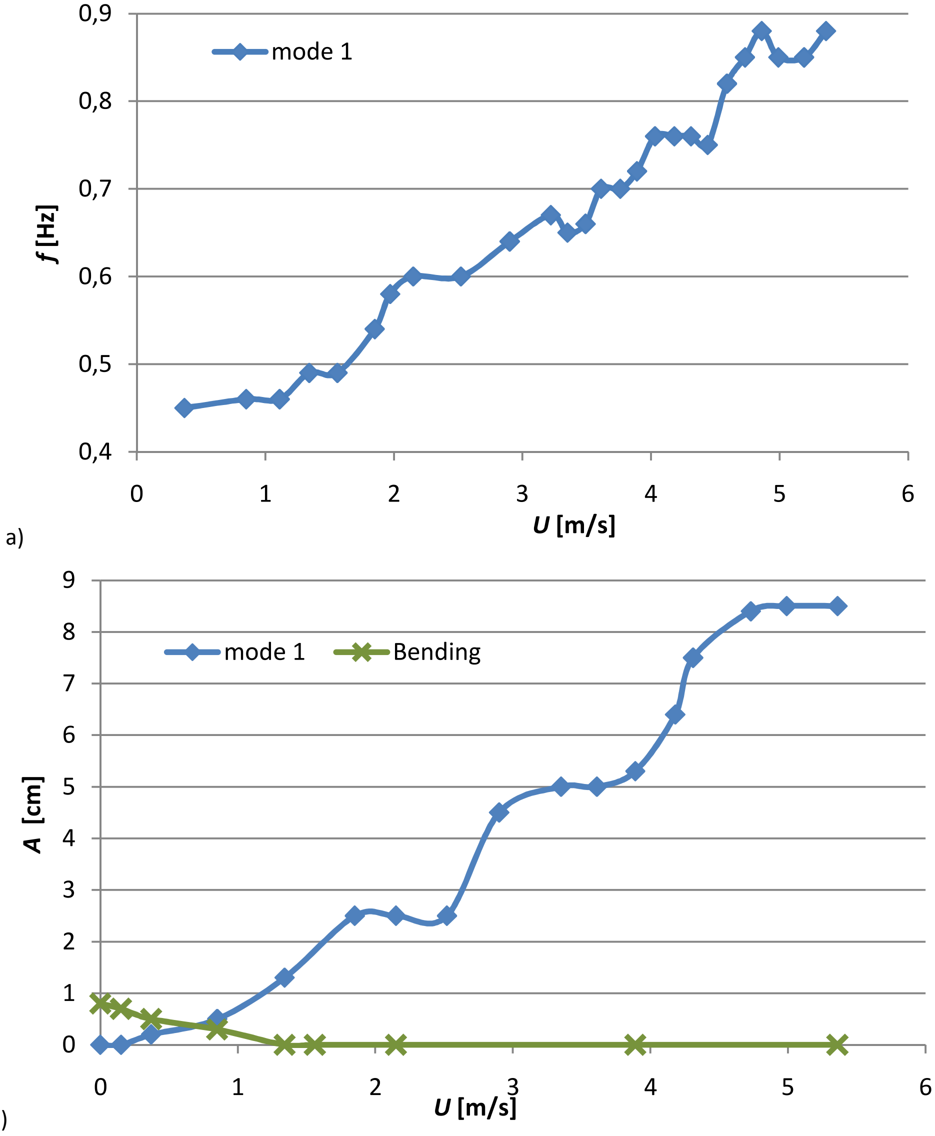

Figure 3.40: a) The experimental frequency and b) amplitude versus velocity with Pipe 1 in configuration 7i

that exhibits periodic motion of small amplitude. The amplitude then increases until the pipe touches the plexiglas. A period of chaotic motion follows and the cycle begins again.

From $U = 2.90\ \mathrm{m/s}$ and to the highest reachable flow velocity, the amplitude increases again rather quickly, from $A = 4.5\ \mathrm{cm}$ to $A = 8.5\ \mathrm{cm}$, and the frequency increases continuously from $f = 0.64\ \mathrm{Hz}$ to $f = 0.88\ \mathrm{Hz}$ (Figure 3.40). The pipe exhibits mainly intervals of periodic motion. However, the motion is still complex, as two kinds of periodic motion alternate: periods of first mode planar motion and phases during which the end of the pipe performs figure-of-eight motion.

3.4.15 Configuration 7ii

In this configuration also, there is a bend of the pipe at low flow velocities. Here, it is limited by the outer rigid tube whose length is equal to half that of the pipe. As in configuration 7i, the bend disappears rather quickly because of the discharging annular flow.

In this last configuration, the first oscillatory instability arises at $U = 2.02\ \mathrm{m/s}$. The amplitude is so small that it is really difficult to observe, but the frequency which is that of the first mode flutter is $f = 1.1\ \mathrm{Hz}$. It is not steady and periods of chaotic motions also occur. As the flow velocity increases, the frequency and the amplitude do the same (Figure 3.43) and periods of periodic motion last longer and longer.

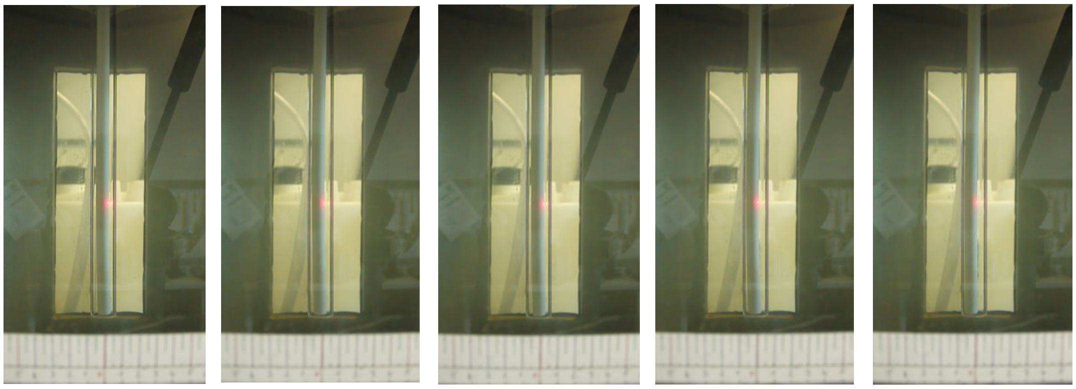

Figure 3.41: The complex behaviour of the pipe at $U = 5.26\ \mathrm{m/s}$

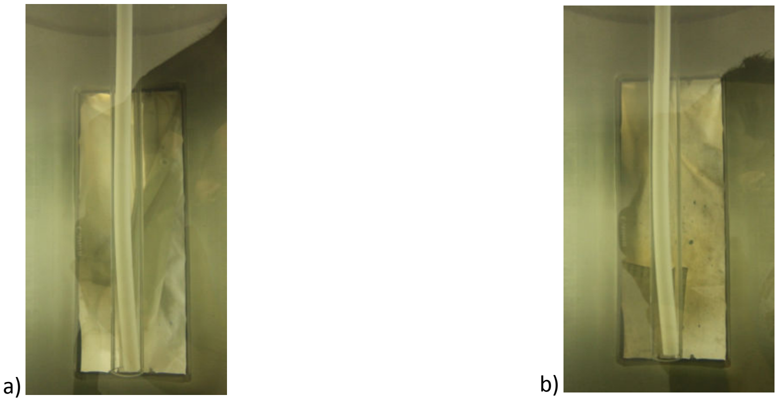

a) b)

Figure 3.42: The final second mode buckling of the pipe at a) $U = 5.26\ \mathrm{m/s}$ and b) $U = 5.56\ \mathrm{m/s}$.

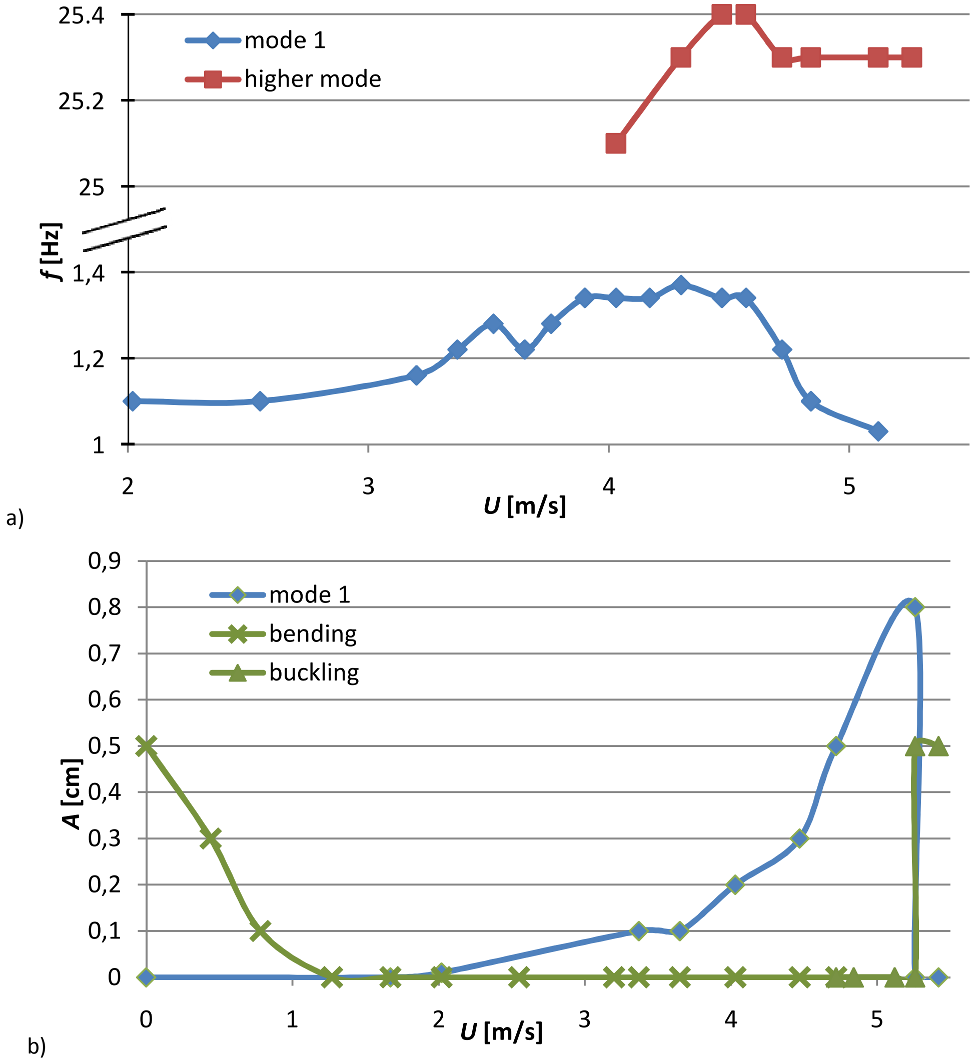

Figure 3.43: a) The experimental frequency and b) amplitude versus velocity with Pipe 1 in configuration 7ii

From $U = 4.03\ \mathrm{m/s}$, the amplitude increases more quickly, whereas it seems that the frequency has reached a plateau around $f = 1.34\ \mathrm{Hz}$. At this velocity, a minor peak appears in the power spectra. It is quite difficult to detect it by the naked eye because the amplitude of these oscillations is less than a millimetre and, so, it is hard to determine the mode of instability. The frequency of these higher mode oscillations is $U = 25.1\ \mathrm{m/s}$. They first increase with the flow velocity before reaching a maximum at $U = 4.54\ \mathrm{m/s}$. From this velocity to $U = 5.26\ \mathrm{m/s}$, both the frequency of the first mode and the frequency of the higher mode decrease. At $U = 5.26\ \mathrm{m/s}$, the amplitude of oscillations reaches a maximum ($A = 0.8\ \mathrm{cm}$). In fact, the pipe exhibits a complex motion: it is mainly oscillating but it sometimes remains in contact for a short time with the outer tube as if it was diverging (Figure 3.41). As shown in Figure 3.42, the pipe suddenly exhibits a second mode buckling at the same velocity. At higher flow velocity, the dynamics of the pipe does not change.

3.5 Conclusion

This project is divided into two quite distinct parts. As presented in Sections 3.2 and 3.3, a new apparatus had to be designed and built to experimentally study the dynamics of the hanging pipes used in salt caverns. Some problems and difficulties had to be overcome to finally get a useful apparatus allowing the study of a large set of configurations. There is a great variety of requirements. The apparatus has to recreate the environment of a salt cavern. It means that the pipe can be completely surrounded by water, which is the experimental fluid, but the sealing of the apparatus still has to be ensured. Furthermore, the two coaxial flows have to be separated, with no connection between them. A special part was designed to ensure this: the vessel sitting on top of the tank. It was really important to switch from one configuration to another quite quickly and easily. Moreover, different instrumentation had to be added to record the flow velocity and the amplitude as well as the frequency of pipe motion.

The second step of this project was to conduct a whole set of experiments with Pipe 1. The results are presented in Section 3.4. The major difficulty that was encountered was a shell-type collapse of the pipe in the configuration involving an aspirating pipe. It was decided to add a spring inside the pipe so that the collapse would be avoided, yet the motion of the pipe would not be constrained in any way. The insertion of the spring generated a small bend in the pipe; it was reduced by annealing the spring, but not entirely removed. However, with flow, this bow gradually disappeared, and in any case the real full-scale system is probably not 100% straight either.

Table 3.5: Comparison of the different critical flow velocities and flow rates

Configuration	Critical flow velocity for Flutter (m/s)	Corresponding flow rate (l/s)	Critical flow velocity for Buckling (m/s)	Corresponding flow rate (l/s)
1	6.94	0.476	-	-
2i	3.93	0.270	-	-
2ii	4.21	0.289	-	-
2iii	-	-	1	0.0686
3i	3.39	0.233	4.19	0.287
3ii	3.25	0.223	3.51	0.241
3iii	-	-	4.04	0.277
4i	3.07	0.946	-	-
4ii	-	-	-	-
5i	1.14	0.357	0.10 (first observable velocity)	0.031
5ii	1.21	0.372	0.123 (first observable velocity)	0.040
6i	5.59	0.383	1.93	0.132
6ii	4.56	0.313	1	0.0686
7i	0.37	0.0254	-	-
7ii	2.02	0.139	5.30	0.364

Table 3.5 presents a comparison of the critical flow velocities of the system in each configuration. If they exist, the onsets of buckling and flutter are presented separately. Furthermore, depending on the configuration, the

measured velocity was either the flow velocity in the pipe or in the annular flow. For reasons of comparison, the corresponding flow rates are also given in this table. On one hand, it appears from this table that the less stable configurations are Configuration 5i and Configuration 5ii as a buckling instability is observable from the very first reachable velocity. In these configurations, the flow is only in the annular gap and goes from the free end to the clamped end. On the other hand, the most stable one is Configuration 4ii as the pipe exhibited no instability in the experiment. Thus, it appears that, whereas the annular flow has a stabilizing effect when it is discharging water, it has the opposite effect when itis going the reverse way. And, it seems that this system should never be used with only an annular flow going from the free end to the clamped end.

The first general observation that can be made is that the surrounding water clearly has a destabilizing effect on the system. The critical flow velocity in Configuration 2i or Configuration 2ii is smaller than in Configuration 1. Then, for systems involving a discharging pipe, the amplitude of motion can easily be larger than twenty centimetres if the outer tube does not have the same length as the pipe. If the pipe is aspirating the fluid, the amplitude is rarely higher than three centimetres, except for Configuration 7i in which the amplitude reaches $A = 8.5\ \mathrm{cm}$. But it is still much smaller than for the cases of a pipe discharging water. Nevertheless, it is important to point out that the maximum experimental velocities are higher when the pipe is discharging water. In that case, the maximum velocity is higher than $8\ \mathrm{m/s}$, whereas $U_{max} < 6\ \mathrm{m/s}$ when the pipe is aspirating fluid.

Moreover, by comparing the critical flow velocities for Configuration 2ii and Configuration 6i, it is difficult to say if the addition of the counter-current annular flow has a beneficial effect. Although the system certainly loses stability by buckling at a lower flow velocity in terms of flutter the system is more stable. In contrast, the comparison of the critical flow velocities of Configuration 3ii, Configuration 4i and Configuration 7i shows that the combination of both flows clearly has a destabilizing effect on the system. This study also shows that for salt mining, storage or withdrawal of the liquid hydrocarbons and natural gas purposes, Configuration 6i should be used as often as possible because the system is much more stable than in configuration 7i.

Furthermore, even if the type of instability, the critical flow velocity and the behaviour of the pipe at higher flow velocities depend on the configuration, some similarities exist. A good example is the comparison of the dynamics of the pipe in Configuration 2ii and Configuration 6i. At low flow velocities, the pipe has the same dynamics in both configurations. The behaviour then differ from one configuration to the other. However, at high flow velocities, the pipe exhibits again the same behaviour in both configurations; at these velocities, the dynamics of the system is dominated by the inner flow in Configuration 6i.

Finally, as explained in Section 3.3, the apparatus was also designed to conduct experiments with another pipe, other outer tubes and also additional rings. In the future, it might be really useful to redo the whole set of experiments presented in Section 3.4 together with these new equipments in which the outer tube size is varied, the effect of a ring is assessed, etc. Indeed, the present results could be compared with other sets of results. Thus, the influence of an additional ring, of the width of the annular gap and of the pipe thickness could be investigated and, the observations and conclusions presented in the present work could be fine-tuned.

Chapter 4: Conclusion

As discussed in Chapter 1, a lot of researchers have been intrigued by the dynamics of a pipe conveying fluid over the past few decades. The dynamics of quite different systems involving thin and thick flexible pipes subjected to internal, external, annular, or both internal and external axial flow has been investigated over the years. If the work in this area has often been curiosity-driven, it is now certain that it is of both fundamental and practical interest, as industrial applications have emerged years after the study has been carried out.

As a matter of fact, whereas the work presented in Chapter 2 is of fundamental interest, the experimental study undertaken in Chapter 3 is directly inspired by industrial problems and the results are expected with great interest by companies who store hydrocarbons and natural gas in salt caverns. Nevertheless, the study presented in Chapter 2 is also motivated by possible applications in existing industrial installations involving cantilevered shells aspirating fluid for ship-board liquefaction of natural gas, as well as by experimental observations made by Rinaldi (2009) at McGill University, Montreal, Canada.

So, the scope of the present work can be divided into two main issues: (i) the investigation of the dynamics of a thin-walled pipe, i.e. a cylindrical shell, aspirating air, and (ii) the experimental study of the stability of a thick-walled pipe subjected to internal, annular, or simultaneous internal and annular axial flows.

In Chapter 2, the dynamical investigation of an aspirating cantilevered shell is conducted both theoretically and experimentally. First, a linear analytical model is developed. Once the model assumptions have been defined, the equations of motion are derived through a variational principle and by taking into account new boundary conditions associated with the fluid flowing from the free towards clamped end. Indeed, as the flow is not a reverse jet in the case of an aspirating cantilevered shell, there is a change of momentum of the flow at the inlet, and the corresponding force acting at the free end of the shell has to be considered in the equations. The pressure difference at the wall is determined with a Fourier-Transform Generalized-Force method, also taking into account an out-flow model. A solution of the problem is finally found by using the extended form of the Galerkin method. The second step of the investigation is to conduct experiments with two different flexible shells that are made of the same material but whose length and wall thickness differs. They have been conducted in an existing apparatus involving air as flowing fluid. Finally, the theoretical and experimental results are compared. Whereas the theory is able to predict qualitatively the first type of instability, which is a first mode flutter, the critical flow velocities are overestimated by the theory. Furthermore, whereas the analytical model predicts buckling at higher flow velocities, in the experiments buckling arises at the same flow velocity as flutter. So, at the end of this work, it is not sure yet if the phenomenon observed in the experiments is flutter followed by buckling, or if it is an "oscillatory buckling", involving the frequent switch from one possible buckling state to another. In the latter case, the final buckling would be the final state of this phenomenon. However, the collapse of the shell could also be due to the combination of the intramural pressure difference at the wall and of the really low stiffness of the material.

The experimental study of the stability of the hanging tubular pipes used in salt caverns has been undertaken as a first step to better understand the failures that were observed in industrial installations. The experiments were first meant to be conducted with a pre-existing apparatus used for the experiments in Chapter 2. However, it quickly became apparent that it would be more expedient to build a new apparatus. Thus, the first really important step of this project presented in Chapter 3 was the design of this new apparatus. Some problems and difficulties had to be overcome to finally get a useful apparatus which would allow the study of a large set of configurations. A great number of experiments had to be tested and it was really important to be able to switch from one configuration to another quite quickly and easily. Furthermore, different instrumentation had to be added to record the flow velocity and the amplitude as well as the frequency motion. Then, the second step of the project could be carried out, namely a whole set of experiments on each of a number of flow configurations.

The stability of the system is investigated in each configuration: determining the critical flow velocity and frequency as well as the post-critical dynamics, i.e. the behaviour of the pipe at higher flow velocities. Thus, the stability of the system in one configuration can be compared to that in others. The main observations are that (i) the surrounding water has a destabilizing effect on the system, (ii) the motion amplitudes are much bigger when the pipe is discharging water than in the reverse case, and (iii) even though the type of instability, the critical flow velocity and the behaviour of the pipe at higher flow velocities depend on the configuration, some similarities exist. Finally, this study also shows that, for salt mining, storage or withdrawal of the liquid hydrocarbons and natural gas, the configuration involving a discharging pipe and an aspirating annular flow should be used as often as possible, because the system is much more stable than in the reverse configuration. It is realized of course that this conclusion is based on just the experiments described; it must be reconfirmed by other experiments to establish how robust this conclusion is.

In the future, to fine-tune the investigation on the dynamics of an aspirating cantilevered shell, it could be very useful to conduct experiments with a stiffer material. This experiment could even be conducted with water in the new apparatus presented in Chapter 3. Moreover, the analytical model needs some improvements, certainly by reconsidering the out-flow model and a new boundary condition. For the study undertaken in Chapter 3, the apparatus was designed to investigate the dynamics of systems with different characteristics. Thus, other sets of experiments should be conducted to study the influence of different parameters, such as the wall thickness of the pipe, the width of the annular gap or the presence of an additional ring at the free end of the outer tube to induce a leakage-flow instability. These further experiments would be of great interest for confirming and adjusting the conclusions reached in the present work regarding the stability as well as the post-critical dynamics.

Appendix A: Stress Resultants and Moments Expressions

In this appendix, the method to get the expressions of the stress resultants and moments is presented. Their definitions are presented in the first chapter of Flügge’s book (1973). To get their expressions for our particular case, we first need to express the displacement of an arbitrary point of the shell according to the displacement of the point located on the reference surface. Considering the assumptions made in Chapter 2, we get:

$$\begin{cases} \widetilde{U} = u - zw_{,x}\,, \\ \widetilde{V} = \dfrac{a-z}{a} v - zw_{,y}\,, \\ \widetilde{W} = w, \end{cases} \tag{A.1}$$

where $\widetilde{U}$, $\widetilde{V}$ and $\widetilde{W}$ are the displacements of an arbitrary point located at a distance *z* from the middle surface. Because of assumption 3, we consider only the strains ε_x, ε_ϑ and $\gamma_{x\vartheta}$. The expressions for the strains are given by

$$\begin{cases} \varepsilon_x = u_{,x} - zw_{,xx} + \dfrac{1}{2}\left(u_{,x}^2 + v_{,x}^2 + w_{,x}^2\right), \\ \varepsilon_\theta = \dfrac{1}{a} v_{,\theta} - \dfrac{z}{a}\dfrac{w_{,\theta\theta}}{a+z} + \dfrac{w}{z+a} \\ \qquad + \dfrac{1}{2}\left[\dfrac{u_{,\theta}^2}{a^2} + \dfrac{(v_{,\theta} + w)^2}{a^2} + \dfrac{(v - w_{,\theta})^2}{a^2}\right], \\ \gamma_{x\theta} = \dfrac{a+z}{a} v_{,x} + \dfrac{u_{,\theta}}{z+a} - \dfrac{2a+z}{a+z}\dfrac{z}{a} w_{,x\theta} \\ \qquad + \dfrac{1}{2}\left[\dfrac{u_{,x}\, u_{,\theta}}{a} + v_{,x}\dfrac{v_{,\theta} + w}{a} - w_{,x}\dfrac{v - w_{,\theta}}{a}\right]. \end{cases} \tag{A.2}$$

Using assumptions 2 and 3 and Hooke’s law, we determine the corresponding stresses:

$$\begin{cases} \sigma_{xx} = \dfrac{E}{1-\nu^2}\left(\varepsilon_x + \nu\varepsilon_\theta\right), \\ \sigma_{\theta\theta} = \dfrac{E}{1-\nu^2}\left(\nu\varepsilon_x + \varepsilon_\theta\right), \\ \sigma_{x\theta} = \dfrac{E}{2(1+\nu)}\gamma_{x\theta}. \end{cases} \tag{A.3}$$

We then introduce these expressions in the definitions of the stress resultants and couples. The terms of order higher than $(h/a)^2$ are neglected when performing the integration. Therefore, the final linear expressions are given by

$$\begin{gathered}
N_x = \frac{D}{a}[(u' + \nu v^{\cdot} + \nu w) - k_a w''], \\
N_\theta = \frac{D}{a}[(v^{\cdot} + w + \nu u') - k_a (w + w^{\cdot\cdot})], \\
N_{\theta x} = \frac{D}{a}\frac{1-\nu}{2}[(u^{\cdot} + v') + k_a (u^{\cdot} + w'^{\cdot})], \\
N_{x\theta} = \frac{D}{a}\frac{1-\nu}{2}[(u^{\cdot} + v') + k_a (v' - w'^{\cdot})], \\
M_x = D k_a (w'' + \nu w^{\cdot\cdot} - u' - \nu v^{\cdot}), \\
M_\theta = D k_a (w + w^{\cdot\cdot} + \nu w''), \\
M_{\theta x} = D k_a (1-\nu)\left(w'^{\cdot} + \frac{u^{\cdot} - v'}{2}\right), \\
M_x = D k_a (1-\nu)(w'^{\cdot} - v'),
\end{gathered} \tag{A.4}$$

where $D = Eh/(1-\nu^2)$

Appendix B: Application of the Variational Principle

To derive the equations using this principle, we need to develop the expressions of the variation of the elastic strain energy (2.3). To accomplish this step, we introduce the expressions of the strains given by (A.2):

$$
\begin{aligned}
\delta U_e = \int_0^L \int_0^{2\pi a} \int_{-h/2}^{h/2} \Bigg\{ & \sigma_{xx} \delta \bigg(u_{,x} - z w_{,xx} + \frac{1}{2} (u_{,x}^2 + v_{,x}^2 + w_{,x}^2) \bigg) \\
& + \sigma_{\theta\theta} \delta \bigg(\frac{1}{a} v_{,\theta} - \frac{z}{a} \frac{w_{,\theta\theta}}{a+z} + \frac{w}{z+a} \\
& + \frac{1}{2} \bigg[\frac{u_{,\theta}^2}{a^2} + \frac{(v_{,\theta} + w)^2}{a^2} + \frac{(v - w_{,\theta})^2}{a^2} \bigg] \bigg) \\
& + \sigma_{x\theta} \delta \bigg(\frac{a+z}{a} v_{,x} + \frac{u_{,\theta}}{z+a} - \frac{2a+z}{a+z} \frac{z}{a} w_{,x\theta} \\
& + \frac{1}{2} \bigg[\frac{u_{,x} u_{,\theta}}{a} + v_{,x} \frac{v_{,\theta} + w}{a} - w_{,x} \frac{v - w_{,\theta}}{a} \bigg] \bigg) \Bigg\} \bigg(1 \\
& + \frac{z}{a} \bigg) a dx d\theta dz.
\end{aligned}
\tag{B.1}
$$

We then develop this expression term by term:

$$
\begin{aligned}
\delta U_e = \int_0^L \int_0^{2\pi a} \int_{-h/2}^{h/2} \Bigg\{ & \sigma_{xx} \left(1 + \frac{z}{a} \right) (\delta u_{,x} - z \delta w_{,xx} + u_{,x} \delta u_{,x} + v_{,x} \delta v_{,x} \\
& + w_{,x} \delta w_{,x}) \\
& + \sigma_{\theta\theta} \bigg(\frac{\delta v_{,\theta} + \delta w}{a} + z \frac{\delta v_{,\theta} - \delta w_{,\theta\theta}}{a^2} \\
& + \frac{1}{a^2} \left(1 + \frac{z}{a} \right) [u_{,\theta} \delta u_{,\theta} + (v_{,\theta} + w) \delta v_{,\theta} \\
& + (v_{,\theta} + w) \delta w + (v - w_{,\theta}) \delta v - (v - w_{,\theta}) \delta w_{,\theta}] \bigg) \\
& + \sigma_{x\theta} \bigg(\frac{\delta u_{,\theta}}{a} - \frac{z}{a} \delta w_{,x\theta} + \left(1 + \frac{z}{a} \right) \delta v_{,x} \\
& + \frac{z}{a} \left(1 + \frac{z}{a} \right) (\delta v_{,x} - \delta w_{,x\theta}) \\
& + \frac{1}{a} \left(1 + \frac{z}{a} \right) [u_{,x} \delta u_{,\theta} + u_{,x} \delta u_{,\theta} + (v_{,\theta} + w) \delta v_{,x} \\
& + v_{,x} (\delta v_{,\theta} + \delta w) + (w_{,\theta} - v) \delta w_{,x} \\
& + w_{,x} (\delta w_{,\theta} - \delta v)] \bigg) \Bigg\} a dx d\theta dz.
\end{aligned}
\tag{B.2}
$$

Considering the definitions of the stress and moment resultants, we get

$$
\begin{aligned}
\delta U_e = \int_0^L \int_0^{2\pi a} \Big\{ & N_x[\delta u_{,x} + u_{,x}\,\delta u_{,x} + v_{,x}\,\delta v_{,x} + w_{,x}\,\delta w_{,x}] \\
& + M_x \delta w_{,xx} \\
& + \frac{N_\theta}{a^2}[(\delta v_{,\theta} + \delta w) + u_{,\theta}\,\delta u_{,\theta} + (v_{,\theta} + w)\delta v_{,\theta} \\
& + (v_{,\theta} + w)\delta w + (v - w_{,\theta})\delta v \\
& - (v - w_{,\theta})\delta w_{,\theta}] \\
& + \frac{M_\theta}{a^3}[a(\delta w_{,\theta\theta} - \delta v_{,\theta}) + u_{,\theta}\,\delta u_{,\theta} \\
& + (v_{,\theta} + w)\delta v_{,\theta} + (v_{,\theta} + w)\delta w \\
& + (v - w_{,\theta})\delta v - (v - w_{,\theta})\delta w_{,\theta}] \\
& + N_{\theta x}\frac{\delta u_{,\theta}}{a} + M_{\theta x}\frac{\delta w_{,x\theta}}{a} \\
& + \frac{N_{x\theta}}{a}[a\delta v_{,x} + u_{,x}\,\delta u_{,\theta} + u_{,x}\,\delta u_{,\theta} \\
& + (v_{,\theta} + w)\delta v_{,x} + v_{,x}\,(\delta v_{,\theta} + \delta w) \\
& + (w_{,\theta} - v)\delta w_{,x} + w_{,x}\,(\delta w_{,\theta} - \delta v)] \\
& + M_{x\theta}\frac{\delta w_{,x\theta} - \delta v_{,x}}{a}\Big\} a dx d\theta.
\end{aligned}
\tag{B.3}
$$

In what follows, we will only show how to get the equations in the *x* direction. For the two other equations, the same method has to be used. To obtain this equation, we only have to consider the terms involving *δu*, and their sum will be equal to zero because we want (2.7) to be valid for any set of perturbations (*δu*, *δv*, *δw*), . In equation (B.3), some derivatives of the displacement *δu* are present; we shall rearrange these components of the equation by using the divergence theorem. For example, the first term becomes

$$
\int_0^L \int_0^{2\pi a} N_x \delta u_{,x}\, a dx d\theta = \int_0^{2\pi a} [N_x \delta u a d\theta]_{x=0}^{x=L} - \int_0^L \int_0^{2\pi a} N_{x,x}\,\delta u a dx d\theta. \tag{B.4}
$$

What we finally obtain from (B.3) is

$$\begin{aligned}\int_0^L\int_0^{2\pi a} a\Big\{&N_{x,x}+(N_x u_{,x})_{,x}+\left(\frac{N_\theta u_{,\theta}}{a^2}\right)_{,\theta}+\left(\frac{M_\theta u_{,\theta}}{a^3}\right)_{,\theta}+\left(\frac{N_{\theta x}}{a}\right)_{,\theta}\\ &+\left(\frac{N_{x\theta}u_{,x}}{a}\right)_{,\theta}+\left(\frac{N_{x\theta}u_{,\theta}}{a}\right)_{,x}\Big\}\delta u dx d\theta\\ &-\int_0^{2\pi a} a\left[N_x(1+u_{,x})+N_{x\theta}\frac{u_{,\theta}}{a}\right]_{x=0}^{x=L}\delta u d\theta\\ &-\int_0^L a\left[N_\theta\frac{u_{,\theta}}{a^2}\right]_{\theta=0}^{\theta=2\pi}\delta u dx\\ &+\int_0^L\int_0^{2\pi a} a\left\{p_x^*\left(1+u_{,x}+\frac{v_{,\theta}+w}{a}\right)-p_z^* w_{,x}\right\}\delta u dx d\theta\\ &+\int_0^{2\pi a}[P_x^*]_{x=0}^{x=L} a\delta u d\theta=0.\end{aligned} \tag{B.5}$$

As the shell is a closed cylinder, we have $\int_0^L a\left[N_\theta\frac{U_{,\theta}}{a^2}\right]_{\theta=0}^{\theta=2\pi}\delta u dx=0$. Furthermore, (B.5) is true for any variational displacement. Keeping in mind that the shell is clamped-free, we obtain the boundary conditions:

$$\begin{gathered}u=0\ at\ x=0,\\ N_x(1+u_{,x})+N_{x\theta}\frac{u_{,\theta}}{a}=P_x^*\ at\ x=L.\end{gathered} \tag{B.6}$$

Considering the linear version of the above, we finally obtain

$$\begin{gathered}u=0\ at\ x=0,\\ aN_{x0}=P_x^*\ at\ x=L,\\ N_{x1}=0\ at\ x=L,\end{gathered} \tag{B.7}$$

where P_x^* is defined in Chapter 2. The equation in the *x*-direction is given by

$$\begin{aligned}N_{x,x}+(N_x u_{,x})_{,x}&+\left(\frac{N_\theta u_{,\theta}}{a^2}\right)_{,\theta}+\left(\frac{M_\theta u_{,\theta}}{a^3}\right)_{,\theta}+\left(\frac{N_{\theta x}}{a}\right)_{,\theta}+\left(\frac{N_{x\theta}u_{,x}}{a}\right)_{,\theta}\\ &+\left(\frac{N_{x\theta}u_{,\theta}}{a}\right)_{,x}+p_x^*\left(1+u_{,x}+\frac{v_{,\theta}+w}{a}\right)-p_z^* w_{,x}=0.\end{aligned} \tag{B.8}$$

The zero-order equation is then easily obtained. Here we give also these equations along ϑ and z because they are useful in obtaining the final form of the first-order equation:

$$\begin{cases} N_{x0,x} = -p_{x0}, \\ N_{\theta 0,\theta} = 0, \\ p_0 = \dfrac{N_{\theta 0}}{a}. \end{cases} \tag{B.9}$$

Using (B.8) and taking into account only the linear terms of the first order, we finally have:

$$\begin{aligned} &aN_{x1,x} + aN_{x0}u_{,xx} + aN_{x0,x}\,u_{,x} + \frac{N_{\theta 0}}{a}u_{,\theta\theta} + N_{\theta x,\theta} \\ &\qquad + ap_{x0}\left(u_{,x} + \frac{v_{,\theta} + w}{a}\right) - ap_0 w_{,x} - \rho_s ah\frac{\partial^2 u}{\partial t^2} = 0. \end{aligned} \tag{B.10}$$

Considering (B.9), this leads to

$$\begin{aligned} &aN_{x1,x} + N_{\theta x,\theta} + aN_{x0}u_{,xx} + p_{x0}(v_{,\theta} + w) + \frac{N_{\theta 0}}{a}(u_{,\theta\theta} - aw_{,x}) \\ &\qquad = \rho_s ah\frac{\partial^2 u}{\partial t^2}. \end{aligned} \tag{B.11}$$

From the expressions of the stress and moment resultants (A.4), we have:

$$\begin{aligned} L_1(u,v,w) = {} & u'' + \frac{1-\nu}{2}u^{\cdot\cdot} + \frac{1+\nu}{2}v'^{\cdot} + \nu w' \\ & + k\left[\frac{1-\nu}{2}u^{\cdot\cdot} - w''' + \frac{1-\nu}{2}w'^{\cdot\cdot}\right] + \tau_x u'' \\ & + \tau(v^{\cdot} + w) + \tau_\theta(u^{\cdot\cdot} - w') - \gamma\frac{\partial^2 u}{\partial t^2} = 0. \end{aligned} \tag{B.12}$$

Following the same procedure, we get the other boundary conditions for a clamped-free shell:

$$\begin{gathered} v = w = \frac{\partial w}{\partial x} = 0 \; at \; x = 0, \\ N_{x\theta} - \frac{M_{x\theta}}{a} = 0 \; at \; x = L, \\ M_x = 0 \; at \; x = L, \\ aM_{x,x} + M_{x\theta,\theta} + M_{\theta x,\theta} = 0 \; at \; x = L, \end{gathered} \tag{B.13}$$

and the two other first order equations:

$$\begin{aligned} N_{\theta,\theta} + aN_{x\theta,x} - \frac{1}{a}M_{\theta,\theta} - M_{x\theta,x} + N_{x0}v_{,xx} + \frac{N_{\theta0}}{a^2}\left(v_{,\theta\theta} + w_{,\theta}\right) \\ = \rho_s ah\frac{\partial^2 v}{\partial t^2}, \end{aligned} \tag{B.14}$$

$$\begin{aligned} aM_{x,xx} + M_{x\theta,x\theta} + M_{\theta x,x\theta} + \frac{1}{a}M_{\theta,\theta\theta} + N_{\theta1} - aN_{x0}w_{,xx} \\ + \frac{N_{\theta0}}{a}\left(-au_{,x} + v_{,\theta} - w_{,\theta\theta}\right) - aq = -\rho_s ah\frac{\partial^2 w}{\partial t^2}. \end{aligned} \tag{B.15}$$

Appendix C: Matrix Elements

Before giving the matrix elements, here are the expressions of the coefficients of the terms W_{ikn}:

$$\begin{aligned} J_{kmn}^{1,1} &= \varepsilon^2 b_{km}\left[\overline{\Omega}^2 - \frac{1-\nu}{2}n^2(1+k_a) - \hat{B}_3 n^2\right] - n^2\varepsilon^2\hat{A}_3 h_{km} \\ &\quad + \varepsilon^4\left[1+\hat{B}_1\right]d_{km} + \varepsilon^4\hat{A}_1 l_{km}, \end{aligned} \tag{C.1}$$

$$J_{kmn}^{1,2} = \frac{1+\nu}{2}n\varepsilon^2 b_{km} + \hat{B}_2 n\varepsilon a_{km} - \nu n\varepsilon^2\varphi_m(1)\varphi'_k(1), \tag{C.2}$$

$$\begin{aligned} J_{kmn}^{1,3} &= \varepsilon^2 b_{km}\left[\nu - k_a\frac{1-\nu}{2}n^2 - \hat{B}_3\right] - \varepsilon^2 h_{km}\hat{A}_3 - k_a\varepsilon^4 d_{km} \\ &\quad + \hat{B}_2\varepsilon a_{km} - \nu\varepsilon^2\varphi_m(1)\varphi'_k(1), \end{aligned} \tag{C.3}$$

$$J_{kmn}^{2,1} = -\frac{1+\nu}{2}n\varepsilon^2 c_{km} + \frac{1-\nu}{2}n\varepsilon^2\varphi'_m(1)\varphi_k(1), \tag{C.4}$$

$$\begin{aligned} J_{kmn}^{2,2} &= \delta_{km}\left[\overline{\Omega}^2 - \mathrm{n}^2\left(1+\hat{B}_3\right)\right] - n^2\hat{A}_3 g_{km} \\ &\quad + \varepsilon^2 c_{km}\left[\frac{1-\nu}{2}(1+3k_a) + \hat{B}_1\right] + \varepsilon^2 k_{km}\hat{A}_1 \\ &\quad - \frac{1-\nu}{2}\varepsilon^2(1+3k_a)\varphi'_m(1)\varphi_k(1), \end{aligned} \tag{C.5}$$

$$\begin{aligned} J_{kmn}^{2,3} &= -\delta_{km}n\left(1+\hat{B}_3\right) - n\hat{A}_3 g_{km} + \varepsilon^2 c_{km}k_a\frac{3-\nu}{2}n \\ &\quad - \frac{1-\nu}{2}3nk_a\varepsilon^2\varphi'_m(1)\varphi_k(1), \end{aligned} \tag{C.6}$$

$$\begin{aligned} J_{kmn}^{3,1} &= \delta_{km}k_a\lambda_m^4\varepsilon^4 - \varepsilon^2 c_{km}\left[\nu - k_a\frac{1-\nu}{2}n^2 - \hat{B}_3\right] + \varepsilon^2 k_{km}\hat{A}_3 \\ &\quad - \frac{1-\nu}{2}n^2\varepsilon^2\varphi'_m(1)\varphi_k(1), \end{aligned} \tag{C.7}$$

$$\begin{aligned} J_{kmn}^{3,2} &= -\delta_{km}n\left[1+\hat{B}_3\right] - n\hat{A}_3 g_{km} + \varepsilon^2 c_{km}\frac{3-\nu}{2}k_a n \\ &\quad + k_a\nu n\varepsilon^2\varphi_m(1)\varphi'_k(1) - \frac{3-\nu}{2}\varepsilon^2 k_a n\varphi'_m(1)\varphi_k(1), \end{aligned} \tag{C.8}$$

$$
\begin{aligned}
J_{kmn}^{3,3} = \bar{\Omega}^2 \left(\delta_{km} + q_{kmn}^{(1)}\right) + \bar{\Omega}\bar{U}\left(2q_{kmn}^{(2)} - i\frac{\mu_e \varepsilon}{2}\varphi_m(1)\varphi_k(1)\right) \\
- \delta_{km}\left[1 + k_a \lambda_m^4 \varepsilon^4 + k_a (n^2-1)^2 + \hat{B}_3 n^2\right] \\
- n^2 \hat{A}_3 g_{km} + \varepsilon^2 c_{km}\left[2n^2 k_a + \hat{B}_1\right] + \varepsilon^2 k_{km} \hat{A}_1 \\
+ \bar{U}^2\left(q_{kmn}^{(3)} - \frac{\mu_e \varepsilon^2}{2}\alpha\varphi'_m(1)\varphi_k(1)\right) \\
+ \nu n^2 \varepsilon^2 k_a \varphi_m(1)\varphi'_k(1) \\
- (2-\nu) n^2 \varepsilon^2 k_a \varphi'_m(1)\varphi_k(1).
\end{aligned}
\qquad \text{(C.9)}
$$

C.1 Matrix [M]

In this matrix the only non-zero terms are located on the diagonal:

$$M_{km}^{1,1} = \varepsilon^2 b_{km}, \qquad \text{(C.10)}$$

$$M_{km}^{2,2} = \delta_{km}, \qquad \text{(C.11)}$$

$$M_{km}^{3,3} = \delta_{km} + q_{kmn}^{(1)}. \qquad \text{(C.12)}$$

C.2 Matrix [C]

This matrix has only one non-zero term:

$$C_{km}^{3,3} = \bar{U}\left(2q_{kmn}^{(2)} - i\frac{\mu_e \varepsilon}{2}\varphi_m(1)\varphi_k(1)\right). \qquad \text{(C.13)}$$

C.3 Matrix [K]

This matrix is much more complicated. All of its terms are non-zero. To better understand the influence of each term, we separate it in four different matrixes: [K$_1$], [K$_{1bis}$], [K$_2$] and [K$_3$]. Matrix [K$_1$]

C.1.1 Matrix [K1]

Matrix [K$_1$] regroups the terms coming from the standard Flügge's shell theory, except for the perturbation pressure term, namely

$$K_{1km}^{1,1} = -\frac{1-\nu}{2} n^2 (1 + k_a)\varepsilon^2 b_{km} + \varepsilon^4 d_{km}, \qquad \text{(C.14)}$$

$$K_{1km}^{1,2} = \frac{1+\nu}{2} n \varepsilon^2 b_{km}, \qquad \text{(C.15)}$$

$$K_{1km}^{1,3} = \varepsilon^2 b_{km}\left[\nu - k_a\frac{1-\nu}{2}n^2\right] - k_a\varepsilon^4 d_{km}, \tag{C.16}$$

$$K_{1km}^{2,1} = -\frac{1+\nu}{2}n\varepsilon^2 c_{km}, \tag{C.17}$$

$$K_{1km}^{2,2} = -\mathrm{n}^2\delta_{km} + \varepsilon^2 c_{km}\left[\frac{1-\nu}{2}(1+3k_a)\right], \tag{C.18}$$

$$K_{1km}^{2,3} = -\delta_{km}n + \varepsilon^2 c_{km}k_a\frac{3-\nu}{2}n, \tag{C.19}$$

$$K_{1km}^{3,1} = \delta_{km}k_a\lambda_m^4\varepsilon^4 + \varepsilon^2 c_{km}\left[k_a\frac{1-\nu}{2}n^2 - \nu\right], \tag{C.20}$$

$$K_{1km}^{3,2} = -\delta_{km}n + \varepsilon^2 c_{km}\frac{3-\nu}{2}k_a n, \tag{C.21}$$

$$K_{1km}^{3,3} = -\delta_{km}[1 + k_a\lambda_m^4\varepsilon^4 + k_a(n^2-1)^2] + \varepsilon^2 c_{km}2n^2 k_a. \tag{C.22}$$

C.1.2 Matrix [K$_{1bis}$]

Matrix [K$_{1bis}$] accounts for the unsteady pressure term and the new boundary condition term due to the aspiration of a fluid, both of them depending on the square of the velocity, namely

$$K_{1biskm}^{3,3} = \bar{U}^2\left(q_{kmn}^{(3)} - \frac{\mu_e\varepsilon^2}{2}\alpha\varphi'_m(1)\varphi_k(1)\right). \tag{C.23}$$

C.1.3 Matrix [K2]

In matrix [K$_2$], the boundary conditions of a clamped-free shell are considered:

$$K_{2km}^{1,1} = 0, \tag{C.24}$$

$$K_{2km}^{1,2} = -\nu n\varepsilon^2\varphi_m(1)\varphi'_k(1), \tag{C.25}$$

$$K_{2km}^{1,3} = -\nu\varepsilon^2\varphi_m(1)\varphi'_k(1), \tag{C.26}$$

$$K_{2km}^{2,1} = \frac{1-\nu}{2}n\varepsilon^2\varphi'_m(1)\varphi_k(1), \tag{C.27}$$

$$K_{2km}^{2,2} = -\frac{1-\nu}{2}\varepsilon^2(1+3k_a)\varphi'_m(1)\varphi_k(1), \tag{C.28}$$

$$K_{2km}^{2,3} = -\frac{1-\nu}{2}3nk_a\varepsilon^2\varphi'_m(1)\varphi_k(1), \tag{C.29}$$

$$K^{3,1}_{2km} = -\frac{1-\nu}{2} n^2 \varepsilon^2 \varphi'_m(1)\varphi_k(1), \tag{C.30}$$

$$K^{3,2}_{2km} = k_a \nu n \varepsilon^2 \varphi_m(1)\varphi'_k(1) - \frac{3-\nu}{2} \varepsilon^2 k_a n \varphi'_m(1)\varphi_k(1), \tag{C.31}$$

$$K^{3,3}_{2km} = \nu n^2 \varepsilon^2 k_a \varphi_m(1)\varphi'_k(1) - (2-\nu) n^2 \varepsilon^2 k_a \varphi'_m(1)\varphi_k(1). \tag{C.32}$$

C.1.4 Matrix [K₃]

Finally, matrix [K₃] is composed of the terms related to steady viscous effects

$$K^{1,1}_{3km} = \varepsilon^4\left(\hat{B}_1 d_{km} + \hat{A}_1 l_{km}\right) - n^2\varepsilon^2\left(\hat{B}_3 b_{km} + \hat{A}_3 h_{km}\right), \tag{C.33}$$

$$K^{1,2}_{3km} = \hat{B}_2 n \varepsilon a_{km}, \tag{C.34}$$

$$K^{1,3}_{3km} = -\varepsilon^2\left(\hat{A}_3 h_{km} + \hat{B}_3 b_{km}\right) + \hat{B}_2 \varepsilon a_{km}, \tag{C.35}$$

$$K^{2,1}_{3km} = 0, \tag{C.36}$$

$$K^{2,2}_{3km} = -n^2\left(\hat{A}_3 g_{km} + \hat{B}_3 \delta_{km}\right) + \varepsilon^2\left(\hat{A}_1 k_{km} + \hat{B}_1 c_{km}\right), \tag{C.37}$$

$$K^{2,3}_{3km} = -n\left(\hat{A}_3 g_{km} + \hat{B}_3 \delta_{km}\right), \tag{C.38}$$

$$K^{3,1}_{3km} = \varepsilon^2\left(\hat{A}_3 k_{km} + \hat{B}_3 c_{km}\right), \tag{C.39}$$

$$K^{3,2}_{3km} = -n\left(\hat{A}_3 g_{km} + \hat{B}_3 \delta_{km}\right), \tag{C.40}$$

$$K^{3,3}_{3km} = -n^2\left(\hat{A}_3 g_{km} + \hat{B}_3 \delta_{km}\right) + \varepsilon^2\left(\hat{A}_1 k_{km} + \hat{B}_1 c_{km}\right). \tag{C.41}$$

Appendix D: Validation of the Computer Program

Before using the computer program for the case of a cantilevered aspirating fluid, it was necessary to get some preliminary results to validate the method of resolution but also to determine some parameters involved in the program.

Two important aspects of the theory had to be examined: the validity of the extended Galerkin method for solving the equations of motion and the usefulness of the concept of an out-flow model for describing the fluid behaviour downstream of the free end. As several models were defined, it was important to determine the most suitable one, as well as the most suitable distance beyond the free end of the shells for flow perturbations to die out.

Furthermore, a numerical integration is required to calculate the unsteady fluid forces because they are obtained through a Fourier transform method. To perform it, it was decided to use the Gaussian quadrature method. Firstly, the forces are calculated in some cases by direct integration to validate the use of the Gaussian quadrature and the number of necessary points. Then, comparing the found critical flow velocities with existing results, the integration stepsize, the domain of integration and the number of admissible functions are determined.

As all of the examined parameters are parts of inviscid theory only, and because the previous work did not involve any viscous effects, the present calculations were conducting without considering steady viscous effects also.

D.1 Natural Frequencies of a Cylinder

Gill (1972) experimentally measured the natural frequencies of a cantilevered shell with the following parameters:

$$\begin{gathered} E = 2.1 * 10^{11}\,\mathrm{N/m^2}, \qquad \nu = 0.28, \qquad \rho_s = 7.8 * 10^3\,\mathrm{kg/m^3}, \\ L = 0.502\,\mathrm{m}, \qquad a = 0.0635\,\mathrm{m}, \qquad h = 0.0016\,\mathrm{m}, \qquad \mu = \chi = 0. \end{gathered} \tag{D.1}$$

In 1974, Sharma theoretically calculated the natural frequencies for the same system. These results are compared with those obtained with the present theory in Table D.1. It can be seen that the results obtained with Model 3 and ten admissible functions are in good agreement with the one measured by Gill in the experiments or found by Sharma's theory. The agreement with experiment is even better with the present theory. The number of admissible functions is such that increasing it changes only slightly the natural frequencies of each mode, and the extended Galerkin method appears to be a suitable way to solve the equations of motion.

Table D.1: Comparison between the natural frequencies of a cantilevered shell from Sharma's theory, Gill's experiments and the present theory

n	Experiments or theory considered	m=1	m=2	m=3	m=4
2	Gill (1972)	293.0	827.0	1894.8	---
	Sharma (1974)	318.0	1006.4	2356.5	3882.3
	Present theory	310.9	938.8	2203.6	3677.8
3	Gill (1972)	760.0	886.0	1371.0	2155.0
	Sharma (1974)	769.7	927.7	1504.2	2403.6
	Present theory	754.0	902.2	1446.5	2307.0
4	Gill (1972)	1451.0	1503.0	1673.0	2045.0
	Sharma (1974)	1465.3	1523.3	1726.0	2148.5
	Present theory	1436.2	1491.6	1686.7	2092.7

D.2 Gaussian Quadrature

To reduce the computing time required, a Gaussian quadrature has been used to calculate the unsteady fluid forces. To determine the validity of this method and the values of the involved parameters (integration stepsize, number of points and domain of integration), a set of calculations with different values of these parameters has been conducted. The chosen values are usually a compromise between the accuracy of the result and of the computing time required. To have a reference for the obtained results, the properties of the pipe used in these calculations are the same as in Païdoussis and Denise (1972):

$$\begin{gathered} E = 8.957 * 10^5\,\mathrm{N/m^2}, \qquad \nu = 0.5, \qquad \rho_s = 850\,\mathrm{kg/m^3}, \\ L = 0.1013\ \mathrm{m}, \qquad a = 7.85 * 10^{-3}\ \mathrm{m}, \qquad h = 1.78 * 10^{-4}\ \mathrm{m}, \\ \rho_{air} = 1.1564\,\mathrm{kg/m^3}, \qquad \mu = \chi = 0 \end{gathered} \tag{D.2}$$

Firstly, it was necessary to validate the use of the Gaussian quadrature. For that purpose, the unsteady fluid forces defined by (2.78) to (2.80) were calculated using a direct numerical integration over the interval [-300,300] using a million points. The results are presented in Table D.2, where *m* represents the axial mode of the perturbation and *k* the axial mode of the corresponding variations as defined in (2.81) and (2.82). For clarity, only the results with *k* and *n* equal to 1 are shown. It appears very clearly that the only differences between the two calculations lie in really small numbers that can be considered as equal to zero in comparison with the modulus of the considered term. That is why

Table D.2: Comparison of the unsteady viscous forces using a Gaussian quadrature and a direct numerical integration for *n*=1 and *k*=1

Gaussian quadrature	Direct integration
$\begin{cases} q_{111}^{(1)} = 0.122 + 5.20 * 10^{-5} i \\ q_{121}^{(1)} = -0.0138 + 4.41 * 10^{-3} i \\ q_{131}^{(1)} = 0.0205 - 0.0112 i \\ q_{121}^{(1)} = -0.0234 + 0.0143 i \end{cases}$	$\begin{cases} q_{111}^{(1)} = 0.122 + 5.20 * 10^{-5} i \\ q_{121}^{(1)} = -0.0138 + 4.41 * 10^{-3} i \\ q_{131}^{(1)} = 0.0205 - 0.0112 i \\ q_{121}^{(1)} = -0.0234 + 0.0143 i \end{cases}$
$\begin{cases} q_{111}^{(2)} = -5.78 * 10^{-20} - 0.00922 i \\ q_{121}^{(2)} = -6.39 * 10^{-19} + 0.0218 i \\ q_{131}^{(2)} = -1.00 * 10^{-19} - 0.0172 i \\ q_{121}^{(2)} = -2.95 * 10^{-19} + 0.0186 i \end{cases}$	$\begin{cases} q_{111}^{(2)} = -5.18 * 10^{-17} - 0.00922 i \\ q_{121}^{(2)} = -1.23 * 10^{-16} + 0.0218 i \\ q_{131}^{(2)} = 1.79 * 10^{-16} - 0.0172 i \\ q_{121}^{(2)} = -2.51 * 10^{-16} + 0.0186 i \end{cases}$
$\begin{cases} q_{111}^{(3)} = -2.12 * 10^{-4} + 2.30 * 10^{-20} i \\ q_{121}^{(3)} = 3.95 * 10^{-3} - 6.34 * 10^{-20} i \\ q_{131}^{(3)} = -9.35 * 10^{-3} - 1.54 * 10^{-19} i \\ q_{121}^{(3)} = 1.25 * 10^{-2} - 2.79 * 10^{-20} i \end{cases}$	$\begin{cases} q_{111}^{(3)} = -2.12 * 10^{-4} + 7.66 * 10^{-20} i \\ q_{121}^{(3)} = 3.95 * 10^{-3} + 6.82 * 10^{-19} i \\ q_{131}^{(3)} = -9.35 * 10^{-3} + 7.13 * 10^{-19} i \\ q_{121}^{(3)} = 1.25 * 10^{-2} - 1.44 * 10^{-18} i \end{cases}$

using a Gaussian quadrature is the proper way to calculate the unsteady viscous forces.

Secondly, the integration stepsize had to be determined. At the same time, the influence of the number of points inside each interval was also studied and it was observed that, as long as it is greater than two, the predictions for the critical flow velocities are identical up to the sixth significant digit for all the results. So it was decided to take only two points in each interval. To study the influence of the integration stepsize, Δ, the domain of integration and the number of admissible functions remained unchanged with

$$[-z, z] = [-300, 300], \quad l = 3 \text{ and } M = 10.$$

The results in Table D.3 show that the calculated critical flow velocities are identical up to the fourth significant digit as long as the integration stepsize is smaller than two. For time computing reasons, the best is to chose this value and, from now on, the integration stepsize will always be taken equal to two: $\Delta = 2$.

Table D.3: Comparison of the critical flow velocities of a cantilevered shell obtained by the present theory using different integration stepsizes with those calculated by Païdoussis and Denise (1972). The axial mode number *m* is associated with instability.

n	Model	Present Theory						Païdoussis and Denise (1972)
		$\Delta = 4.0$	*m*	$\Delta = 2.0$	*m*	$\Delta = 1.0$	*m*	
1	1	0.609	1	0.609	1	0.609	1	0.959
	2	1.091	2	0.963	2	0.963	2	
	3	1.056	2	0.957	2	0.957	2	
2	1	0.374	2	0.364	2	0.364	2	0.452
	2	0.484	2	0.417	2	0.417	2	
	3	0.46	2	0.415	2	0.415	2	
3	1	0.400	3	0.405	3	0.405	3	0.524
	2	0.363	3	0.466	2	0.466	2	
	3	0.424	2	0.465	2	0.465	2	

Thirdly, the domain of integration is [-∞, +∞] but it is not possible to carry out a numerical integration over this domain, it has to be restricted to a narrower one. In that case, $M = 10$ and $\Delta = 2$. Three sets of calculation were done with the following domain of integration:

$$[-z, z] = [-300, 300], \qquad [-z, z] = [-1000, 1000], \qquad [-z, z] = [-5000, 5000]. \tag{D.3}$$

From the results in Table D.4, it can be seen that for each circumferential mode *n*, the predicted critical flow velocities remained unchanged up to the fourth significant digit; so, the narrowest of the domains of integration can be used in the calculations.

Table D.4: Comparison of the critical flow velocities of a cantilevered shell obtained by the present theory using different domains of integration with those calculated by Païdoussis and Denise (1972). The axial mode number *m* is associated with instability.

n	Model	Present theory		Païdoussis and Denise (1972)
		$[-z,z]=[-300,300]$ or $[-1000,1000]$ or $[-5000,5000]$	m	
1	1	0.609	1	0.959
	2	0.963	2	
	3	0.957	2	
2	1	0.364	2	0.452
	2	0.417	2	
	3	0.415	2	
3	1	0.405	2	0.524
	2	0.466	2	
	3	0.465	2	

D.3 Number of Admissible Functions

The number of admissible functions used in the calculations corresponds to the number of axial modes that is considered to describe the motion of the shell. That is why, the more functions are taken into account the more accurate should the results be. Thus, a compromise has to be found between the accuracy of the result and the required computing time. As shown in Table D.5, the first instability usually arises in the lower axial modes. So, not considering the higher axial modes does not affect the predicted mode of instability. The results in that table numerically describe the effect of the number of considered admissible functions. For each axial mode, the predicted critical flow velocity seems to approach a limit value, and the difference between the critical velocities calculated for two consecutive *M* decreases as *M* is increased. For example, the relative differences of these velocities for the first circumferential mode are (4.1%, 2.1%, 0.41%, 0.21%, 0.10%). It also appears in the third mode (n=3) that the predicted axial mode of instability changes as *M* is increased, from *m*=1 to *m*=3 and finally to *m*=2 for Model 2 and Model 3. Thus it seems important to take a sufficiently large number of admissible functions to have an accurate prediction. In the end, $M = 10$ appears to be high enough to get a good accuracy, but it is also a good choice regarding the required computing time.

Table D.5: Comparison of the critical flow velocities of a cantilevered shell obtained by the present theory using an increasing number of admissible functions with those calculated by Païdoussis and Denise (1972). The axial mode number *m* is associated with instability.

n	Model	Present Theory						Païdoussis and Denise (1972)
		$M = 2$	m	$M = 4$	m	$M = 6$	m	
1	1	0.636	1	0.618	1	0.612	1	0.959
	2	1.023	2	0.978	2	0.969	2	
	3	1.013	2	0.971	2	0.963	2	
2	1	0.373	2	0.367	2	0.365	2	0.452
	2	0.423	2	0.420	2	0.418	2	
	3	0.420	2	0.418	2	0.416	2	
3	1	1.052	1	0.407	3	0.406	3	0.524
	2	1.484	1	0.468	3	0.464	3	
	3	1.476	1	0.467	3	0.463	3	
n	Model	Present Theory						Païdoussis and Denise (1972)
		$M = 8$	m	$M = 10$	m	$M = 12$	m	
1	1	0.610	1	0.609	1	0.609	1	0.959
	2	0.965	2	0.963	2	0.961	2	
	3	0.959	2	0.957	2	0.956	2	
2	1	0.365	2	0.364	2	0.364	2	0.452
	2	0.418	2	0.417	2	0.417	2	
	3	0.415	2	0.415	2	0.415	2	
3	1	0.405	3	0.405	3	0.405	3	0.524
	2	0.465	2	0.466	2	0.468	2	
	3	0.463	2	0.465	2	0.466	2	

D.4 Out-flow Model

It was quickly discovered that the predicated behaviour of the cantilevered shell was abnormal if no out-flow model was applied. Indeed, it was predicted to lose stability by divergence and then by coupled mode flutter. This is the exact behaviour of a shell with both ends supported. Thus, the addition of an out-flow model appeared to be crucial. As specified in Chapter 2, four different models were applied. Their physical characteristics are presented by Nguyen in his thesis (1992) and in Nguyen et al. (1993).

From Table D.3, Table D.4 and Table D.5, it can be observed that Model 1 gives results really different from those found by Païdoussis and Denise (1972) but also by Model 2 and Model 3. Firstly, for n=1, it always predicts a first axial mode instability, whereas the two other models predict a second axial mode instability. Secondly, the same kind of difference appears for *n*=3. It predicts a third axial mode instability, whereas the two other models predict a second axial mode instability. Finally whereas the results of Model 2 and Model 3 are always really close (they differ by less than 0.5%), the results of Model 1 are really different. Even for *n*=2 where the same axial mode of instability is predicted, the difference between Model 1 and Model 3 is greater than 10%. These three models are empirical and Model 1 seems less realistic than the two other ones, as, in that model the decay of the perturbation is not really smooth since only the continuity of the pressure is imposed. That is why Model 1 was not considered to be relevant.

Table D.6: Comparison of the critical flow velocities of a cantilevered shell obtained by the present theory with Model 4 using different integration stepsizes with the one calculated with Model 3. The axial mode number *m* is associated with instability.

Δ	Model 4					
	n=1	m	n=2	m	n=3	m
4	0.807	2	0.357	2	<0.01	2
2	0.978	2	0.425	2	0.472	3
1	0.961	2	0.417	2	0.467	3
0.75	0.959	2	0.416	2	0.465	2
0.5	0.958	2	0.416	2	0.465	2
0.25	0.958	2	0.416	2	0.465	2
0.1	0.958	2	0.416	2	0.465	2
	Model 3					
2	0.957	2	0.415	2	0.465	2

Model 4 was developed to overcome some numerical difficulties due to the fact that the solution of the problem was not converging with any of the three first models when *l* was increased to infinity. This non-convergence arises because of the non-existence of $\lim_{l\to\infty} H_{km}(\bar{\alpha})$ due to the presence of a term in le^{il}. Even if it is finite for any *l*, it does not have a limit when $l \to \infty$. The main idea was to consider that the perturbations of the flow would decay really slowly and die out infinitely far from the free end. It appeared (Nguyen et al., 1993) that the results with this new model would be slightly different than with Model 3. But, more recent results presented in Table D.6 prove that if the integration stepsize of the Gaussian quadrature are modified, the critical flow velocities predicted by Model 4 tend toward the same limit as Model 3. Thus, to get the same result, a much smaller integration stepsize has to be used and that leads to a much longer computing time. Furthermore, for the case of an aspirating shell that is motivating this study, it does not seem relevant to consider that perturbations can occur really far from the free end. They might grow at a distance of the order of magnitude of a few pipe lengths. For those reasons, it was decided to drop Model 4.

Table D.7: The critical flow velocities of a cantilevered shell obtained by the present theory using different length *l*. A dash signifies that the shell is immediately unstable.

n	Model	Length *l*									
		1.25	1.5	2	2.5	3	3.5	4	5	10	50
1	2	0.884	0.936	0.955	0.960	0.963	0.887	-	-	-	-
	3	0.836	0.905	0.942	0.952	0.957	0.940	0.960	1.023	-	-
2	2	0.388	0.408	0.415	0.417	0.417	-	-	-	-	-
	3	0.364	0.395	0.409	0.414	0.415	0.408	0.412	0.444	-	-
3	2	0.447	0.460	0.465	0.466	0.466	-	-	-	-	-
	3	0.426	0.451	0.461	0.464	0.465	0.471	0.476	0.480	-	-

The main difficulty with Models 2 and 3 lies in the determination of the length *l*, because of the convergence problem mentioned before and emphasized in Table D.7. The first conclusion is that if *l* is greater than 10, the solution is inadequate because some modes, even small ones like *m*=2, are unstable from the very beginning. It should also be noted that for $3.5 \leq l \leq 5$, some of the axial modes higher than *M*=5 are always unstable for Model 2. That is why they were considered to be immediately unstable. For Model 3, some of the axial modes higher than five are unstable at the beginning but regain stability shortly. If material damping would have been considered, they would have been stable at the beginning. That is why it is considered that the instability occurring for a lower axial mode was the relevant one. For $2 \leq l \leq 3$, the predicted critical velocities are close to each other. For example, for the first circumferential mode and Model 3, they differ by 1.5%. For the greater values of this length, the predicted critical velocities increase, sometimes by more than 6.5% for the previous example. For lower values, the predicted velocities decrease by more than 5% for the same example. For $l < 1$, the system becomes unstable at infinitesimal flow velocity. So it seems that the length *l* should be between 2 and 3. It is still not understood why other values give really unexpected results, e.g. predicting that the system is always unstable.

Finally, as the decay of the perturbation is smoother in Model 3 because of the continuity of the derivative of the pressure at the free end and at $\xi=l$, and because a solution could be found for higher value of the length *l*, it was chosen to adopt Model 3.

D.5 Conclusion

In this appendix, some preliminary calculations were conducted to validate the computer program. It was thus verified that the extended Galerkin method was a good one to solve the equations of motion. Comparing the results obtained by varying some parameters allowed to get the optimum values of these parameters and to validate the Gaussian quadrature method to calculate the unsteady viscous forces. Finally, the importance of an out-flow model was proved, and then the most suitable mode was chosen. The results are shown in Table D.8.

Table D.8: The parameters of the computer program

Number of Gaussian points	2
Integration stepsize	$\Delta = 2$
Domain of integration	[-300; 300]
Number of admissible functions	M=10
Chosen model	Model 3
Length *l*	$2 \leq l \leq 3$

Appendix E: Technical Drawings for Chapter 2

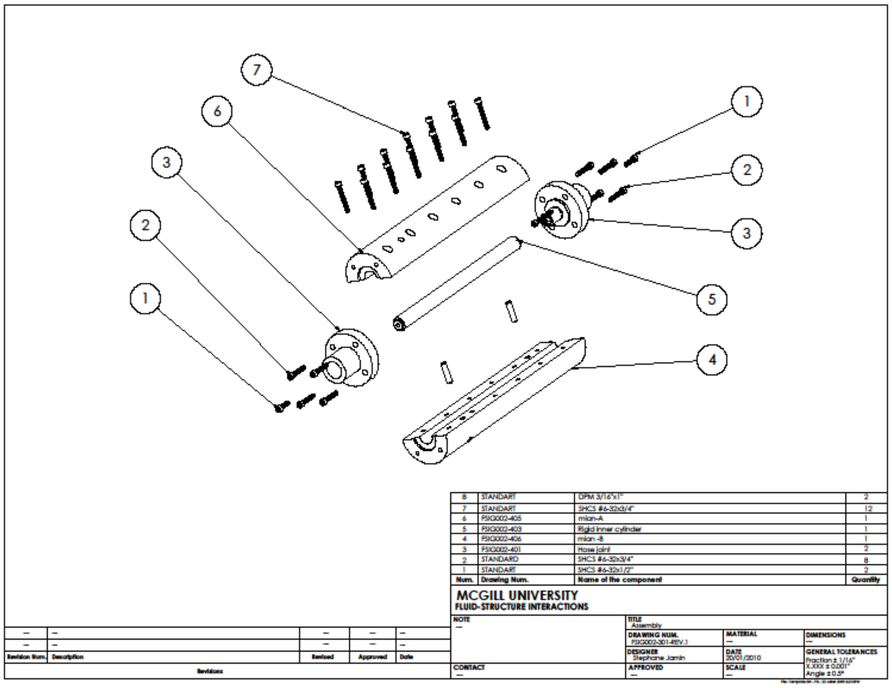

Figure E.1: Assembly technical drawing

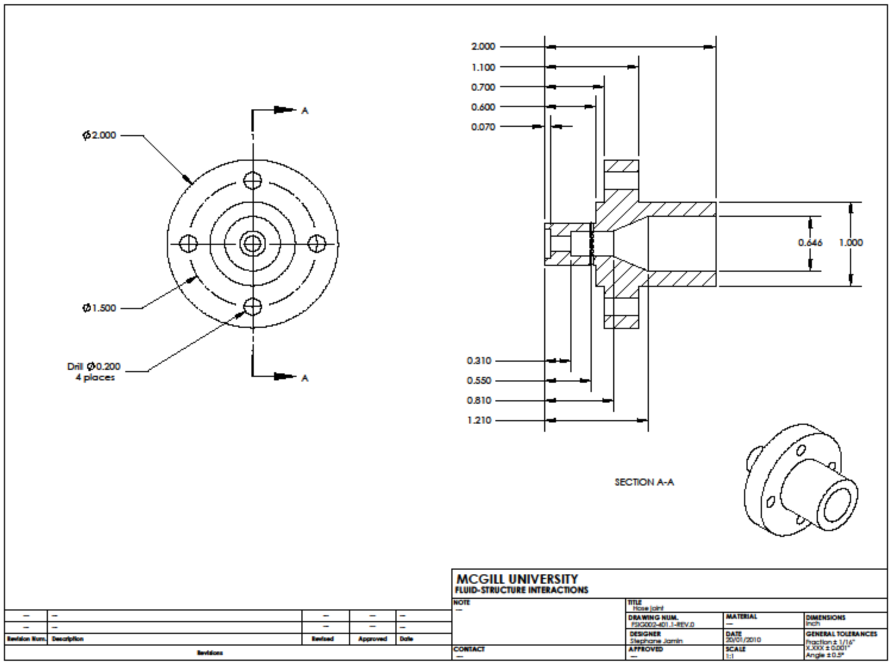

Figure E.2: Component technical drawings

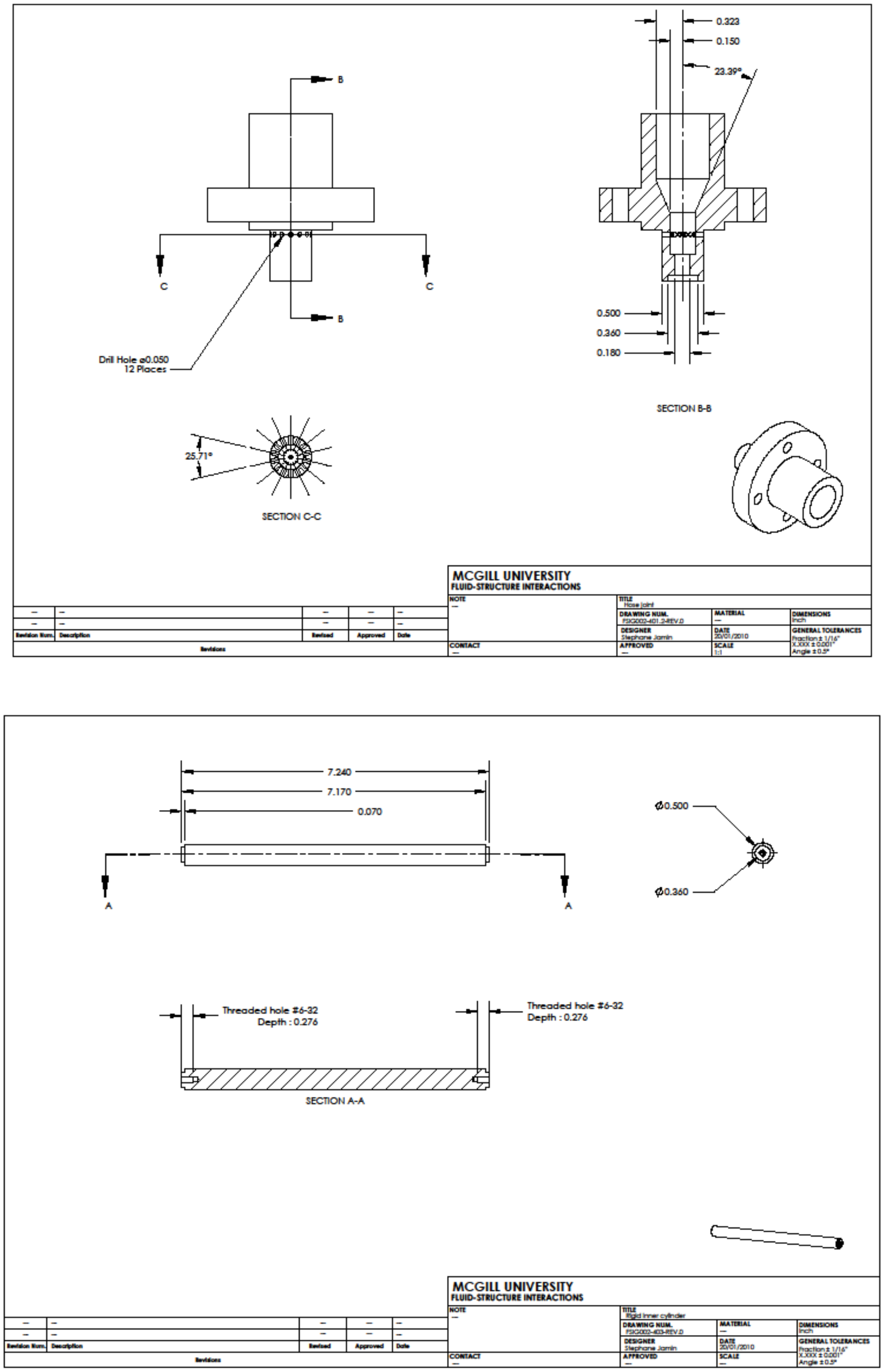

Figure E.2: cont'd

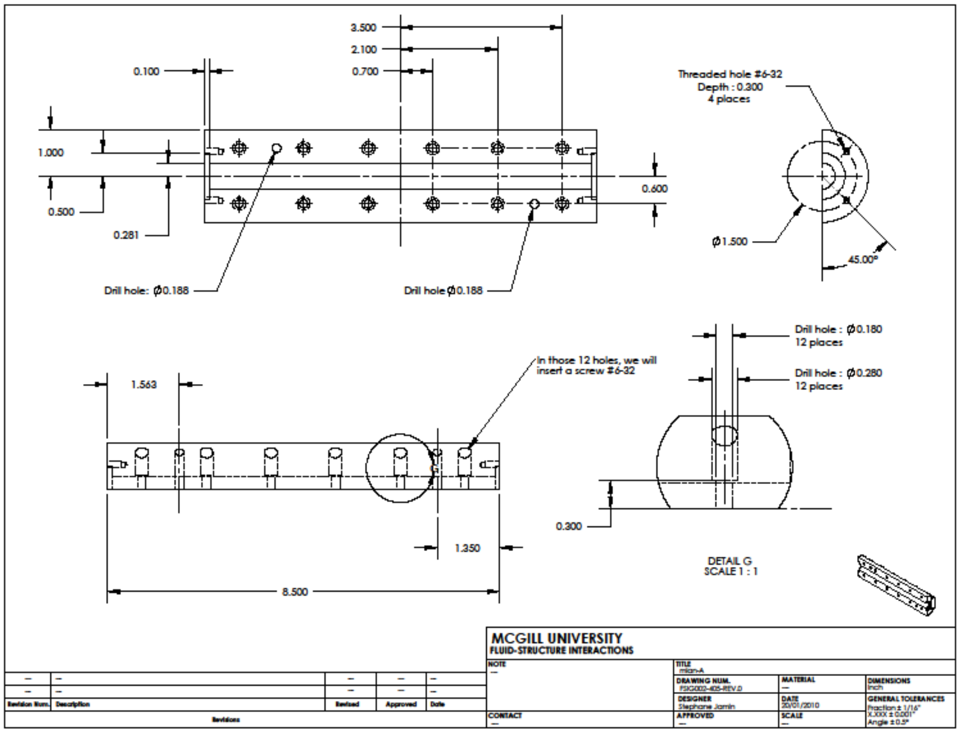

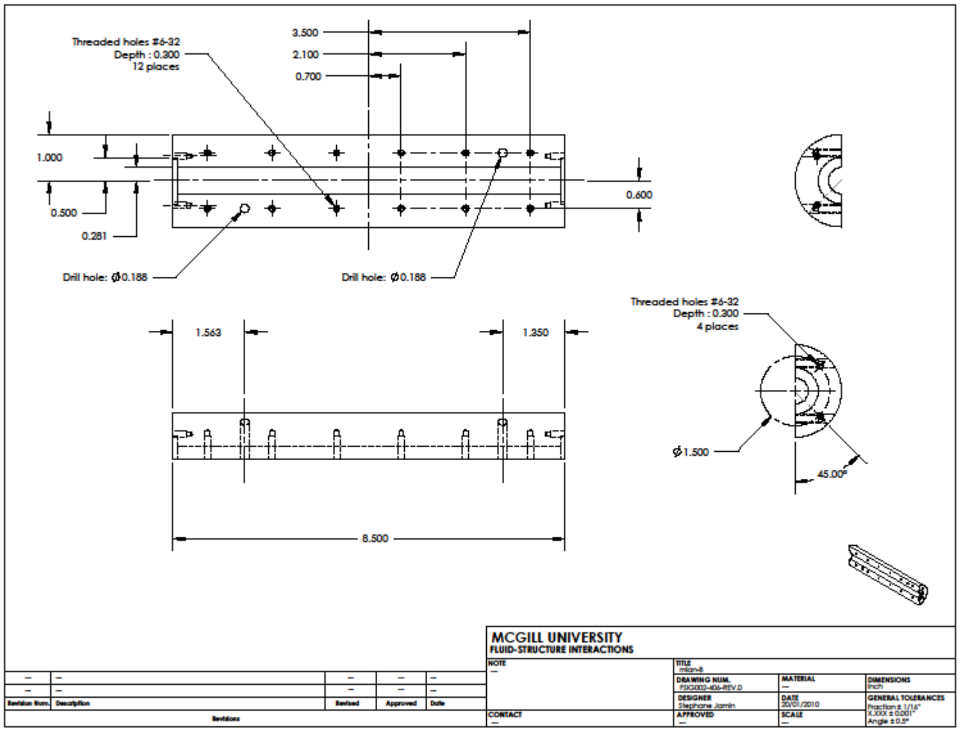

Figure E.2: cont'd

Appendix F: Technical Drawings for Chapter 3

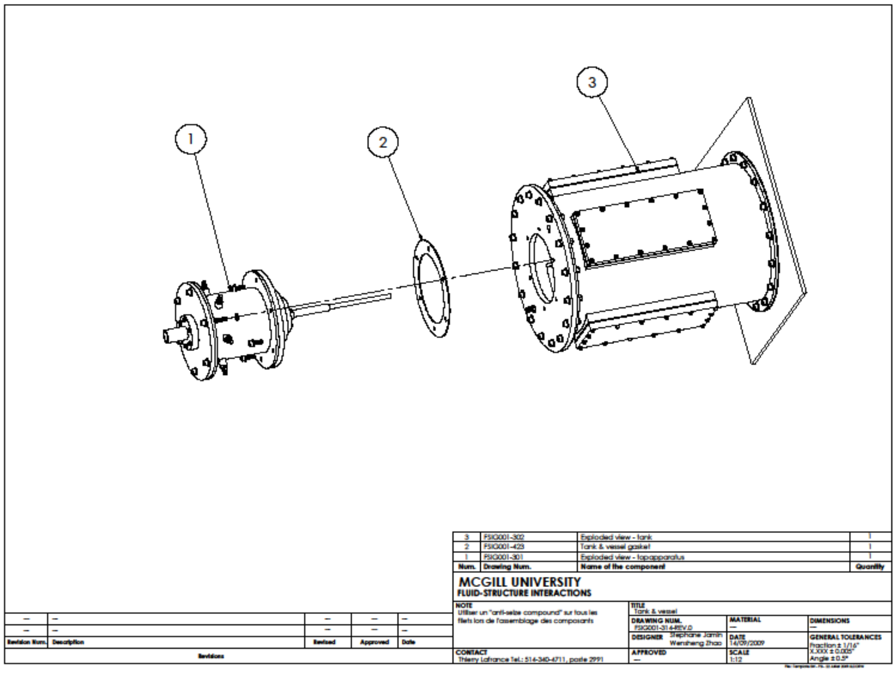

Figure F.1: Assembly technical drawing for the tank and vessel

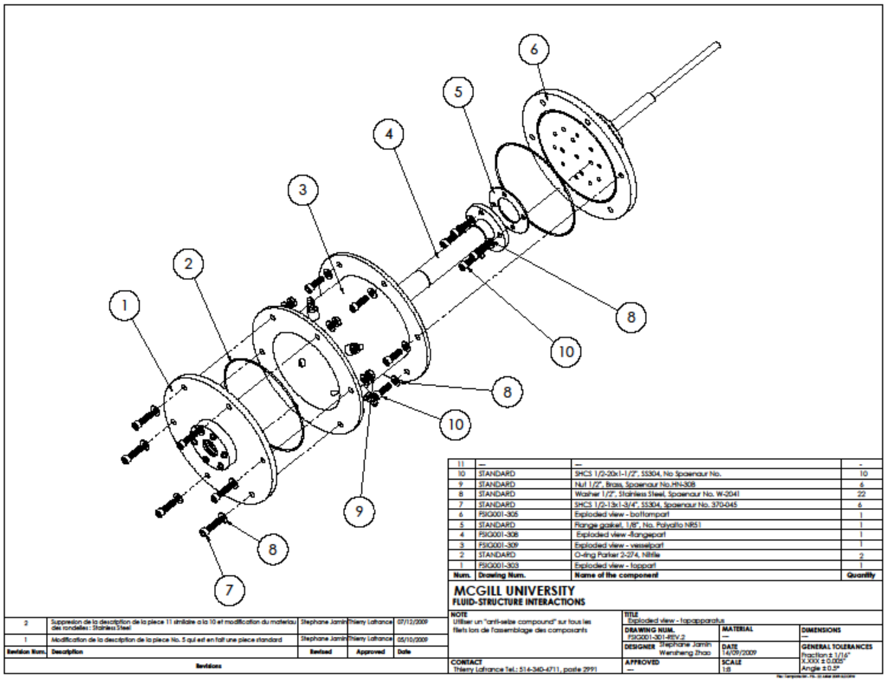

Figure F.2: Assembly technical drawing for the vessel

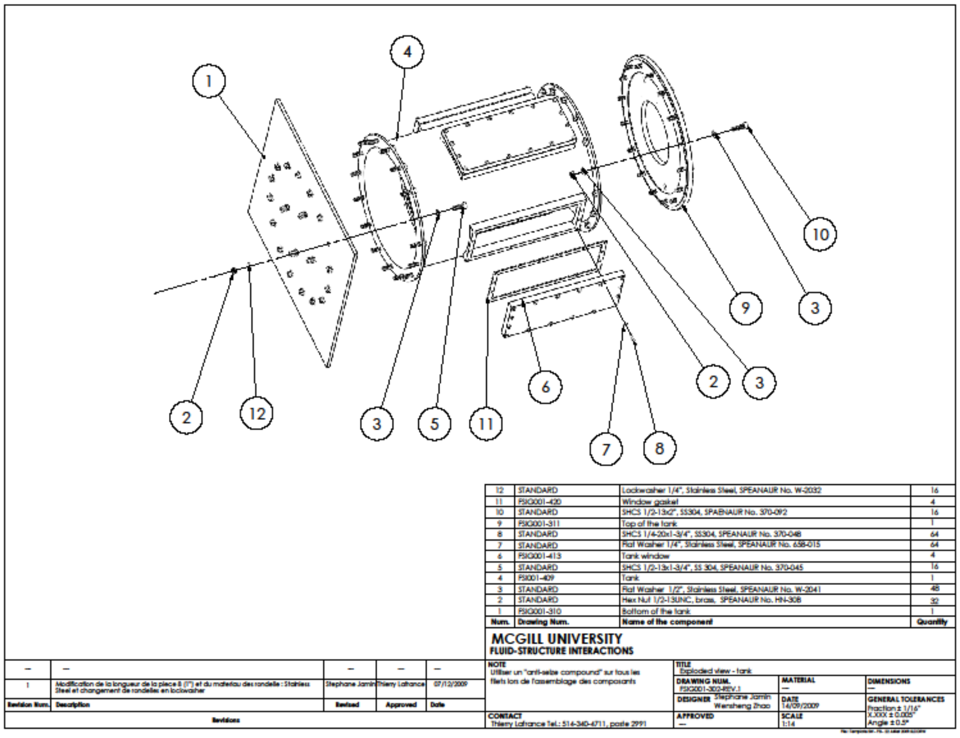

Num.	Drawing Num.	Name of the component	Quantity
12	STANDARD	Lockwasher 1/4", Stainless Steel, SPEANAUR No. W-2032	16
11	FSIG001-420	Window gasket	4
10	STANDARD	SHCS 1/2-13x2", SS304, SPAENAUR No. 370-092	16
9	FSIG001-311	Top of the tank	1
8	STANDARD	SHCS 1/4-20x1-3/4", SS304, SPEANAUR No. 370-048	64
7	STANDARD	Flat Washer 1/4", Stainless Steel, SPEANAUR No. 658-015	64
6	FSIG001-413	Tank window	4
5	STANDARD	SHCS 1/2-13x1-3/4", SS 304, SPEANAUR No. 370-045	16
4	FSI001-409	Tank	1
3	STANDARD	Flat Washer 1/2", Stainless Steel, SPEANAUR No. W-2041	48
2	STANDARD	Hex Nut 1/2-13UNC, brass, SPEANAUR No. HN-308	32
1	FSIG001-310	Bottom of the tank	1

MCGILL UNIVERSITY
FLUID-STRUCTURE INTERACTIONS

NOTE
Utiliser un "anti-seize compound" sur tous les filets lors de l'assemblage des composants

TITLE
Exploded view - tank
DRAWING NUM.
FSIG001-302-REV.1
MATERIAL
—
DIMENSIONS
—
DESIGNER Stephane Jamin Wensheng Zhao
DATE
14/09/2009
GENERAL TOLERANCES
Fraction ± 1/16"
X.XXX ± 0.005"
Angle ± 0.5°
CONTACT
Thierry Lafrance Tel.: 514-340-4711, poste 2991
APPROVED
—
SCALE
1:14

Revision Num.	Description	Revised	Approved	Date
—	—	—	—	—
1	Modification de la longueur de la piece 8 (1") et du materiau des rondelle : Stainless Steel et changement de rondelles en lockwasher	Stephane Jamin	Thierry Lafrance	07/12/2009

Revisions

Figure F.3: Assembly technical drawing for the tank

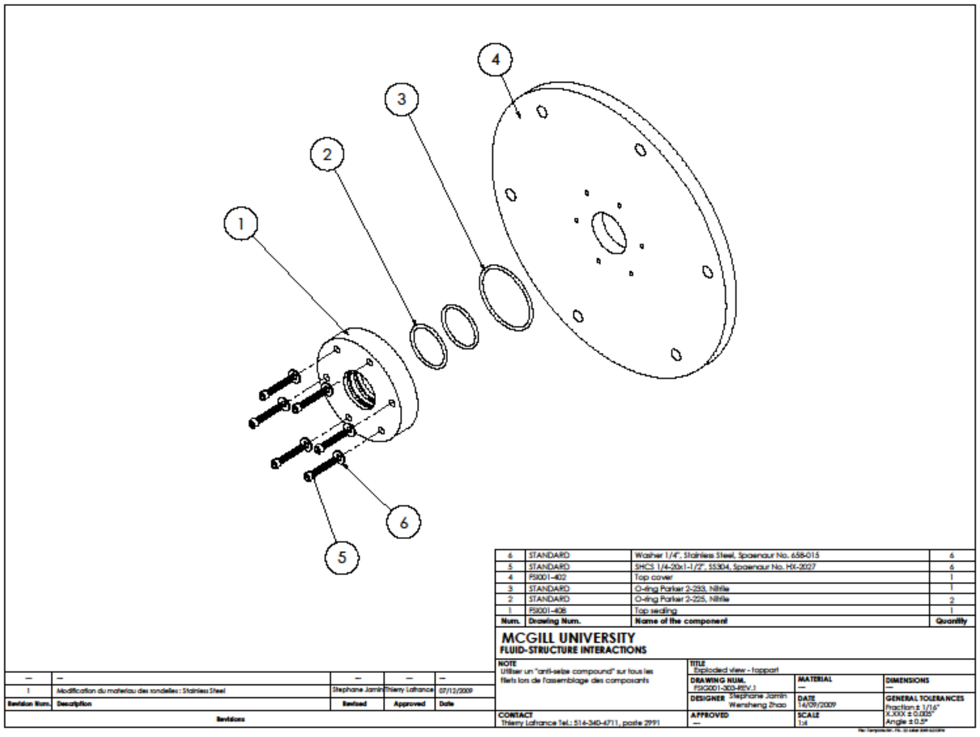

Num.	Drawing Num.	Name of the component	Quantity
6	STANDARD	Washer 1/4", Stainless Steel, Spaenaur No. 658-015	6
5	STANDARD	SHCS 1/4-20x1-1/2", SS304, Spaenaur No. HX-2027	6
4	FSI001-402	Top cover	1
3	STANDARD	O-ring Parker 2-233, Nitrile	1
2	STANDARD	O-ring Parker 2-225, Nitrile	2
1	FSI001-408	Top sealing	1

MCGILL UNIVERSITY
FLUID-STRUCTURE INTERACTIONS

NOTE
Utiliser un "anti-seize compound" sur tous les filets lors de l'assemblage des composants

TITLE
Exploded view - toppart
DRAWING NUM.
FSIG001-303-REV.1
MATERIAL
—
DIMENSIONS
—
DESIGNER Stephane Jamin Wensheng Zhao
DATE
14/09/2009
GENERAL TOLERANCES
Fraction ± 1/16"
X.XXX ± 0.005"
Angle ± 0.5°
CONTACT
Thierry Lafrance Tel.: 514-340-4711, poste 2991
APPROVED
—
SCALE
1:4

Revision Num.	Description	Revised	Approved	Date
—	—	—	—	—
1	Modification du materiau des rondelles : Stainless Steel	Stephane Jamin	Thierry Lafrance	07/12/2009

Revisions

Figure F.4: Sub-assembly drawing for the vessel: Top part

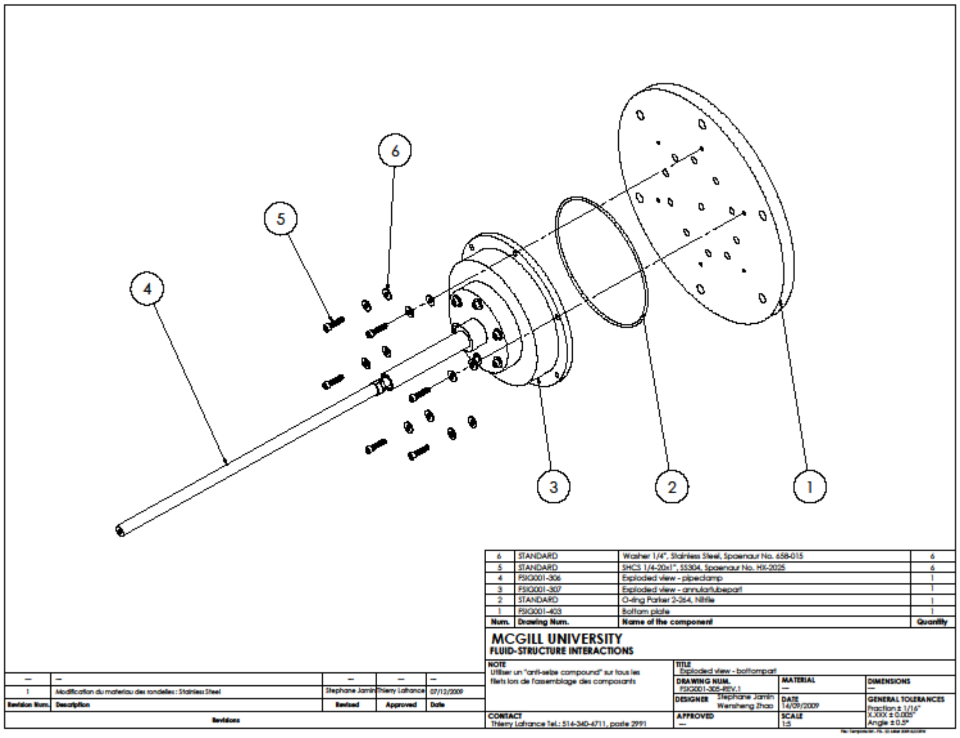

Num.	Drawing Num.	Name of the component	Quantity
6	STANDARD	Washer 1/4", Stainless Steel, Spaenaur No. 658-015	6
5	STANDARD	SHCS 1/4-20x1", SS304, Spaenaur No. HX-2025	6
4	FSIG001-306	Exploded view - pipeclamp	1
3	FSIG001-307	Exploded view - annulartubepart	1
2	STANDARD	O-ring Parker 2-264, Nitrile	1
1	FSIG001-403	Bottom plate	1

MCGILL UNIVERSITY
FLUID-STRUCTURE INTERACTIONS

NOTE Utiliser un "anti-seize compound" sur tous les filets lors de l'assemblage des composants

TITLE Exploded view - bottompart

DRAWING NUM. FSIG001-305-REV.1

MATERIAL —

DIMENSIONS —

DESIGNER Stephane Jamin, Wensheng Zhao

DATE 14/09/2009

GENERAL TOLERANCES Fraction ± 1/16", X.XXX ± 0.005", Angle ± 0.5°

CONTACT Thierry Lafrance Tel.: 514-340-4711, poste 2991

APPROVED —

SCALE 1:5

Revision Num.	Description	Revised	Approved	Date
—	—	—	—	—
1	Modification du materiau des rondelles : Stainless Steel	Stephane Jamin	Thierry Lafrance	07/12/2009

Revisions

Figure F.5: Sub-assembly drawing for the vessel: Bottom part

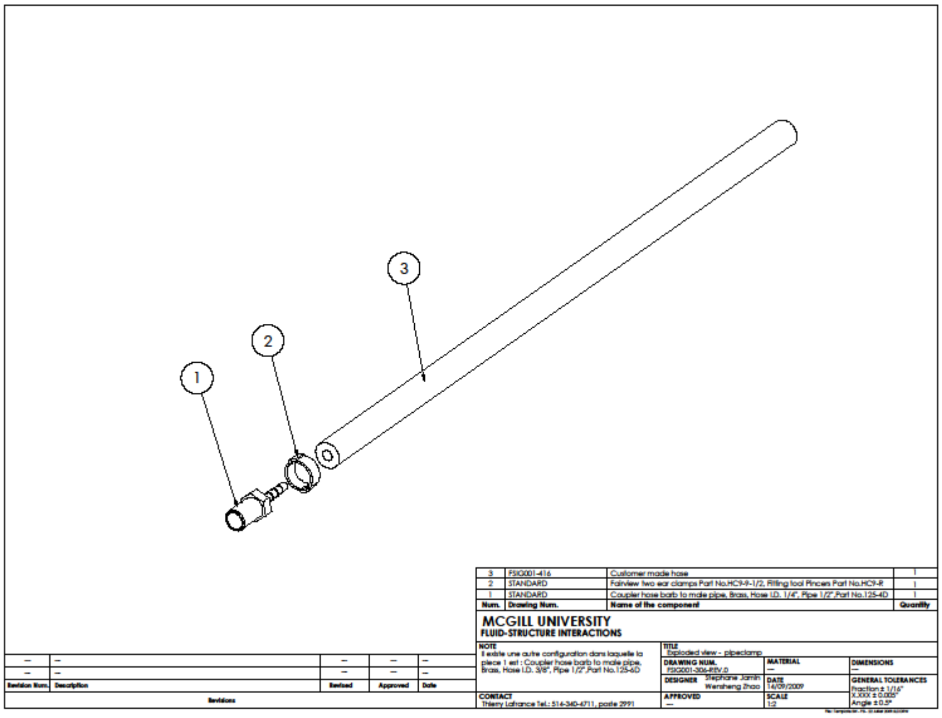

Num.	Drawing Num.	Name of the component	Quantity
3	FSIG001-416	Customer made hose	1
2	STANDARD	Fairview two ear clamps Part No.HC9-9-1/2, Fitting tool Pincers Part No.HC9-R	1
1	STANDARD	Coupler hose barb to male pipe, Brass, Hose I.D. 1/4", Pipe 1/2",Part No.125-4D	1

MCGILL UNIVERSITY
FLUID-STRUCTURE INTERACTIONS

NOTE Il existe une autre configuration dans laquelle la piece 1 est : Coupler hose barb to male pipe, Brass, Hose I.D. 3/8", Pipe 1/2",Part No.125-6D

TITLE Exploded view - pipeclamp

DRAWING NUM. FSIG001-306-REV.0

MATERIAL —

DIMENSIONS —

DESIGNER Stephane Jamin, Wensheng Zhao

DATE 14/09/2009

GENERAL TOLERANCES Fraction ± 1/16", X.XXX ± 0.005", Angle ± 0.5°

CONTACT Thierry Lafrance Tel.: 514-340-4711, poste 2991

APPROVED —

SCALE 1:2

Revision Num.	Description	Revised	Approved	Date
—	—	—	—	—
—	—	—	—	—

Revisions

Figure F.6: Sub-assembly drawing for the vessel: Clamped pipe

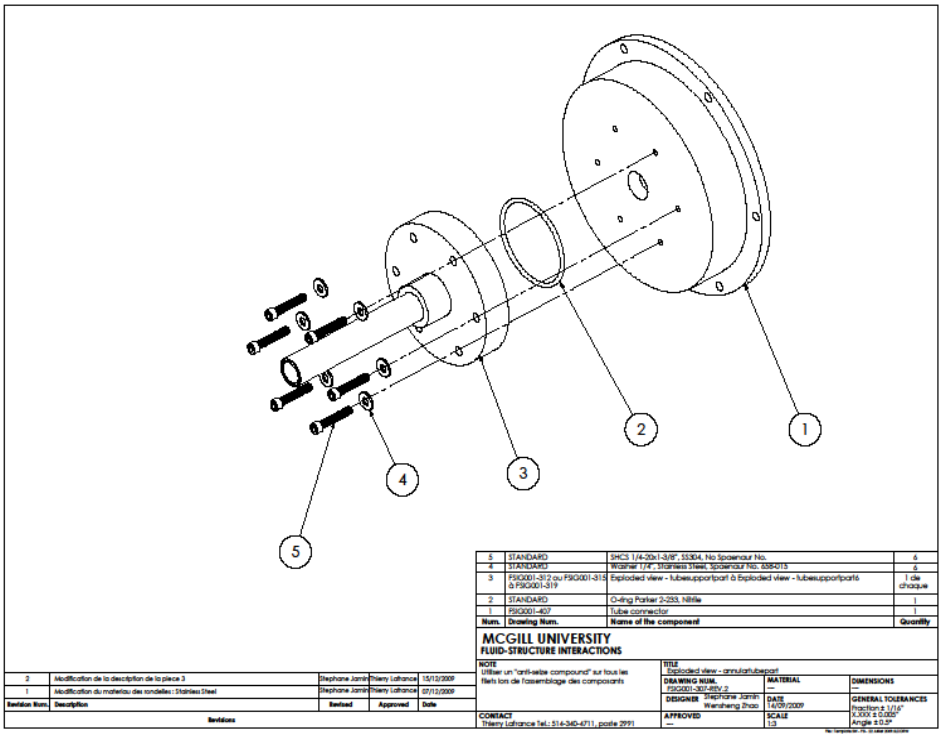

Figure F.7: Sub-assembly drawing for the vessel: Annular tube part

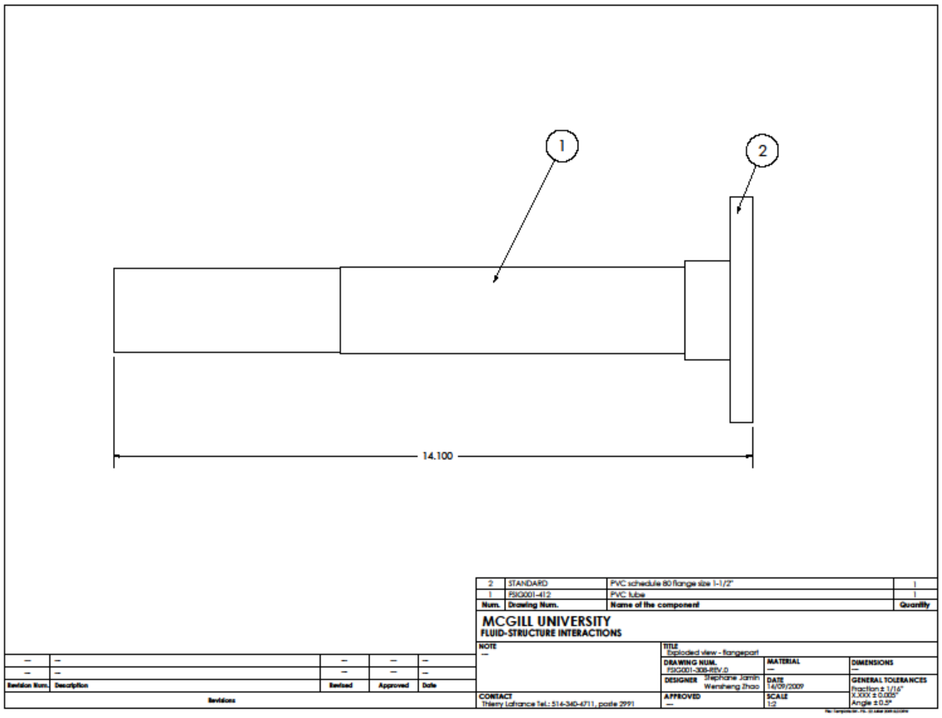

Figure F.8: Sub-assembly drawing for the vessel: Flange part

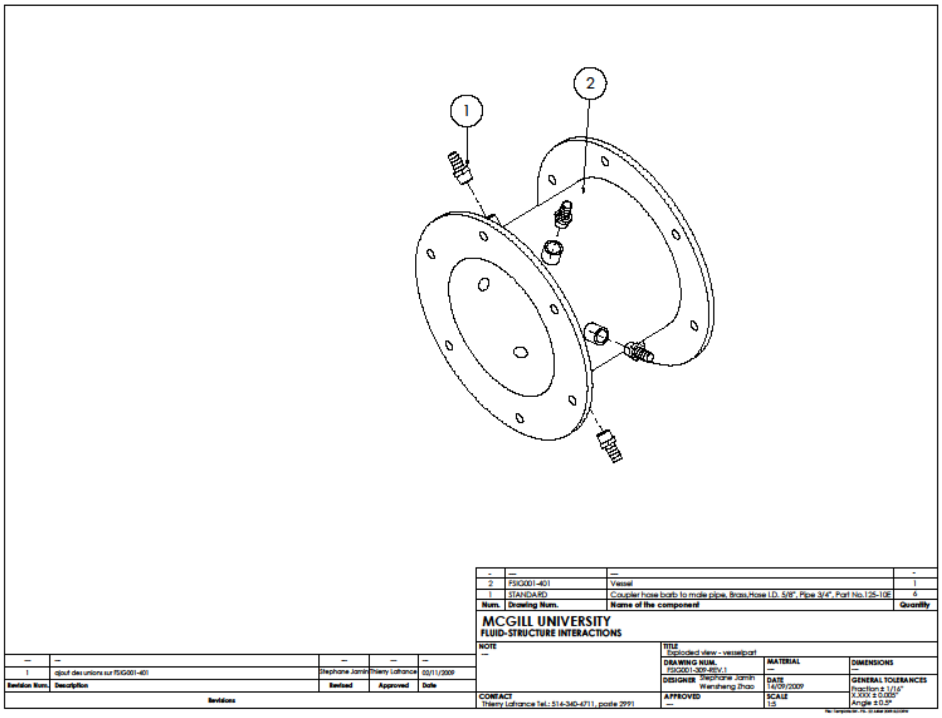

Figure F.9: Sub-assembly drawing for the vessel: Vessel part

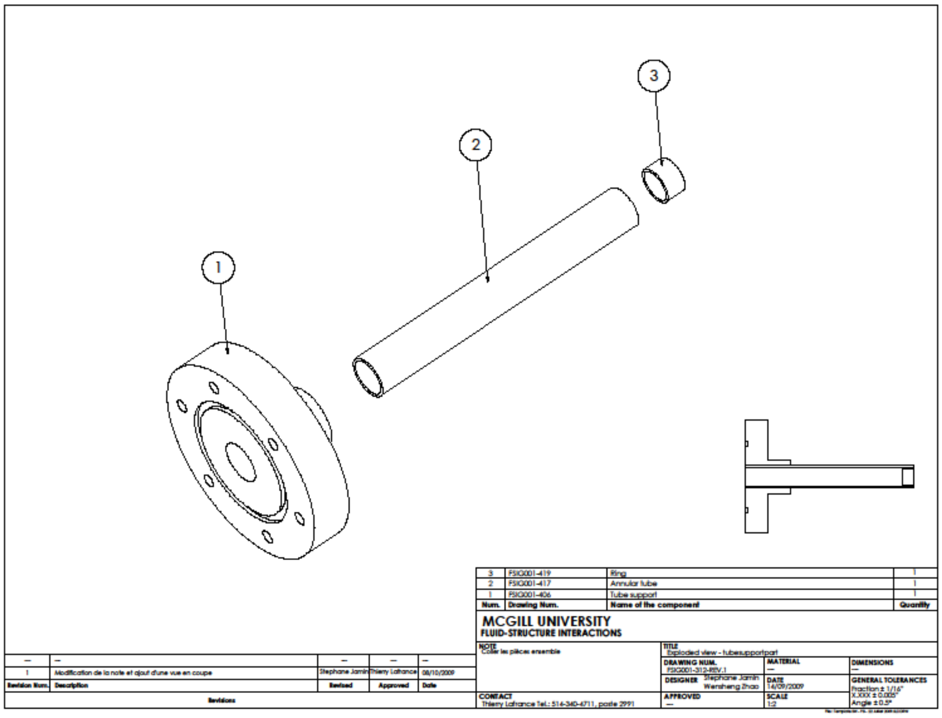

Figure F.10: Sub-assembly drawing for the vessel: Tube support part

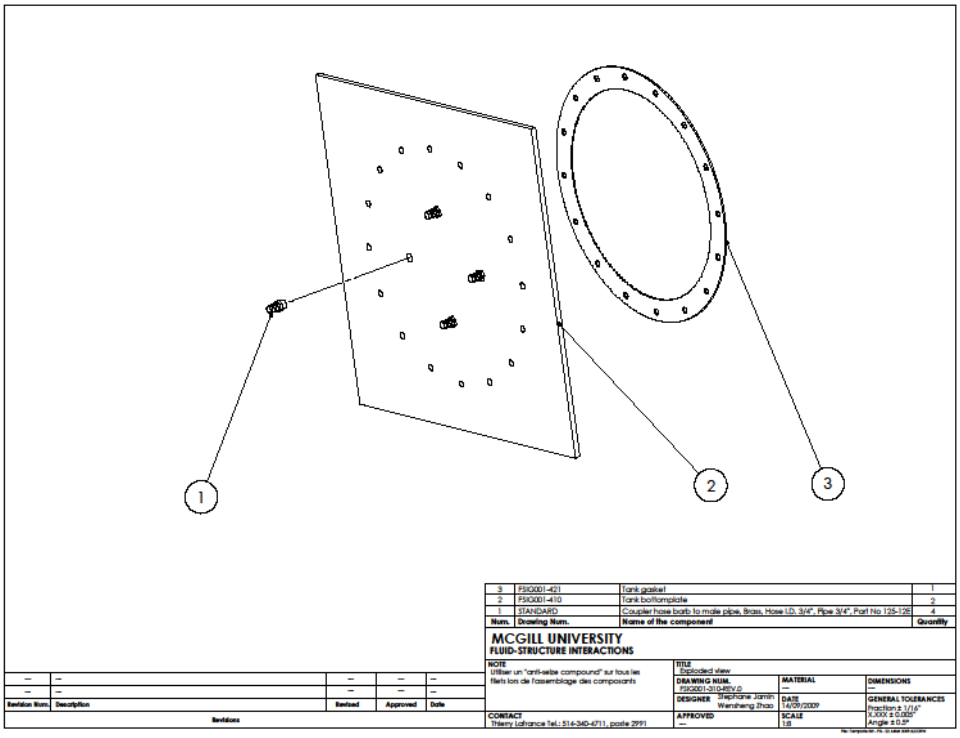

Figure F.11: Sub-assembly drawing for the tank: Bottom of the tank

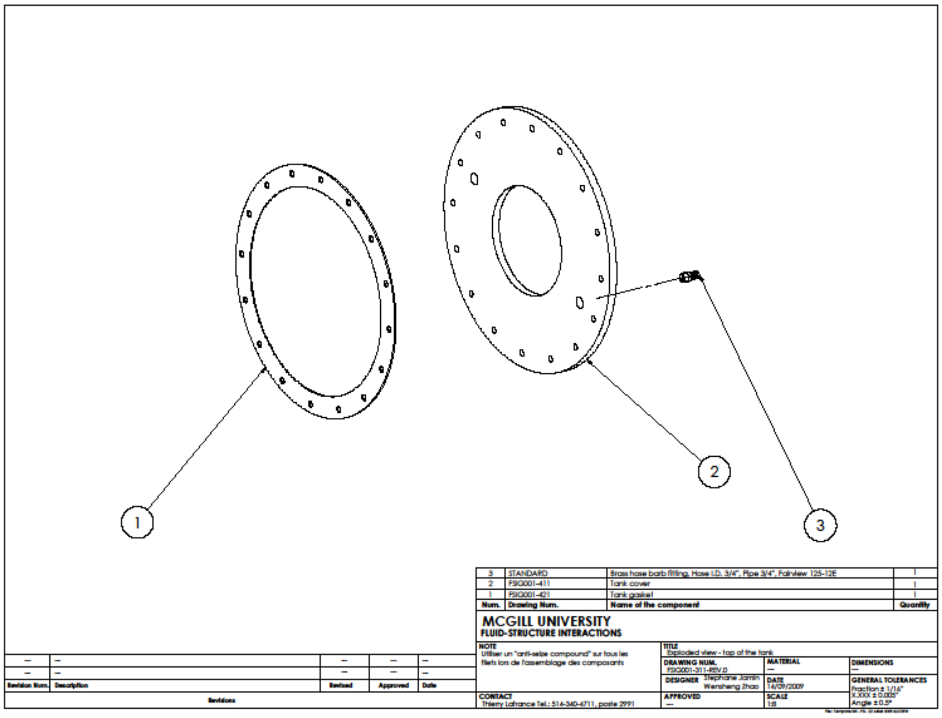

Figure F.12: Sub-assembly drawing for the tank: Top of the tank

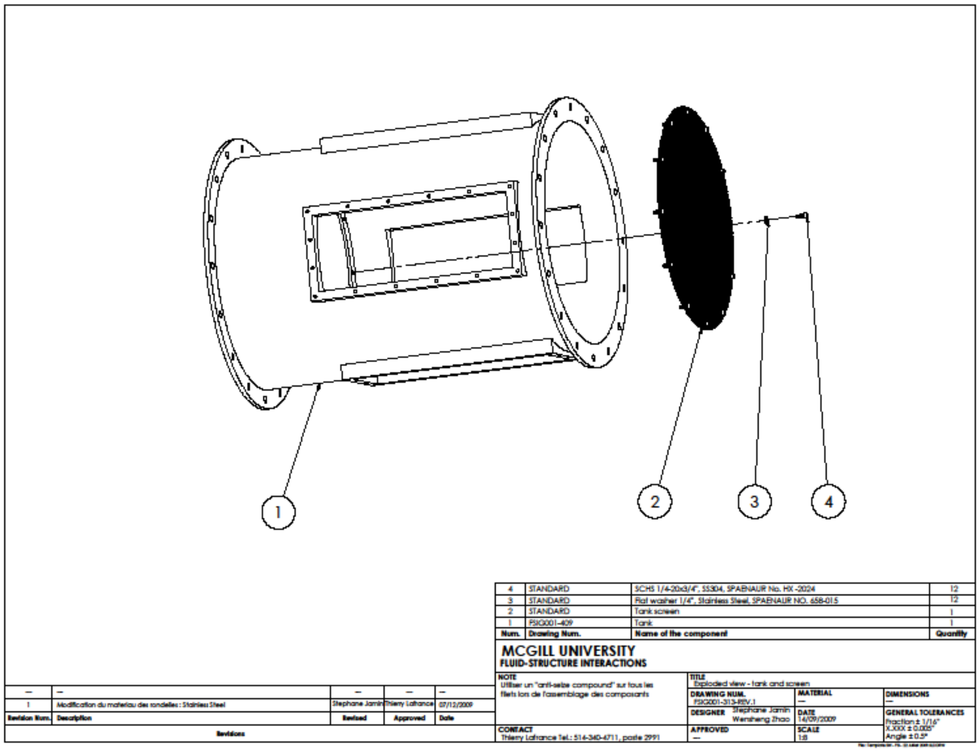

Num.	Drawing Num.	Name of the component	Quantity
4	STANDARD	SCHS 1/4-20x3/4", SS304, SPAENAUR No. HX -2024	12
3	STANDARD	Flat washer 1/4", Stainless Steel, SPAENAUR NO. 658-015	12
2	STANDARD	Tank screen	1
1	FSIG001-409	Tank	1

MCGILL UNIVERSITY
FLUID-STRUCTURE INTERACTIONS

NOTE
Utiliser un "anti-seize compound" sur tous les filets lors de l'assemblage des composants

CONTACT
Thierry Lafrance Tel.: 514-340-4711, poste 2991

TITLE
Exploded view - tank and screen

DRAWING NUM. FSIG001-313-REV.1
MATERIAL —
DIMENSIONS —
DESIGNER Stephane Jamin, Wensheng Zhao
DATE 14/09/2009
GENERAL TOLERANCES
Fraction ± 1/16"
X.XXX ± 0.005"
Angle ± 0.5°
APPROVED —
SCALE 1:8

Revision Num.	Description	Revised	Approved	Date
—	—	—	—	—
1	Modification du materiau des rondelles : Stainless Steel	Stephane Jamin	Thierry Lafrance	07/12/2009

Revisions

Figure F.13: Sub-assembly drawing for the tank: Tank and screen

Bibliography

Anderson, G.L. (1972) A comparison of approximate methods for solving non-conservative problems of elastic stability. *Journal of Sound and Vibration* **22**, 159-168.

Ashley, H. & Haviland, G. (1950) Bending vibrations of a pipeline containing flowing fluid. *Journal of Applied Mechanics* **17**, 229-232.

Au-Yang, M.K. (1976) Free vibration of fluid-coupled coaxial cylindrical shells of different lengths. *Journal of Applied Mechanics* **43**, 480-484.

Bajaj, A.K. & Sethna, P.R. (1982) Bifurcations in three dimensional motions of articulated tubes. Part 2: Non-linear analysis. *Journal of Applied Mechanics* **49**, 612-618.

Benjamin, T.B. (1961) Dynamics of a system of articulated pipes conveying fluid. II. Experiments. *Proceedings of the Royal Society of London. Series A, Mathematical and Physical Sciences* **261**, 487-499.

Benjamin, T.B. (1961) Dynamics of a system of articulated pipes conveying fluid. I. Theory. *Proceedings of the Royal Society of London. Series A, Mathematical and Physical Sciences* **261**, 457-486.

Bourrières, F.J. (1939) Sur un phénomène d'oscillation auto-entretenue en mécanique des fluides réels. *Publication Scientifique et Technique du Ministère de l 'Air* No. 147.

Brown, S.J. & Lieb, B.W. (1980) A comparison of experimental and theoretical vibration results for narrow gap, fluid-coupled, coaxial flexible cylinders. *American Society of Mechanical Engineering,* Paper No 80-C2/PVP-104.

Cesari, F. & Curioni, S. (1971) Buckling instability in tubes subject to internal and external axial fluid flow. *Proceedings of the 4th Conference on Dimensioning and Strength Calculations,* pp. 301-311, Hungarian Academy of Sciences, Budapest.

Chan, S.P. (1984) Dynamics and stability of two coaxial cylindrical shells conveying fluid. M.Eng. Thesis, McGill University.

Chen, S.S. (1971) Flow-induced instability of an elastic tube. *ASME Paper* No.71-Vibr.-39.

Chen, S.S. & Rosenberg, G.S. (1975) Dynamics of a coupled shell-fluid system. *Nuclear Engineering and Design* **32**, 302-310.

Chen, S.S. & Jendrzejczyk, J.A. (2010) General characteristics, transition, and control of instability of tubes conveying fluid. *Journal of the Acoustical Society of America* **77**, 887-895.

De Langre, E., Païdoussis, M.P., Doaré, O. & Moddares-Sadeghi, Y. (2007) Flutter of long flexible cylinders in axial flow. *Journal of Fluid Mechanics* **571**, 371-389.

Den Hartog, J.P. (1969) John Orr memorial lecture: recent cases of mechanical vibration. *The South African Mechanical Engineer* **19**, 53-68.

Dowell, E.H. & Widnall, S.E. (1966) Generalized aerodynamic forces on an oscillating cylindrical shell: subsonic and supersonic flow. *AIAA Journal* **4**, 607-610.

Dowling, A.P. (1988) The dynamics of towed flexible cylinders Part 1. Neutrally buoyant elements. *Journal of Fluid Mechanics Digital Archive* **187**, 507-532.

Dowling, A.P. (1988) The dynamics of towed flexible cylinders Part 2. Negatively buoyant elements. *Journal of Fluid Mechanics Digital Archive* **187**, 533-571.

El Chebair, A., Païdoussis, M.P. & Misra, A.K. (1989) Experimental study of annular-flow-induced instabilities of cylindrical shells. *Journal of Fluids and Structures* **3**, 349-364.

El Chebair, A., Misra, A.K. & Païdoussis, M.P. (1990) Theoretical study of the effect of unsteady viscous forces on inner- and annular-flow-induced instabilities of cylindrical shells. *Journal of Sound and Vibration* **138**, 457-478.

Feodos'ev, V.P. (1951) Vibrations and stability of a pipe when liquid flows through it. *Inzhenernyi Sbornik* **10**, 169-170.

Flügge, W. (1973) Stresses in shells. 2nd edition. Berlin: Springer-Verlag.

Fox, R.W., McDonald, A.T. & Pritchard, P.J. (2009) Introduction to fluid mechanics. Hoboken, N.J. : Chichester:

Ghayesh, M.H. & Païdoussis, M.P. (2010) Three-dimensional dynamics of a cantilevered pipe conveying fluid, additionally supported by an intermediate spring array. *International Journal of Non-Linear Mechanics* doi:10.1016/j.ijnonlinmec.2010.02.001.

Giacobbi, D.B. (2007) A numerical and experimental study of the dynamics of aspirating cantilever pipes. B.Eng. Honours Thesis, McGill University.

Giacobbi, D.B., Semler, C. & Païdoussis, M.P. (2008) Numerical fluid-structure interaction study of a cantilevered pipe discharging or aspirating fluid via a computational fluid dynamics and finite element analysis model. *Proceedings of the 6th International Conference on Engineering Computational Technology* (eds Papadrakakis, M. & Topping, B. H. V.), Paper 48, 2-5 September 2008, Athens, Greece.

Giacobbi, D.B. (2010) The dynamics of aspirating cantilever pipes and pipes conveying variable density fluid. M.Eng. Thesis, McGill University.

Gill, P.A.T. (1972) Vibrations of a clamped-free circular cylindrical shells. *Journal of Sound and Vibration* **25**, 501-502.

Gregory, R.W. & Païdoussis, M.P. (1966) Unstable oscillation of tubular cantilevers conveying fluid. I. Theory. *Proceedings of the Royal Society of London. Series A, Mathematical and Physical Sciences* **293**, 512-527.

Gregory, R.W. & Païdoussis, M.P. (1966) Unstable oscillation of tubular cantilevers conveying fluid. II. Experiments. *Proceedings of the Royal Society of London. Series A, Mathematical and Physical Sciences* **293**, 528-542.

Hannoyer, M.J. & Païdoussis, M.P. (1978) Instabilities of tubular beams simultaneously subjected to internal and external axial flows. *Journal of Mechanical Design* **100**, 328-336.

Hannoyer, M.J. & Païdoussis, M.P. (1979) Dynamics of slender tapered beams with internal or external axial flow. Part1: Theory. *Journal of Applied Mechanics* **46**, 45-51.

Hannoyer, M.J. & Païdoussis, M.P. (1979) Dynamics of slender tapered beams with internal or external axial flow. Part2: Experiments. *Journal of Applied Mechanics* **46**, 52-57.

Hawthorne, W.R. (2010) The early development of the Dracone flexible barge.

Hill, J.L. & Swnason, C.P. (1970) Effect of lumped masses on the stability of fluid conveying tubes. *Journal of Applied Mechanics* **37**, 494-497.

Hobson, D.E. (1982) Fluid-elastic instabilities caused by flow in an annulus. *Proceedings of 3rd International Conference on Vibration in Nuclear Plant,* pp. 440-463, Keswick.

Housner, G.W. (1952) Bending vibrations of a pipeline containing flowing fluid. *Journal of Applied Mechanics* **19**, 109-134.

Jendrzejczyk, J.A. & Chen, S.S. (1985) Experiments on tubes conveying fluid. *Thin-Walled Structures* 109-134.

Krajcinovic, D. (1974) Vibrations of two coaxial cylindrical shells containing fluid. *Nuclear Engineering and Design* **30**, 242-248.

Kuiper, G.L. & Metrikine, A.V. (2005) Dynamic stability of a submerged, free-hanging riser conveying fluid. *Journal of Sound and Vibration* **280**, 1051-1065.

Kuiper, G.L., Metrikine, A.V. & Battjes, J.A. (2007) A new time-domain drag description and its influence on the dynamic behaviour of a cantilever pipe conveying fluid. *Journal of Fluids and Structures* **23**, 429-445.

Kuiper, G.L. & Metrikine, A.V. (2008) Experimental investigation of dynamic stability of a cantilever pipe aspirating fluid. *Journal of Fluids and Structures* **24**, 541-558.

Laithier, B.E. & Païdoussis, M.P. (1981) The equations of motion of initially stressed Timoshenko tubular beams conveying fluid. *Journal of Sound and Vibration* **79**, 175-195.

Langhtjem, M.A. & Sugiyama, Y. (1999) Vibration and stability analysis of cantilevered two-pipes systems conveying different fluids. *Journal of Fluids and Structures* **13**, 251-268.

Long, R.H.Jr. (1955) Experimental and theoretical study of transverse vibration of a tube containing flowing fluid. *Journal of Applied Mechanics* **22**, 65-68.

Lopes, J.L., Païdoussis, M.P. & Semler, C. (1999) Nonlinear dynamics of a cylinder in steady axial flow. MERL-99-2. Dept. of Mechanical Engineering, Mcgill University, Montreal.

Lopes, J.L., Païdoussis, M.P. & Semler, C. (1999) Nonlinear equations of a cylinder in steady axial flow. MERL-99-1. Dept. of Mechanical Engineering, Mcgill University, Montreal.

Lopes, J.L., Païdoussis, M.P. & Semler, C. (2002) Linear and nonlinear dynamics of cantilevered cylinders in axial flow. Part 2: The equations of motion. *Journal of Fluids and Structures* **16**, 715-737.

Love, A.E.H. (1927) The Mathematical Theory of Elasticity. Cambridge University Press.

Luu, T.P. (1983) On the dynamics of three systems involving tubular beams conveying fluid. M.Eng. Thesis, McGill University.

Mateescu, D. & Païdoussis, M.P. (1985) The unsteady potential flow in an axially variable annulus and its effect on the dynamics of the oscillating rigid center-body. *Journal of Fluids Engineering* **107**, 427-

Mateescu, D. & Païdoussis, M.P. (1987) Unsteady viscous effects on the annular-flow-induced instabilities of a rigid cylindrical body in a narrow duct. *Journal of Fluids and Structures* **1**, 197-215.

Mateescu, D., Païdoussis, M.P. & Bélanger, F. (1988) Unsteady pressure measurements on an oscillating cylinder in narrow annular flow. *Journal of Fluids and Structures* **2**, 615-628.

Miller, D.R. (1970) Generation of positive and negative damping with a flow restrictor in axial flow. *Proceedings of the Conference on Flow-Induced Vibrations in Reactor System Components*, Report ANL-7685, pp. 304-311, Argonne National Laboratory, Argonne, IL, USA.

Modarres-Sadeghi, Y., Semler, C., Wadham-Gagnon, M. & Païdoussis, M.P. (2007) Dynamics of cantilevered pipes conveying fluid. Part 3: Three-dimensional dynamics in the presence of an end-mass. *Journal of Fluids and Structures* **23**, 589-603.

Nguyen, V.B. (1992) Theoretical and experimental study of the stability of clamped-free coaxial cylindrical shells subjected to internal and annular flows of viscous liquid. Ph.D. Thesis, McGill University.

Nguyen, V.B., Païdoussis, M.P. & Misra, A.K. (1993) A new outflow model for cylindrical shells conveying fluid. *Journal of Fluids and Structures* **7**, 417-419.

Nguyen, V.B., Païdoussis, M.P. & Misra, A.K. (1993) An experimental study of the stability of cantilevered coaxial cylindrical shells conveying fluid. *Journal of Fluids and Structures* **7**, 913-930.

Niordson, F.I. (1953) Vibrations of a cylindrical tube containing flowing fluid. *Kungliga Tekniska Hogskolans Handlingar (Stockholm)* No. 73.

Niordson, F.I. (2000) An asymptotic theory for circular cylindrical shells. *International Journal of Solids and Structures* **37**, 1817-1839.

Païdoussis, M.P. (1966, a) Dynamics of flexible slender cylinders in axial flow Part 1. Theory. *Journal of Fluid Mechanics* **26**, 717-736.

Païdoussis, M.P. (1966, b) Dynamics of flexible slender cylinders in axial flow Part 2. Experiments. *Journal of Fluid Mechanics* **26**, 737-751.

Païdoussis, M.P. (1968) Stability of towed, totally submerged flexible cylinders. *Journal of Fluid Mechanics Digital Archive* **34**, 273-297.

Païdoussis, M.P. & Trois Maisons, P.E. (1969) Free vibration of a heavy, damped cantilever in a plane inclined to the vertical. Report MERL-69-6. Dept. of Mechanical Engineering, McGill University, Montréal.

Païdoussis, M.P. (1970) Dynamics of tubular cantilevers conveying fluid. *Journal of Mechanical Engineering Science* **12**, 85-103.

Païdoussis, M.P. & Deksnis, E.B. (1970) Articulated models of cantilevers conveying fluid: the study of a paradox. *Journal of Mechanical Engineering Science* **12**, 288-300.

Païdoussis, M.P. & Denise, J.P. (1970) Instabilities of cylindrical shells containing flow. MERL Report No. 70-10. Montreal: Dept. of Mechanical Engineering, McGill University.

Païdoussis, M.P. & Des Trois Maisons, P.E. (1971) Free vibration of a heavy, damped, vertical cantilever. *Journal of Applied Mechanics* **38**, 524-526.

Païdoussis, M.P. & Denise, J.P. (1971) Flutter of cylindrical shells conveying fluid. *Journal of Sound and Vibration* **16**, 459-461.

Païdoussis, M.P. & Denise, J.P. (1972) Flutter of thin cylindrical shells conveying fluid. *Journal of Sound and Vibration* **20**, 9-26.

Païdoussis, M.P. (1973) Dynamics of cylindrical structures subjected to axial flow. *Journal of Sound and Vibration* **29**, 365-385.

Païdoussis, M.P. & Issid, N.T. (1974) Dynamic stability of pipes conveying fluid. *Journal of Sound and Vibration* **33**, 267-294.

Païdoussis, M.P. & Pettigrew, M.J. (1979) Dynamics of flexible cylinders in axisymmetrically confined axial flow. *Journal of Applied Mechanics* **46**, 37-44.

Païdoussis, M.P. & Ostoja-Starzewski, M. (1981) Dynamics of a flexible cylinder in subsonic axial flow. *AIAA Journal* **19**, 1467-1475.

Païdoussis, M.P. & Besançon, P. (1981) Dynamics of arrays of cylinders with internal and external axial flow. *Journal of Sound and Vibration* **76**, 361-380.

Païdoussis, M.P., Chan, S.P. & Misra, A.K. (1984) Dynamics and stability of coaxial cylindrical shells containing flowing fluid. *Journal of Sound and Vibration* **97**, 201-235.

Païdoussis, M.P., Misra, A.K. & Chan, S.P. (1985) Dynamics and stability of coaxial cylindrical shells conveying viscous fluid. *Journal of Applied Mechanics* **52**, 389-396.

Païdoussis, M.P. & Luu, T.P. (1985) Dynamics of a pipe aspirating fluid such as might be used in ocean mining. *Journal of Energy Resources Technology* **107**, 250-255.

Païdoussis, M.P., Luu, T.P. & Laithier, B.E. (1986) Dynamics of finite-length tubular beams conveying fluid. *Journal of Sound and Vibration* **106**, 311-331.

Païdoussis, M.P. (1987) Flow-induced instabilities of cylindrical structures. *Applied Mechanics Reviews* **40**, 163-175.

Païdoussis, M.P., Mateescu, D. & Sim, W.G. (1990) Dynamics and stability of a flexible cylinder in a narrow coaxial cylindrical duct subjected to annular flow. *Journal of Applied Mechanics* **57**, 232-240.

Païdoussis, M.P., Nguyen, V.B. & Misra, A.K. (1991) A theoretical study of the stability of cantilevered coaxial cylindrical shells conveying fluid. *Journal of Fluids and Structures* **5** , 127-164.

Païdoussis, M.P., Misra, A.K. & Nguyen, V.B. (1992) Internal- and annular-flow-induced instabilities of a clamped-clamped or cantilevered cylindrical shell in a coaxial conduit: The effects of system parameters. *Journal of Sound and Vibration* **159**, 193-205.

Païdoussis, M.P. & Li, G.X. (1993) Pipes Conveying Fluid: A Model Dynamical Problem. *Journal of Fluids and Structures* **7**, 137-204.

Païdoussis, M.P. (1998) Fluid-Structure Interactions: Slender Structures and Axial Flow. Volume 1. London: Academic Press Limited.

Païdoussis, M.P. (1999) Aspirating pipes do not flutter at infinitesimally small flow. *Journal of Fluids and Structures* **13**, 419-425.

Païdoussis, M.P., Grinevich, E., Adamovic, D. & Semler, C. (2002) Linear and nonlinear dynamics of cantilevered cylinders in axial flow. Part 1: Physical dynamics. *Journal of Fluids and Structures* **16**, 691-713.

Païdoussis, M.P. (2005) Some unresolved issues in fluid-structure interactions. *Journal of Fluids and Structures* **20**, 871-890.

Païdoussis, M.P. (2005) Fluid-structure interactions: slender structures and axial flow. Volume 2. London: Elsevier Academic Press.

Païdoussis, M.P., Semler, C. & Wadham-Gagnon, M. (2005) A reappraisal of why aspirating pipes do not flutter at infinitesimal flow. *Journal of Fluids and Structures* **20**, 147-156.

Païdoussis, M.P., Semler, C., Wadham-Gagnon, M. & Saaid, S. (2007) Dynamics of cantilevered pipes conveying fluid. Part 2: Dynamics of the system with intermediate spring support. *Journal of Fluids and Structures* **23**, 569-587.

Païdoussis, M.P. (2008) Dynamics of cantilevers subjected to internal and/or external axial flow: new developments and insights. *Proceeding of the 9th International Conference on Flow-Induced Vibration* (eds Zolotarev, I. & Horacek, J.), Paper 289, 30 June - 3 July 2008, Prague, Czech Republic.

Païdoussis, M.P. (2008) The canonical problem of the fluid-conveying pipe and radiation of the knowledge gained to other dynamics problems across Applied Mechanics. *Journal of Sound and Vibration* **310**, 462-492.

Païdoussis, M.P., Luu, T.P. & Prabhakar, S. (2008) Dynamics of a long tubular cantilever conveying fluid downwards, which then flows upwards around the cantilever as a confined annular flow. *Journal of Fluids and Structures* **24**, 111-128.

Ratigan, J.L. (2008) Brine string integrity and model evaluation. *Solution Mining Research Institute Fall 2008 Technical Conference,* Galveston, Texas, USA.

Rayleigh, J.W.S. & Lindsay, R.B. (1945) The theory of sound. New York: Dover Publications.

Rinaldi, S. (2009) Experiments on the dynamics of cantilevered pipes subjected to internal and/or external axial flow. M.Eng. Thesis, McGill University.

Rinaldi, S. & Païdoussis, M.P. (2010) Dynamics of a cantilevered pipe discharging fluid, fitted with a stabilizing end-piece. *Journal of Fluids and Structures* **26**, 517-525

Rousselet, J. & Hermann, G. (1981) Dynamic behaviour of continuous cantilevered pipes conveying fluid near critical velocity. *Journal of Applied Mechanics* **48**, 943-947.

Semler, C., Li, G.X. & Païdoussis, M.P. (1994) The non-lineare equations of motion of pipes conveying fluid. *Journal of Sound and Vibration* **169**, 577-599.

Semler, C., Lopes, J.L., Augu, N. & Païdoussis, M.P. (2002) Linear and nonlinear dynamics of cantilevered cylinders in axial flow. Part 3: nonlinear dynamics. *Journal of Fluids and Structures* **16**, 739-759.

Sharma, C.B. & Johns, D.J. (1971) Vibration characteristics of a clamped-free and clamped-ring-stiffened circular cylindrical shell. *Journal of Sound and Vibration* **14**, 459-474.

Sharma, C.B. & Johns, D.J. (1972) Free vibration of cantilever circular cylindrical shells-A comparative study. *Journal of Sound and Vibration* **25**, 433-449.

Sharma, C.B. (1974) Calculation of natural frequencies of fixed-free circular cylindrical shells. *Journal of Sound and Vibration* **35**, 55-76.

Shayo, L.K. & Ellen, C.H. (1974) The stability of finite length circular cross-section pipes conveying inviscid fluid. *Journal of Sound and Vibration* **37**, 535-545.

Shayo, L.K. & Ellen, C.H. (1978) Theoretical studies of internal flow-induced instabilities of cantilever pipes. *Journal of Sound and Vibration* **56**, 463-474.

Sugiyama, Y., Tanaka, Y., Kishi, T. & Kawagoe, H. (1985) Effect of a spring support on the stability of pipes conveying fluid. *Journal of Sound and Vibration* **100**, 257-270.

Sugiyama, Y., Kawagoe, H., Kishi, T. & Nishiyama, S. (1988) Studies on the stability of pipes conveying fluid (the combined effect of a spring support and a lumped mass). *JSME International Journal* **31**, 20-26.

Wadham-Gagnon, M., Païdoussis, M.P. & Semler, C. (2007) Dynamics of cantilevered pipes conveying fluid. Part 1: Nonlinear equations of three-dimensional motion. *Journal of Fluids and Structures* **23**, 545-567.

Wang, I. & Ni, Q. (2009) Vibration of slender structures subjected to axial flow or axially towed in quiescent fluid. *Advances in Acoustics and Vibration* **vol. 2009**, 19 pages.

Wang, X. & Bloom, F. (1999) Dynamics of a submerged and inclined concentric pipe system with internal and external flows. *Journal of Fluids and Structures* **13**, 443-460.

Weaver, D.S. & Myklatun, B. (1973) On the stability of thin pipes with an internal flow. *Journal of Sound and Vibration* **31**, 399-410.

Weaver, D.S. & Unny, T.E. (1973) On the dynamic stability of fluid-conveying pipes. *Journal of Applied Mechanics* **40**, 48-52.

Weppelink, H. (1979) Free vibration of finite circular cylindrical shells and tubes with and without a surrounding fluid. M.Sc. Thesis, Technische Hogeschool Twente, Enschede, The Netherlands.

Widnall, S.E. & Dowell, E.H. (1967) Aerodynamic forces on an oscillating cylindrical duct with an internal flow. *Journal of Sound and Vibration* **6**, 71-85.

Yamaki, N. (1984) Elastic Stability of Circular Cylindrical Shells. Amsterdam: North-Holland.

Yeh, T.T. & Chen, S.S. (1977) Dynamics of a cylindrical shell system coupled by viscous fluid. *Journal of the Acoustical Society of America* **62**, 262-270.

Drawings of the Experimental Configurations Tested in Chapter 3

While reviewing this Thesis, it appeared very useful to have a spare of the drawings of the different configurations tested in Chapter 3. Indeed, because of the great number of configurations, it is not that simple to remember which configuration is related to which flow path. So that the reader can have a look at these drawings while reading the Thesis, these drawings are presented here again.

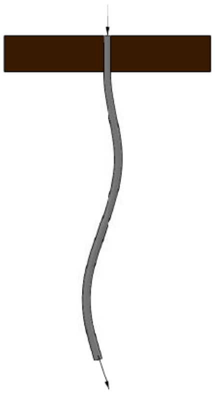

Config. 1

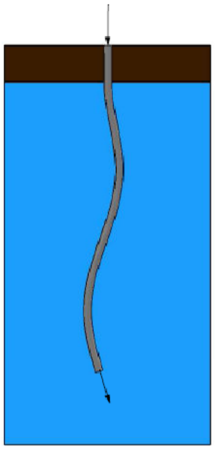

Config. 2i

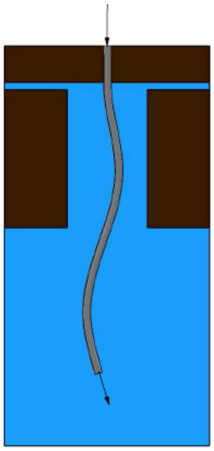

Config. 2ii

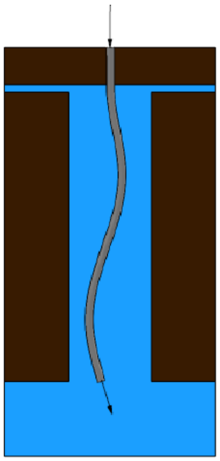

Config. 2iii

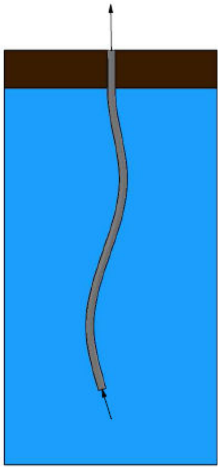

Config. 3i

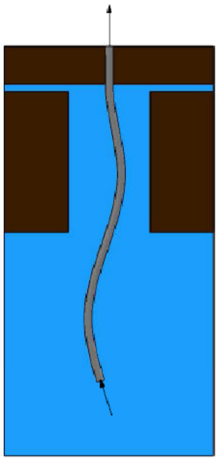

Config. 3ii

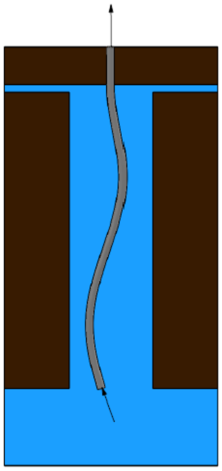

Config. 3iii

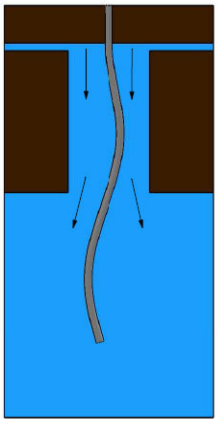

Config. 4i

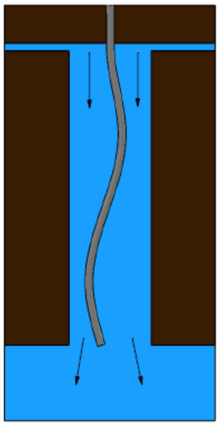

Config. 4ii

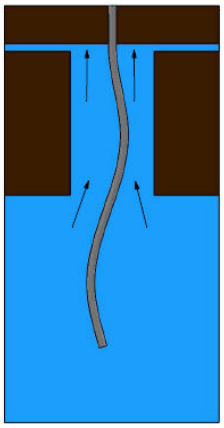

Config. 5i

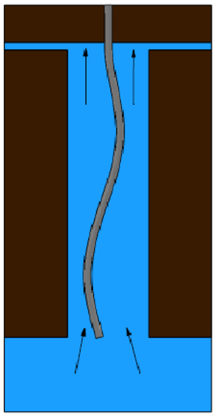

Config. 5ii

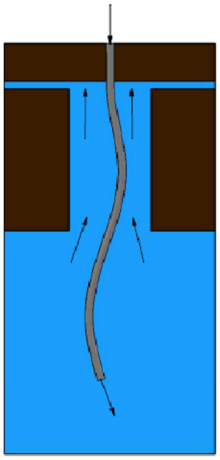

Config. 6i

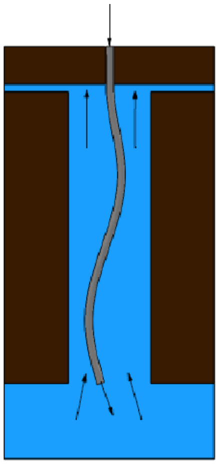

Config. 6ii

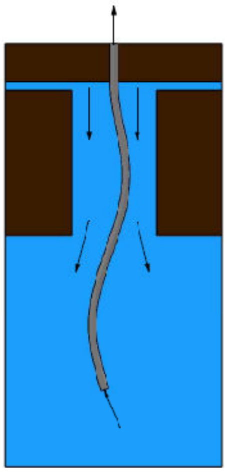

Config. 7i

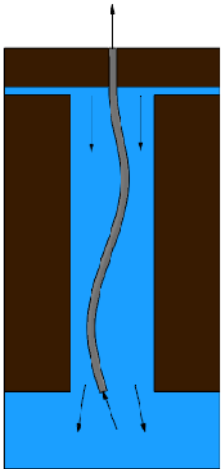

Config.7ii